Carrier distribution processes in Quantum Dot ensembles

Matthew D. Hutchings

Ph.D. Thesis

School of Physics and Astronomy

Cardiff University

2012

DECLARATION

This work has not been submitted in substance for any other degree or award at this or any other university or place of learning, nor is being submitted concurrently in candidature for any degree or other award.

Signed ………………………………… (candidate)   Date …………………………

STATEMENT 1

This thesis is being submitted in partial fulfillment of the requirements for the degree of PhD.

Signed ………………………………… (candidate)   Date …………………………

STATEMENT 2

This thesis is the result of my own independent work/investigation, except where otherwise stated. Other sources are acknowledged by explicit references. The views expressed are my own.

Signed ………………………………… (candidate)   Date …………………………

STATEMENT 3

I hereby give consent for my thesis, if accepted, to be available for photocopying and for inter-library loan, and for the title and summary to be made available to outside organisations.

Signed ………………………………… (candidate)   Date ....…………………

Abstract.

In this thesis the development of new analysis methods that study the carrier distributions in quantum dots (QDs) directly from experimental measurement of spontaneous emission and gain spectra are described. These were applied to three InAs QD structures that are nominally identical except for the doping type in the active region, one p-doped, one n-doped and one left un-doped for comparison. The effect that carrier localisation within individual dots had on this temperature dependence of the carrier distribution under injection was studied and related to key aspects associated with laser device performance.

The nature of QD occupation in the three samples was determined through measurement of the carrier temperature (T_C) of the electrons populating the QD states. It was found that the un-doped samples QDs were in thermal equilibrium with the bulk lattice down to 200 K. Below this temperature the sample's QD states become decoupled from the lattice and at 60 K QD occupation was shown to be random. The p-doped sample was shown to be non-thermal between 300 K and 200 K where at 150 K the occupation of QDs became random. The T_C was observed to decrease for this sample below 200 K and this was attributed to fewer dopants ionising as the temperature decreased. The n-doped sample was also shown to be non-thermal between 300 K and 200 K with the QD occupation becoming random at 100 K. In all three samples, above 300 K, the measured T_C was lower than that predicted by a Fermi-Dirac distribution and this was attributed to the these QDs having a large number of closely spaced hole states leading to a size dependence of the number of these states. This means an individual ΔE_f exists for a given set of dot sizes. So emission from an ensemble of dots is "smoothed" across different ΔE_f levels leading to a reduction in the apparent T_C. These results have a significant effect on the threshold current densities of these samples and suggest that the differences observed due to doping will not be reproduced by calculations assuming a quasi-thermal equilibrium across the QD structure.

The temperature dependence of the shift in gain peak energy was determined for the un and p-doped samples. This showed that the blue-shift of the gain peak due to state-filling in un-doped QD structures is independent of temperature, at a given

value of peak gain, over the temperature range studied (200 K to 350 K). In the p-doped sample however, the state filling is temperature dependent at any fixed gain with a shift of 8meV observed between 200 K and 350 K. This was attributed to the wide electron state distribution and the lowering of the electronic quasi-Fermi level by the p-doping. This renders p-doped materials unsuitable for any technology application where gain peak wavelength temperature stability is required for efficient operation.

Acknowledgements.

I would like to thank my PhD supervisors Prof. P. Blood and Prof. P. Smowton for their advice and guidance throughout my studies, their enthusiasm and expertise in this field was invaluable. I would also like to thank the former and current members of the condensed matter group for our many insightful and stimulating discussions.

I'm particularly grateful to Dr. I. O'Driscoll for his insight and patience during the early period of my PhD and for generally making my studies enjoyable.

I wish to thank the Physics and Astronomy technical staff particularly Mr S. Baker, Mr I. Robinson, Mr R. Tucker, and Mr H. Lang. My experimental research would have not been possible without their continuous support. I also thank Dr. A. Sobiesierski and Mrs K. Barnett for the processing of the various structures I have tested during my time in Cardiff.

I'd like to thank my good friends, my time in Cardiff would not have been so enjoyable if it weren't for their company. Finally, I give a special thanks to my family for their loving support and encouragement throughout my University studies.

Contents.

Chapter 1. Introduction.

1.1. Thesis rationale.

The research, presented in this thesis, was conducted with the intention of furthering the understanding behind carrier distribution in InAs Quantum dot (QD) ensembles. In particular the effect that carrier localisation within individual dots had on this carrier distribution was studied and related to key aspects associated with laser device performance.

The use of QDs as a gain medium in diode lasers has attracted significant attention in recent years due to the promise of a number of attractive characteristics. These include very low threshold currents, good temperature insensitivity and a wide gain spectrum capable of ultra-short pulse generation [Bimberg, et al., 1999, Ustinov, 2003]. InAs QDs are of particular interest as they are capable of achieving long wavelength lasing on GaAs substrates over the 1.3 – 1.6 μm range used for communication technologies. The use of GaAs as a substrate is well established within current commercial industries and so is a desirable basis for new generation laser diodes. Current commercially available laser diodes operating in this wavelength range are based on InP Quantum well (QW) lasers. This material has a relatively shallow potential well and this leads to these lasers having poor temperature sensitivity. In Vertical Cavity Surface Emitting Lasers (VCSELs) Bragg mirror stacks are required to obtain precise wavelength emission. These are difficult and expensive to engineer in InP QW structures but are common and inexpensive on GaAs substrates.

Although QD lasers have been shown to have a low threshold current density (10.4 Acm^{-2} [Deppe, et al., 2009]) and high operating temperature (220 °C CW [Kageyam, et al., 2012]) they have not yet fulfilled their true potential. This is due to a number of factors, many of which originate in the inhomogeneous size distribution existent in epitaxialy grown QD ensembles. In particular, the temperature dependence of threshold current arises from the thermal spread of carriers across the distribution of confined energy states. It is thought that at room temperature equilibrium is achieved between the spatially separated dot states by thermal

exchange of carriers with Quantum well like "wetting layer" states in these QD structures. However, this is not always true [O'Driscoll, et al., 2009] and at lower temperatures dots states are occupied randomly, independently of their energy. This has a profound influence on the temperature dependence of threshold current [O'Driscoll, et al., 2010].

Determining the carrier distribution within a QD structure is key to understanding the behaviour of its laser performance. This thesis describes the development of new analysis techniques capable of fully characterising the carrier distributions and state filling processes that occur under electrical injection, directly from experimental measurement of spontaneous emission and gain spectra [Blood, et al., 2003]. These are powerful tools and It is demonstrated how they can be used to explain key performance limiting properties of InAs QDs. The application of these analysis tools to new quantum dot materials will provide the insight necessary to improve the design of QD materials and fully exploit their properties.

1.2. Thesis structure.

In the next chapter the background theory and laser concepts required to understand the results and discussions in the subsequent chapters of this thesis is described. Details of the most widely used growth method for QD structures are given, including the benefits and consequences this growth has on its material characteristics.

In chapter three the measurement techniques used to obtain the results presented in this thesis are described. This includes details of the segmented contact technique [Blood, et al., 2003] and experimental apparatus used to probe the QD structures. Details of the QD materials studied in this thesis are given.

In chapter four the motivation behind the incorporation of modulation doping within the active region of InAs QD materials is discussed. The results obtained from segmented contact measurements made on three differently doped samples are described where the temperature dependence of key material properties, including modal gain and radiative and threshold current densities, are characterised.

In chapter five a novel method for analysing the way in which carriers are distributed across the available states of a QD material is introduced. A description of how this method is able to identify the temperature at which carriers no longer distribute thermally across the spatially separated dots states, leading to random occupancy across the electronic structure, is given. It is then described how the understanding this provides is able to explain the material properties characterised in chapter four.

In chapter six the shifts in the gain peak, which determines a device's lasing wavelength, with injection is studied and the temperature dependence of these shifts is explained. It is shown how the inclusion of p-doping within QD structures induces a strong temperature dependence in their state filling properties that leads to very temperature sensitive gain peak movement. This has significant implications for laser applications such as VCSELs whose properties are sensitive to shifts in gain peak wavelength.

In chapter seven a summary of the main conclusions made from this thesis work is given and a plan for future work that utilises the techniques developed is described.

Chapter 2. Background theory.

2.1. Introduction.

In this chapter, the background theory required to understand and explain the experimental results presented in this thesis is provided. A brief account of the fundamental processes behind lasing is given, more detailed descriptions of general laser diode theory can be found in [Coldren and Corzine, 1995]

2.2. The Laser Diode.

In this section the conditions required to achieve lasing in semiconductor devices is outlined and the type of structure studied in this thesis is described.

2.2.1. Principles of lasing.

A laser emits coherent light when a high density of photons within the lasing medium causes stimulated emission processes to dominate over absorption and spontaneous emission. In a semiconductor laser diode, to induce the photon densities required for stimulated emission to dominate, an optical "active region" is placed in a resonant cavity with partially reflecting mirrors (semiconductor crystal facets). Electrons in the active region are electrically injected into non-stable high energy states, called conduction band (CB) states in laser diodes. These electrons relax down to lower energy states (called valence band (VB) states) where they are more stable, releasing a photon of energy equivalent to the energy separation of the states (spontaneous emission). Some of the photons emitted along the length of the cavity are reflected back along the cavity at the laser facets. If there is a greater number of electrons in CB states than VB states (inverted carrier populations) then these photons induce more electrons in the CB to relax producing more and more coherent emission (stimulated emission), otherwise they excite electrons in the VB (absorption). If the amplification (gain) along the cavity is sufficient to match the loss processes in that cavity (i.e loss due to emission at the facets (α_m) and scattering within the cavity (α_i)) then lasing will occur. The gain at which this occurs is called the threshold gain (G_{th}) and is given by Equation 2.1, when the reflectivity (R) of the mirrors at each end of the cavity, of length L, are identical.

$$G_{th} = \alpha_i + \frac{1}{L}\ln\left(\frac{1}{R}\right)$$

<div align="right">Equation 2.1</div>

In this work the laser material is a semiconductor and the cavity mirrors are formed by the air/semiconductor interface. The active region (gain material) is made up of a quantum dot (QD) structure within a so called wetting layer, which can be considered to be a quantum well due to its dimensions. More details of this structure are given in section 2.2.2. To induce a non-equilibrium of the electrons within the active region (i.e. invert the population) the material is electrically driven thereby forcing electrons into the higher lying states of the structure.

2.2.2. Quantum Dot active region.

To facilitate electrical injection within laser diodes the active region is placed between wider band gap n and p type semiconductor layers forming a double heterostructure (DH). The first DHs used a bulk narrow gap semiconductor, typically 100-200 nm thick, as the active region. The DH was further developed by reducing the thickness of the active region to ~10 nm or less. This forms a Quantum Well (QW) where carriers are quantum confined in the smallest dimension (the growth direction – see Figure 2.1). Quantum confinement can be extended by reducing the dimensions of the semiconductor active region in the other directions, forming a 1 dimensional Quantum Wire and 0 dimensional QD structures. In a QD laser diode structure the dots are grown on a larger band gap material, via self assembly, (more details of this in section 2.4.1) which can be sufficiently thin to be a QW structure. During the growth process the dots form on a so called wetting layer (WL) that is the same semiconductor material as the dots and these WL states are well like. This entire structure is embedded in a wider band gap quantum well forming a so called dot in a well structure (DWELL), this is embedded in a waveguide consisting of a high refractive index material surrounded by a low refractive index material. This provides separate confinement of carriers and photons and so is known as a separate confinement heterostructure (SCH). Figure 2.1 shows a schematic of this type of structure. As discussed, a QD active region is incorporated into the materials studied in this thesis and so the following sections of

this chapter outline the brief theory behind QDs detailing the advantages that quantum confinement in three dimensions creates.
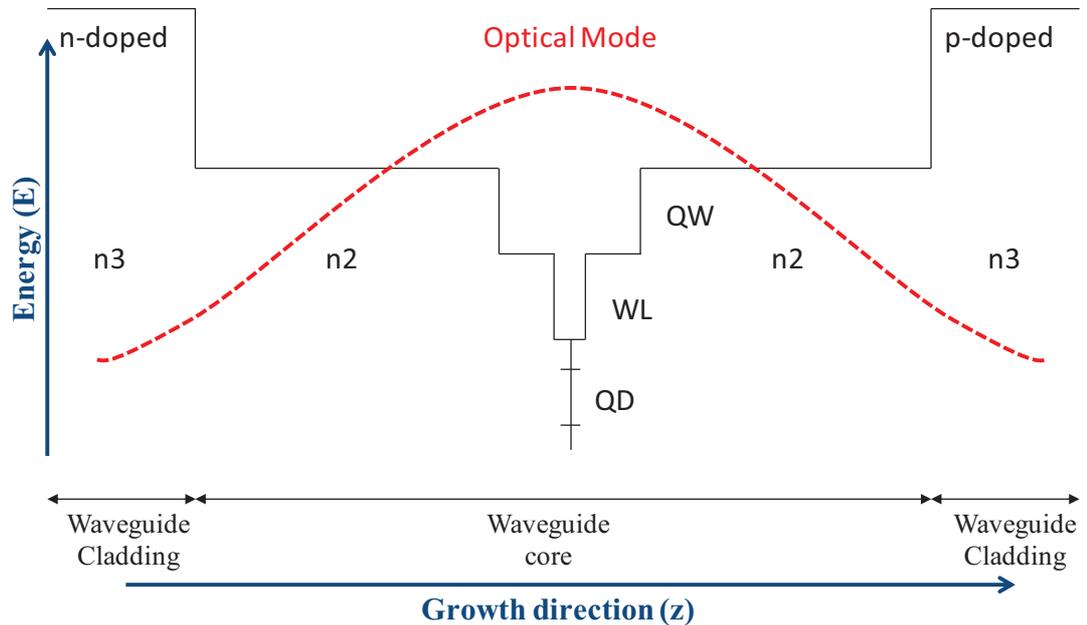
Figure 2.1. Schematic diagram of the CB structure of a QD active region (DWELL) and SCH. The refractive indices (n) of the wavequide are marked and in this structure n2 > n3. The optical mode (red dashed line) is also illustrated.

2.3. Optical transitions in QDs.

A QD can be considered as a two energy level system consisting of a single conduction and valence band state. In a two energy level system there are several possible types of electronic transitions. Figure 2.2 illustrates the possible optical transitions in a two level system. An ideal QD active region consists of many sets of identical two energy level systems and so a two state system is able to describe such materials behaviour, if this is integrated over all possible pairs of states within the structure.
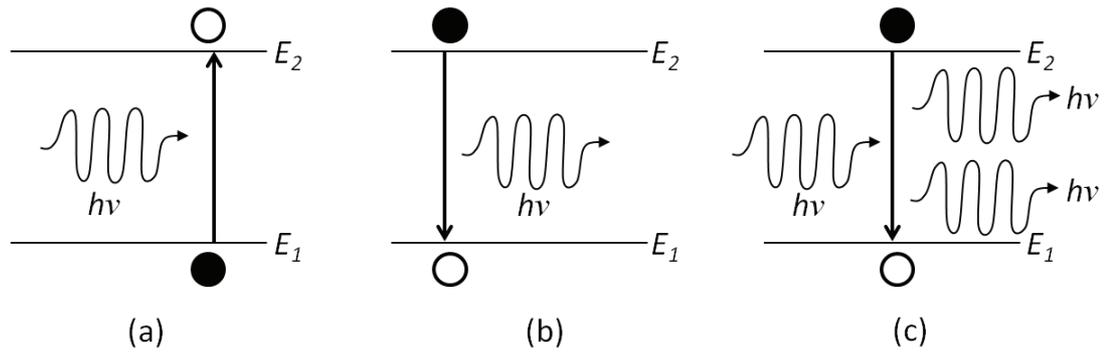
Figure 2.2. Possible optical transitions between two energy levels, E_1 and E_2. filled circles represent electrons and open circles represent empty states (hole). a)Absorption, b) Spontaneous emission and c) Stimulated emission.

2.3.1. Absorption.

If a photon is incident upon the two level system, described above, that has an energy equal to that of the separation between the states then it will be absorbed by an electron in the lower state if there is an empty state (hole) in the upper energy level. All of the energy of the photon is transferred to this electron, thus eliminating the photon, causing it to be excited to the upper empty state. In a QD system consisting of a number of these identical two level systems the rate at which absorption occurs is controlled by the number of photons with the appropriate energy, the number of electrons in the lower states and the number of empty upper states. So the total rate is given by Equation 2.2.

$$R_{abs} = B_{12}(1-f_2)f_1\rho(h\nu)$$

<div align="right">Equation 2.2</div>

where f_1 and f_2 are the occupation probabilities for electrons in the lower and upper states respectively, ρ is the photon density and B_{12} is a coefficient.

2.3.2. Spontaneous emission.

If an electron exists in the upper energy level and there is an empty state in the lower energy level then a spontaneous emission event can occur. Here the electron relaxes from the upper level to the lower level through the emission of a photon with energy equal to that of the energy separation of the levels. This process is initiated by a so called 'virtual' photon generated by zero-point fluctuations in the electromagnetic field. Spontaneous emission is therefore independent of any photon density and so

its rate is controlled by the relative occupation of the two energy levels and is given by Equation 2.3.

$$R_{spon} = A_{21} f_2 (1 - f_1)$$

Equation 2.3

where A_{21} is a coefficient. A photon emitted through this spontaneous emission process will have a random phase and direction of motion.

2.3.3. Stimulated emission.

If again there is an electron in the upper energy level and an empty state in the lower energy level then an incoming photon, with an energy equal to the difference between the levels, will perturb this electron causing it to relax to the lower state. This process is called stimulated emission and the relaxation of the electron releases a second photon. This photon has the same energy as the perturbing photon and is coherent with it (has the same phase and direction of motion). The rate of this process, like the absorption process, is controlled by the photon density and the relative occupation probabilities and is given by Equation 2.4.

$$R_{stim} = B_{21}(1 - f_1) f_2 \rho(h\nu)$$

Equation 2.4

where B_{21} is another coefficient.

In thermal equilibrium all absorption and emission rates are balanced and so

$$R_{abs} = R_{spon} + R_{stim}$$

Equation 2.5

This expression was solved by Einstein in 1917 [Einstein, 1917. Coldren and Corzine, 1995] where he compared his derivation of $\rho(h\nu)$ with Plank's law of blackbody radiation to show that for Equation 2.5 to hold for all temperatures

$$B_{12} = B_{21}$$

Equation 2.6

and

$$A_{21} = \frac{8\pi n^3}{h^3 c^3} (h\nu)^2 B_{21}$$

<div align="right">Equation 2.7</div>

The constants A_{21}, B_{21} and B_{12} are therefore called Einstein coefficients and Equation 2.7 shows that there is a fundamental link between spontaneous and stimulated emission. A_{21} has units of reciprocal time and is related to the spontaneous lifetime τ_{spon} by Equation 2.8.

$$A_{21} = \frac{1}{\tau_{spon}}$$

<div align="right">Equation 2.8</div>

2.3.4. Non radiative recombination.

So far only electronic transitions that involve the emission or absorption of a photon have been discussed, however it is also possible for an electron to recombine with a empty state (hole) non-radiatively (i.e. recombination without emission of a photon). Such processes do not contribute towards optical gain in a laser cavity and so minimising them is advantageous and a major area of interest. There are two main sources of non-radiative recombination in semiconductor lasers, recombination via defect states and Auger recombination.

Non-radiative recombination via defects.

In an ideal semiconductor crystal lattice there are no defects or impurities. However, in real structures these form during growth. A state is formed at point defects (caused by vacant lattice sites), surfaces and interfaces. These defect states are spatially localised and may form within the band gap of the semiconductor material. Recombination via defect states was first described by [Hall, 1952] and separately by [Shockley and Read, 1952] and so is commonly referred to as Shockley-Read-Hall recombination. Figure 2.3 shows a schematic of a recombination event through a defect state.
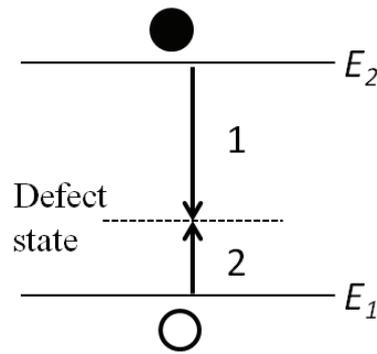
Figure 2.3. Non radiative recombination via defect state.

This process involves the capture of an electron and a hole into the defect state, both of which are independent events that result in the emission of a phonon. Recombination between the upper and lower state has occurred once the defect state has captured both an electron and a hole. So the overall rate of recombination is determined by the slowest of these two capture processes and is therefore proportional to the density of that carrier type (N).

Auger recombination.

Auger recombination occurs via the indirect recombination of a hole and an electron. Energy is conserved in this process through the excitation of a second electron (or hole) into the higher lying states (lower lying states) of the wetting layer. The QDs are localised and so momentum is easily conserved for transition within the same dot. This electron then relaxes through multi phonon emission. There are several different Auger processes and one such process is illustrated in Figure 2.4.
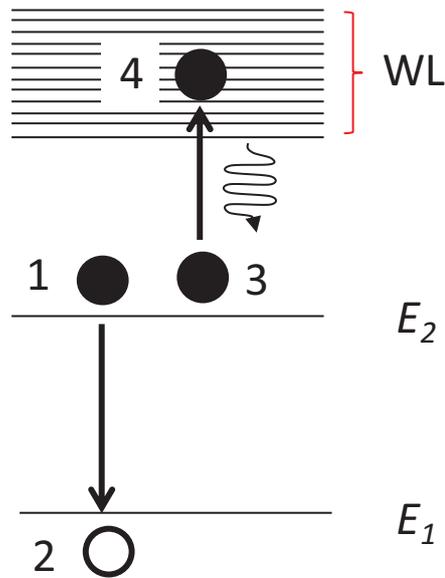
Figure 2.4. Example of an Auger recombination process

In this example an electron recombines with a hole, but the energy associated with that transition is transferred to a second electron causing it to be excited to a higher wetting layer state, this electron then relaxes back to its initial state through multi phonon emission. This process involves the simultaneous recombination of an electron with a hole as a second electron is excited and so is a three carrier process. In bulk semiconductors the rate of auger recombination tends to be proportional to N^3, assuming the number of electrons equals the number of holes.

2.4. Quantum Dot systems.

As discussed, the work in this thesis is concerned with the characterisation of semiconductor lasers with QD active regions and the following sections describe some of the key aspects that effect QD performance.

QD systems were predicted to have several advantages over lasers based on QW active regions. These include a reduction of threshold current density, reduced temperature sensitivity of threshold current density and a narrow spectral linewidth. The improvements in threshold current were predicted due to the increased energy separation of the states, from the quantum confinement in three dimensions, requiring fewer carriers to achieve population inversion. QDs should theoretically have a delta like density of states, again from the three dimensional quantum

confinement, and so it was expected that this would lead to reduced temperature sensitivity. A narrow spectral emission was predicted as the QDs should theoretically only have one possible energy transition within the dot.

2.4.1. Quantum Dot growth.

The most common method used to form QDs, by epitaxy using Molecular beam epitaxy (MBE) or Metalorganic vapour phase epitaxy (MOVPE), in the active region of a semiconductor laser diode is by self assembly through the Stranski-Krastanow growth mode. This growth mode occurs when a semiconductor material is epitaxially deposited upon another semiconductor that has a different lattice constant. The InAs QDs, studied in this thesis, are grown on GaAs. These two semiconductors have a lattice parameter mismatch of 7% and this is sufficient to induce the Stranski-Krastanow growth mode. The initial few monolayers deposited form a planar layer known as the wetting layer, as more and more layers of semiconductor are deposited three dimensional islands form on top of the wetting layer. The formation of these islands reduces the elastic strain caused by the lattice mismatch. The size, shape, density and uniformity of these islands is extremely sensitive to the growth conditions and this leads to significant issues in obtaining the ideal properties described above as well as making reproducibility of structures difficult. These islands that form on top of the wetting layer are the QD structures and they are capped with materials that minimise the strain between these layers and subsequent optical confinement layers. Dots grown in this self-assembly technique form a coupled system with the wetting layer of the structure. The wetting layer provides a reservoir of carriers and this has profound effects on the properties of such QD materials. The effect the wetting layer has on carrier distribution in QD materials will be discussed in greater detail in section 2.4.7.

2.4.2. Broadening in Self-Assembled Quantum Dots.

Although the development of self-assembled QDs has led to the realisation of this materials use in commercial lasers, it leads to broadening of the ideal delta like spectral function. On top of electronic transition broadening that affects all systems, self assembled dot materials exhibit spectral broadening due to differences between the dots in the ensemble.

Homogeneous broadening.

Homogeneous broadening arises from the probability that an electronic transition may occur before the QD system undergoes a dephasing event due to a collision. From the Heisenberg uncertainty principle, this finite amount of time between dephasing events leads to a probability that the energy of the electron will not exactly match that of the quantum state. This type of broadening is usually expressed using a normalised Lorentzian function with a typical linewidth of a few meV [Borri, et al., 2001. Ouerghui, et al., 2005]. In InAs QD systems the homogeneous broadening has been experimentally measured by [Borri, et al., 2002] and has a full width at half max (FWHM) of approximately 6 meV at 300K.

Inhomogeneous broadening.

Whilst in a single QD the optical transitions consist of a series of homogeneously broadened delta function lines around its quantum states, in an ensemble of QDs grown using self assembly there is variation in dot size and composition between different dots. This leads to the observed spectrum from such QD systems being inhomogeneously broadened. Slight variations in the size of the dots change the energy of the quantum states in the dots and fluctuations in dot composition leads to variations in their individual bandgap energy, with both effects combining to inhomogeneously broaden the overall emission spectrum from a QD ensemble. Inhomogeneous broadening can be described by applying a Gaussian function in energy over the ensemble. For self-assembled dots grown by the Stranski-Krastanow method, inhomogeneous broadening is the dominant broadening mechanism [Sugawara, et al., 1997. Borri, et al., 2001. Osborne, et al., 2004]. Figure 2.5 is a schematic that illustrates the variations in dot sizes arising from Stranski-Krastanow growth.
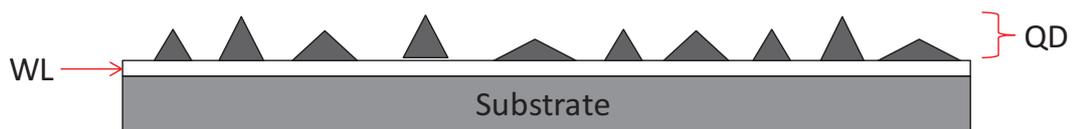

Figure 2.5. Schematic of QDs grown by the Stranski-Krastanow method illustrating the variation in dot sizes that occur from this growth mode.

2.4.3. Optical absorption and modal gain.

For bulk, quantum well, and quantum wire systems optical gain is calculated using Fermi's Golden Rule [Coldren and Corzine, 1995] which considers transitions from a discrete energy state to a continuum of energy states using the appropriate density of states function for the system under consideration. This approach is not valid for QD systems however as no such continuum of energy states exists within the dots. Carriers in the ensemble of dots are fully localised at each dot so recombination of an electron and hole can only occur if they exist in the same dot. This spatial selection means that the energy states are not extended over the whole ensemble and so cannot be combined to form a joint density of states. Instead individual envelope functions must be defined for each dot. Inspite of this, expressions for the modal gain of QD systems have been derived using a modified density of states [Asryan and Suris, 1996. Kirstaedter et al., 1996. Bimberg et al., 1997. Blood, 2000] which sufficiently describe many properties of these systems.

Here the approach described in [Blood, 2009] is used to determine the modal gain of an ensemble of QDs. To account for the localisation of carriers at individual dots, the interaction of a light within a single two energy level system is considered, this effectively models a single dot. In such a system the number of photons absorbed per unit time ($\Delta\Phi$) is given by Equation 2.9.

$$\frac{\Delta\Phi(h\nu)}{\Phi_o(h\nu)} = \frac{2 \times 4\pi\hbar}{cn\varepsilon_0\hbar\omega}\left(\frac{e}{2m_0}\right)^2 M^2 \left\{\int_{dot} F_1(\bar{r})F_2(\bar{r})dr\right\}^2 L(E_i, h\nu)$$

<div align="right">Equation 2.9</div>

where the incident optical flux is Φ_0, $F_2(r)$ and $F_1(r)$ are normalised envelope functions for the upper and lower state respectively, obtained by solving Schrodinger's equation for the QD potential. The factor 2 accounts for the spin degeneracy of the states. $L(E_i, h\nu)$ is a Lorentzian function that describes the homogeneous broadening of the transition about an energy E_i. The QD material has a refractive index n and optical matrix element M.

The terms on the right hand side of Equation 2.9 collectively have dimensions of [area] and represent the optical cross section of a single dot. The envelope functions indirectly relate the optical cross section of a dot to its dimensions. It is not possible

to characterise an absorption coefficient for a single QD as its dimensions mean that the distance light travels through each dot is much shorter than its wavelength. Instead an absorption coefficient for an ensemble of QDs with macroscopic dimensions is defined by assuming that the ensemble is made up of N_{dots} identical QDs per unit area. By multiplying Equation 2.9 by the N_{dots} an equation for the fraction of incident flux absorbed is obtained.

By integrating Equation 2.9 a term for the spectrally-integrated optical cross section $(\sigma_0(E_i))$ is obtained. The Lorentzian $(L(E_i,hv))$ is normalised so its integral is unity and so Equation 2.9 becomes

$$\frac{\Delta\Phi(hv)}{\Phi_o(hv)} = \sigma_0(E_i) \cdot L(E_i,hv)$$

Equation 2.10

The integrated cross section is independent of homogeneous broadening and simply a characteristic of the dot.

In an edge emitting laser device the light is guided over the dots along a cavity much longer than the wavelength of the light and so a modal absorption/gain coefficient can be defined along the axis of the waveguide. The coefficient for modal gain G is given by Equation 2.11.

$$G = \frac{1}{W}\frac{dW}{dL}$$

Equation 2.11

where W is the energy in the mode and (dW/dL) is the increase in energy per unit distance.

The increase in energy of the mode due to a single dot is given by Equation 2.12.

$$\frac{dW}{dL} = \sigma_0(E_i,hv)L(E_i,hv)A_{dot}^2(f_2 - f_1)$$

Equation 2.12

where A_{dot} is the vector potential of the optical field (A) at the layer of dots within the waveguide and f_2 and f_1 are the occupation probabilities of the upper and lower states

at an energy hv. W is obtained at any given point along the waveguide by integrating the square of the optical field across the waveguide (normal to the plane of the dot layer). Like absorption, the modal gain from a single QD cannot be defined so instead this is defined for an ensemble of identical dots by combining Equation 2.11 and Equation 2.12 and multiplying by N_{dots}. This gives Equation 2.13.

$$G(hv) = N_{dots}\sigma_0(E_i,hv)L(E_i,hv)\left[\frac{A_{dot}^2}{\int A^2(z)dz}\right](f_2 - f_1)$$

Equation 2.13

The term in the square brackets is defined as the reciprocal of the effective mode width w_{mod}. Equation 2.13 determines the modal gain per unit area for an ensemble of identical dots, however as discussed in section 2.4.2, an ensemble of QDs grown using self assembly exhibits an inhomogeneously broadened emission spectrum due to variations in dot sizes and compositions. To account for this inhomogeneity a Gaussian function ($P(E_i)$) is applied to Equation 2.13. This leads to an expression of the form in Equation 2.14.

$$G(hv) = \int \frac{N_{dots}\sigma_0(E_i,hv)L(E_i,hv)P(E_i)(f_2 - f_1)}{w_{mod}}dE_i$$

Equation 2.14

Using Equation 2.14 the modal gain spectrum for an ensemble of inhomogeneously broadened QDs states can be obtained and it takes account of the spatial localisation of carriers within each dot.

It is possible to relate Einstein's coefficient B, describing the total rate of absorption of photons in a two level system, to the integrated optical cross section of a dot system by considering the rate at which electrons are excited out of the lower energy level. Equation 2.15 describes the rate at which electrons (N) are lost from the lower energy level.

$$\frac{dN}{dt} = BN\rho(hv)$$

Equation 2.15

For broadband light incident upon a two level system with N electrons in the lower energy level, the incident photon flux is $\rho(h\nu) \times (c/n)$ photons per unit energy per unit time. The total rate of absorption defined by the integrated optical cross section is therefore

$$R_{up} = N\left[\rho(h\nu)\frac{c}{n}\right]\sigma_0$$

Equation 2.16

So by relating this to the rate of upward transitions, Equation 2.15, and accounting for the spin degeneracy of the states it is seen that

$$B = \frac{1}{2}\left(\frac{c}{n}\right)\sigma_0$$

Equation 2.17

Substituting this into Equation 2.7 gives

$$A_{21} = \frac{1}{2}\frac{8n^2(h\nu)^2}{h^3c^2}\sigma_0$$

Equation 2.18

So the spontaneous lifetime of a carrier in a dot can be determined from its integrated cross section.

2.4.4. Spontaneous emission.

The spontaneous rate from a two energy level system was given in section 2.3.2 and is repeated here in Equation 2.19 with the spin degeneracy of the state accounted for.

$$R_{spon} = 2A_{21}f_2(1-f_1)$$

Equation 2.19

Using Equation 2.18, Equation 2.19 can be related to the integrated cross section of a single dot (i.e two level system) giving Equation 2.20. To account for the homogeneous broadening a Lorentzian function is included.

$$R_{spon}(h\nu) = \frac{8n^2(h\nu)^2}{h^3c^2}\sigma_0(E_i,h\nu)L(E_i,h\nu)f_2(1-f_1)$$

<div align="right">Equation 2.20</div>

To determine the spontaneous emission from an ensemble of N_{dot} QDs Equation 2.20 is integrated over all dot states to give Equation 2.21. Inhomogeneous broadening is accounted for by applying a Gaussian function to this equation.

$$R_{spon}(h\nu) = \frac{8n^2(h\nu)^2}{h^3c^2}\int N_{dots}\sigma_0(E_i,h\nu)L(E_i,h\nu)P(E_i)f_2(1-f_1)dE_i$$

<div align="right">Equation 2.21</div>

2.4.5. Fermi-Dirac statistics and population inversion.

Throughout this chapter occupation probabilities have been used to describe occupation of QD states when calculating absorption, gain and spontaneous emission. In some cases, the system as a whole can be considered using statistical physics to describe these occupation probabilities. This method is used to describe the most likely distribution in energy, of carriers within a QD system made up of broadened energy states.

In thermal equilibrium the probability that an electron, which obeys the Pauli Exclusion Principle, occupies a state of energy E is described using Fermi-Dirac statistics [Coldren and Corzine, 1995]. Equation 2.22 determines the occupation probability f_i of a state i at energy E_i using Fermi-Dirac statistics.

$$f_i = \frac{1}{e^{\frac{E_i-E_F}{kT}}+1}$$

<div align="right">Equation 2.22</div>

where E_F is the Fermi level of the system, k is Boltzmann's constant and T is temperature. When a system is in thermal equilibrium, the rates of excitation and relaxation of carriers between two states are equal. For lasing action to occur in a two state system, stimulated emission must dominate and so there must be more carriers in the upper state. For this to occur, additional carriers must be continuously injected into the upper state, via electrical or optical pumping, taking the system out

of thermal equilibrium. Under these conditions the population of carriers is said to be inverted and the term quasi-Fermi level replaces E_F in Equation 2.22.

2.4.6. Population inversion factor.

The probabilities of occupancy of the upper and lower state involved in a transition appear in the expressions for modal gain and spontaneous emission. By taking the ratio of these two quantities the degree of inversion of the system can be determined. This ratio is shown in Equation 2.23.

$$\frac{G^p(hv)}{I_{spon}(hv)} = \left\{ \frac{3\pi^2 \hbar^3 c^2}{n^2 (hv)^2} \cdot \frac{1}{\omega_{mod}} \right\} \left[\frac{f_2 - f_1}{f_2(1-f_1)} \right]$$

Equation 2.23

where $I_{spon}(hv)$ is the total spontaneous emission rate of light of a single polarisation. The quantity in the square bracket is defined as the population inversion factor (P). It only consists of occupation probabilities and can range from a value of 0 to 1, unity is achieved if, in a two state system, the upper state is fully occupied ($f_2 = 1$) or if the lower state is empty ($f_1 = 0$). When both these conditions are met the system is said to be fully inverted.

If the system can be described by global occupation probabilities which are in quasi-thermal equilibrium then P can be determined using Fermi-Dirac statistics and is of the form in Equation 2.24.

$$P = 1 - \exp\left(\frac{E - \Delta E_f}{kT} \right)$$

Equation 2.24

where E is the photon energy and ΔE_f is the quasi-Fermi level separation. So by studying the modal gain and spontaneous emission from a system it is possible to determine the form of the carrier distribution within the system.

2.4.7. Carrier distribution – thermal and non-thermal.

It has been discussed how dots grown through self assembly are coupled to a quantum well known as a wetting layer. Therefore the dots cannot be regarded as an

isolated system and so consideration of a global dots plus wetting layer system must be used in the analysis of QD laser material.

The wetting layer acts as a reservoir of carriers for the dots and exchange of carriers constantly occurs between the two. This exchange occurs through capture and emission of phonons with energies equivalent to the energy separation of the dot and wetting layer states, typically of the order of 200 meV. This phonon interaction means that this process is strongly affected by the temperature of the structure. However, the process can also be influenced by dot composition and size that change the energy separation between dot and wetting layer states. The rate of escape of carriers to the wetting layer and recombination rates determines how carriers are distributed throughout the available states of the system. Figure 2.6 shows a schematic illustration of the interaction of carriers in the wetting layer with the inhomogeneous distribution of dot states in QD materials.
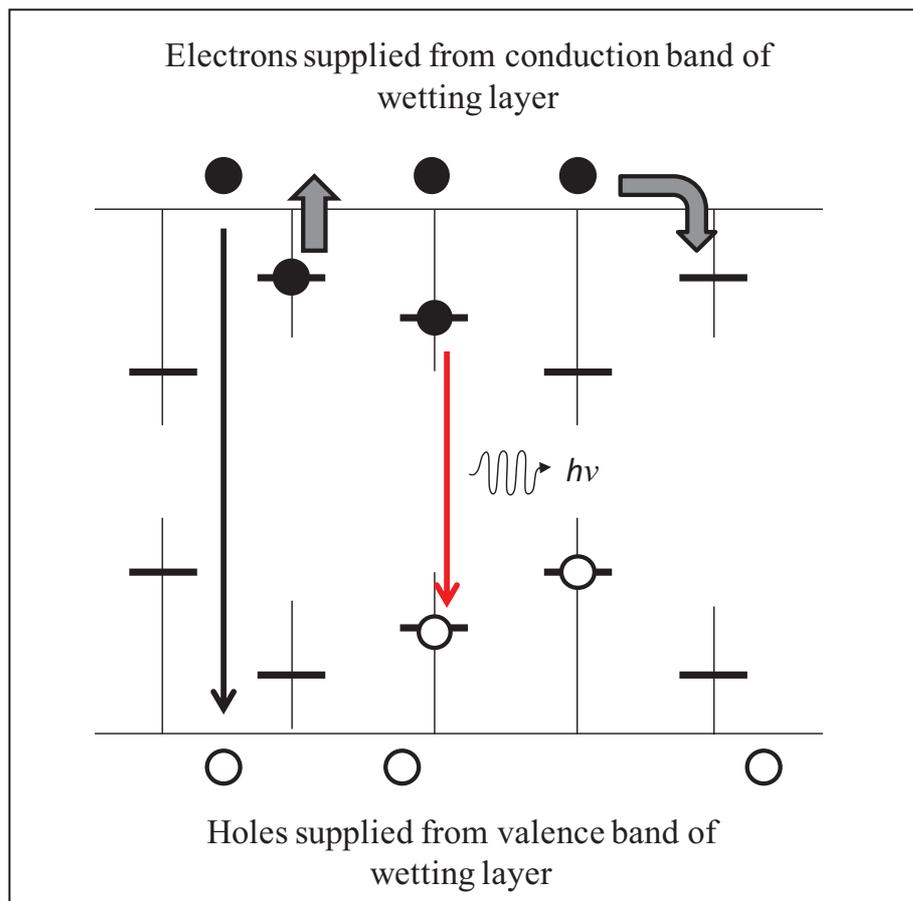

Figure 2.6. Schematic illustration of the interaction of carriers in the WL with the inhomogeneous distribution of QD states, showing processes of capture and emission of carriers into the dots from the WL and recombination between QD states containing an electron and a hole.

If the rate of escape is faster than the rate of recombination then carriers can be emitted and recaptured from the wetting layer into the dots before they recombine. This means that carriers can reallocate themselves amongst the dots and so a thermal equilibrium is established between the dots. Under thermal equilibrium the probability of occupancy of a dot state is dependent on its energy. Fermi-Dirac statistics can be applied to the distribution and electron and hole quasi-Fermi levels can be defined for the whole system.

If however, the rate of recombination from the dots is significantly faster than the thermal excitation and relaxation of carriers from the wetting layer states then the distribution of carriers within the QDs becomes random provides that capture into the dots is random. Under these conditions carriers cannot reallocate themselves between dots before they recombine and so are uncoupled from each other. This means that all dots are occupied with the same occupation probability and so it is not appropriate to apply Fermi-Dirac statistics to the system.

These two conditions of occupation are the extreme cases and several factors mean that the situation can easily be somewhere between the two. One of these factors is the presence of excited states within the QDs, which influences the rate of thermal emission of carriers and adds an additional recombination process. It must also be remembered that the electron and hole states have different energies within the same dot due to the different effective masses associated with these states. The characterisation and understanding of carrier distributions throughout QD systems is a key part of this thesis.

2.5. Important definitions.

Section 2.4.7 described the different possible ways in which carriers occupy the states within a QD sample. Throughout this thesis three phrases will be used to describe the nature of the carrier occupation within the QD samples. The definitions provided here for these phrases describe the context in which they should be interpreted, unless otherwise stated.

- **Thermal occupancy** – the QD and wetting layer states are all in thermal equilibrium and occupation of all states can be described by a global Fermi-Dirac distribution in energy.

- **Non-thermal occupancy** – Occupation within any given dot is dependent on energy and can be described by a Fermi-Dirac distribution. However, the temperature describing each dots distribution does not match that of the lattice.

- **Random Occupancy** – QD states are decoupled from the wetting layer states. The rate of recombination from the dots is significantly faster than the thermal excitation of carriers to the wetting layer so carriers cannot redistribute between spatially separated QDs. Capture into a QD is independent of energy whist emission is dependent on energy so now emission is eliminated, carriers are distributed independently of energy across the dot states.

2.6. Summary.

In summary, this chapter has provided the relevant theory required to understand and explain the experimental results shown in the subsequent chapters of this thesis. The impact that the Stranski-Krastanow growth method has on the properties of QD devices has been discussed in detail as this is particularly important to the content of this work.

Chapter 3. Experimental procedure.

3.1. Introduction.

In this chapter the experimental techniques used to obtain the results for this thesis are outlined. Details of the materials investigated are given and it is discussed how these are processed into devices from which measurements can be made. The equations used to analyse these materials will be derived, outlining the assumptions made and examples of experimental results obtained using these equations are shown. The device checks required to ensure that those assumptions are made will be described and details of the experimental apparatus used to measure those devices are given.

3.2. The segmented contact method.

The segmented contact method [Thomson, et al., 1999] employs the measurement of single pass, edge emitted amplified spontaneous emission (ASE) for varying pump lengths to obtain modal gain spectra, modal loss spectra and spontaneous emission spectra [Blood, et al., 2003]. From these spectra it is possible to characterise laser materials properties including radiative and non-radiative current density, overall internal quantum efficiency and carrier population distributions. This technique is advantageous over other techniques as it allows for measurement of modal absorption in real units, vital for identifying the optical transitions of a material. In addition, measurements can be made at high carrier densities where carrier-carrier interactions can be investigated.

3.2.1. Test device Structure.

The materials described in this work were processed by Mrs Karen Barnett, into test structures designed for the segmented contact method. These devices consist of an edge emitting laser structure with a 50 μm oxide isolated stripe. A 4μm separation in the p-contact and GaAs capping layer is formed every 300 μm and then cleaved into 1500 μm long devices, creating a test structure with five 300 μm long sections where the carrier leakage between them has been limited to such an extent that they can be pumped separately. This test device is illustrated in Figure 3.1.(a) and a photo of a

test device is shown in Figure 3.1. a) Segmented contact test structure.(b). In this implementation of the segmented contact method the front two sections, described as sections 1 and section 2, are electrically excited to provide the ASE for measurement. They can be driven individually or together to provide a gain length of *L* and *2L*. Details of how the measured ASE from these sections is used to provide gain, absorption and spontaneous emission spectra are described in Sections 3.2.2 to 3.2.4. The three back sections provide passive absorption to prevent round trip gain. To further ensure that round trip gain is suppressed the latter sections can have a reverse bias applied to them and the rear facet of the device can be damaged to prevent reflections along the gain guided region.

a)

b)
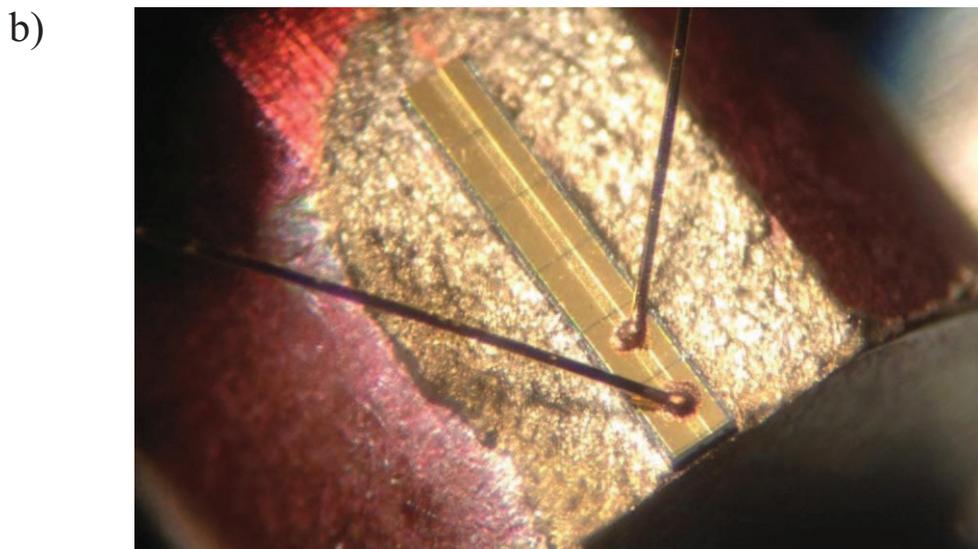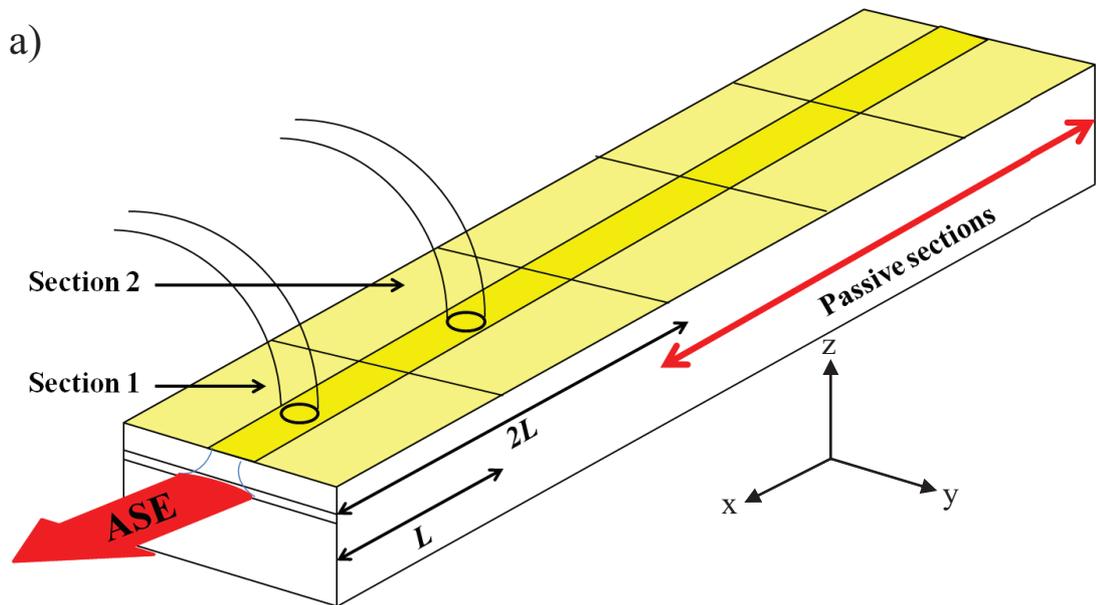
Figure 3.1. a) Segmented contact test structure. b) Photo of a test device.

3.2.2. Measured amplified spontaneous emission.

If the total spontaneous emission rate of light of a single polarisation is I_{spon} per unit area per unit energy interval then the ASE ($I(x)$) from a section of length Δx, a distance x from the beginning of the pumped length, is given by Equation 3.1.

$$I(x) = \beta I_{spon} e^{(G-\alpha_i)x} \Delta x$$

<div align="right">Equation 3.1</div>

where β is the fraction of spontaneous emission coupled into the waveguide, G is the modal gain and α_i is the intrinsic loss due to photon scattering within the waveguide. Assuming that I_{spon} is uniform along the entire pumped length then the total ASE $I(L)$ from a stripe of length L is given by Equation 3.2.

$$I(L) = \int_0^L \beta I_{spon} e^{(G-\alpha_i)x} dx = \beta I_{spon} \left(\frac{e^{(G-\alpha_i)L} - 1}{G - \alpha_i} \right)$$

<div align="right">Equation 3.2</div>

The ASE ($I_{meas}(L)$) measured from the front facet of this stripe length is given by Equation 3.3 and has arbitrary units.

$$I_{meas}(L) = CI_{ext}(L) = C(1-R)I(L)$$

<div align="right">Equation 3.3</div>

where R is the reflectivity of the air-semiconductor boundary at the front facet and C is an extraction factor due to conversions in the measuring devices. This extraction factor includes contributions from collection geometry, spectral response and an overall calibration factor. Determining C is necessary to obtain spontaneous emission in real units and will be discussed in Section 3.2.4.

Considering measurement on the segmented contact sample described above in section 3.2.1, ASE can be obtained from three electrical drive conditions, when Section 1 is pumped alone resulting in ASE from length L, when section 1 and 2 are pumped together resulting in ASE from length $2L$, and finally when section 2 is pumped alone resulting in ASE identical to that from section 1 but passing through

an absorbing length L (Section 1). $I_{meas}(L)$ can then be represented for these three situations giving Equation 3.4, Equation 3.5 and Equation 3.6.

$$I_{meas}(1) = C(1-R)(\beta I_{spon})\frac{e^{(G-\alpha_i)L}-1}{G-\alpha_i}$$

Equation 3.4

$$I_{meas}(1+2) = C(1-R)(\beta I_{spon})\frac{e^{(G-\alpha_i)2L}-1}{G-\alpha_i}$$

Equation 3.5

$$I_{meas}(2) = C(1-R)(\beta I_{spon})\frac{e^{(G-\alpha_i)L}-1}{G-\alpha_i}[e^{(-A-\alpha_i)L}]$$

Equation 3.6

where A is modal absorption. Examples of ASE measured in this way for the three conditions described are shown below in Figure 3.2.
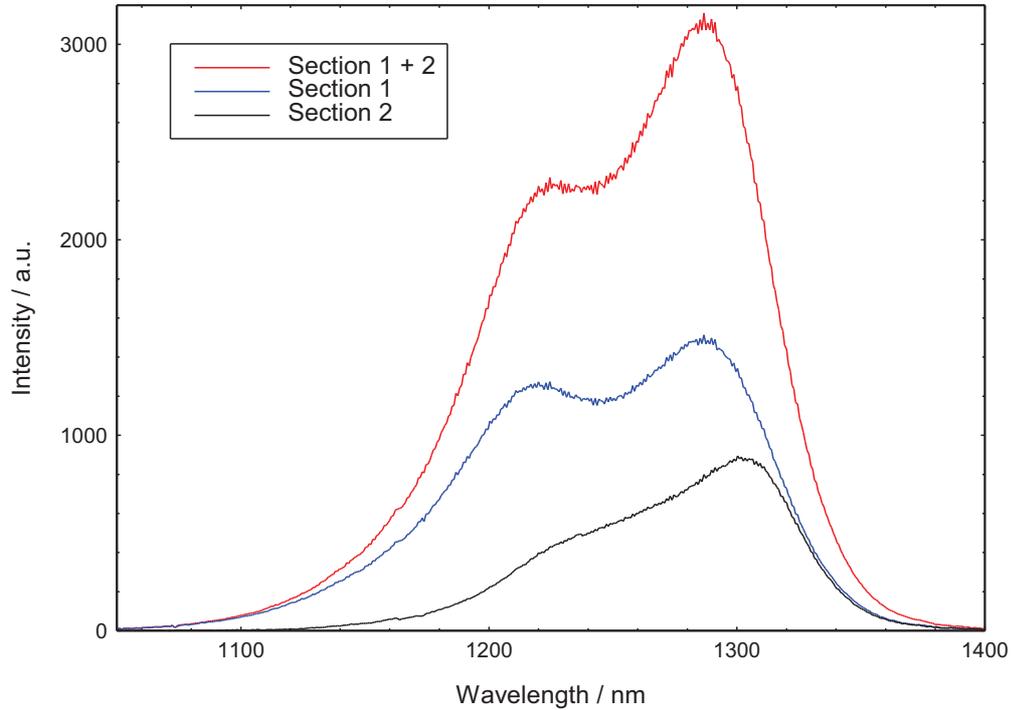

Figure 3.2. ASE measured from the front facet of segmented contact test structure. Red - ASE when section 1 and 2 pumped, Blue - ASE when section 1 pumped alone, Black - ASE when section 2 pumped alone.

3.2.3. Net Modal Gain and Absorption.

By comparing the ASE from multiple pump lengths, it is possible to obtain the net modal gain and absorption spectrum of a material. In the experiment described above in section 3.2.2, by comparing the ASE from lengths L and $2L$, it can be shown that Equation 3.7 can be derived from Equation 3.4 and Equation 3.5.

$$G - \alpha_i = \frac{1}{L} \ln \left(\frac{I_{meas}(1+2)}{I_{meas}(1)} \right)$$

Equation 3.7

In a similar fashion ASE from sections 1 can be compared with ASE from section 2 to obtain the modal absorption spectrum of the material being measured. Equation 3.8 for the modal absorption is derived by combining Equation 3.4 and Equation 3.6.

$$(A + \alpha_i) = \frac{1}{L} \ln \left(\frac{I_{meas}(1)}{I_{meas}(2)} \right)$$

Equation 3.8

The equations derived here for net modal Gain and Absorption only apply if the assumptions in the segmented contact method calculations are met, so the section lengths must be identical and have the same current density applied during measurement. The resistance of the contact break between the sections must be sufficiently high such that carrier leakage does not increase the pumped section length. Finally ASE measured from the facet must be from light coupled into the waveguide and amplified so a lens with a sufficiently narrow collection angle must be used to focus the light onto the detector.

Examples of net modal Gain and Absorption obtained using Equation 3.7 and Equation 3.8 from measurements of ASE measured on an InAs quantum dot sample are shown in Figure 3.3. If the low energy side of Figure 3.3 is considered it is observed that the net modal gain and absorption spectrum converge at energies below that of the bandgap, where there are no absorbing states. Here the internal optical loss (α_i) of the material is obtaned as in this region any loss in signal intensity is purely due scattering losses and free carrier absorption within the sample. If α_i has no spectral dependence then it can be added to the measured spectra to obtain the

modal gain and absorption of the material. The transparency point (TP) for a material is defined when the gain matches the losses and this is equivalent to the quasi-Fermi level separation (ΔE_f) for a system in thermal equilibrium, where the photon energy must be greater than ΔE_f for gain to occur. The TP is shown on Figure 3.3 where the net modal gain is zero at high energies where states exist. ΔE_f can be used as a measure of the level of injection within the sample by subtracting the TP from some reference energy (giving ΔE) that is fixed at all injection levels used within the measurement. This is illustrated in Figure 3.3 where the reference energy is given by the first absorption spectra peak.
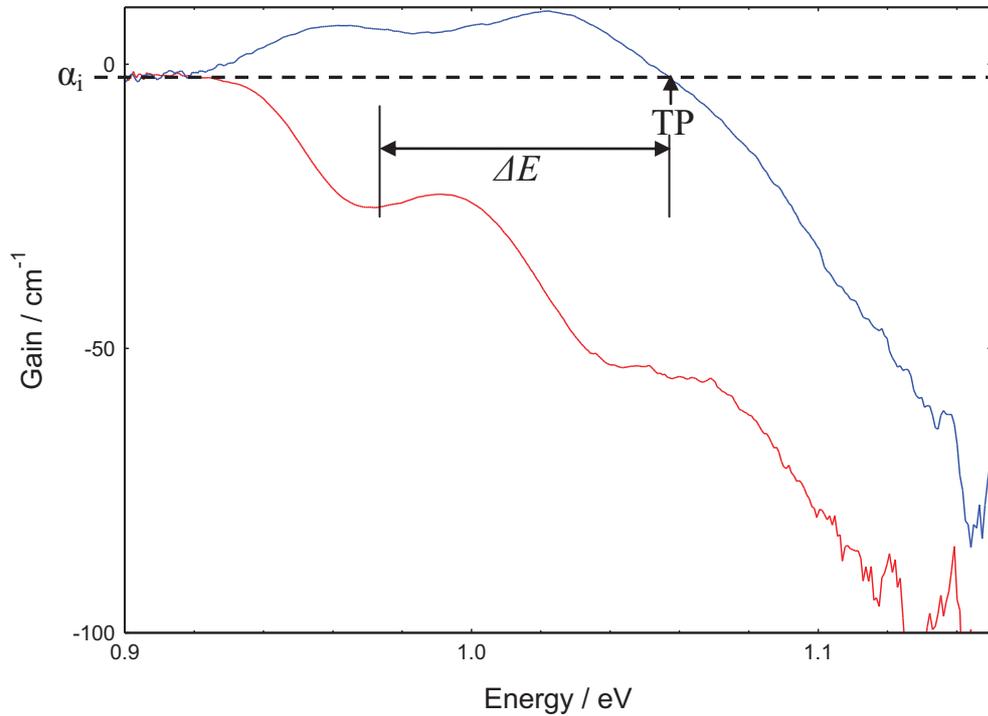
Figure 3.3. Net modal gain (blue) and absorption (red) spectrum measured for the p-doped InAs sample at 300 K with a current density of 533 Acm^{-2} applied to each section.

3.2.4. Population function and calibrated spontaneous emission.

It is also possible to obtain the unamplified spontaneous emission (I_{spon}) using the segmented contact method. The measured gain is used to effectively correct the ASE for the amplification along the waveguide, so Equation 3.7 is substituted into Equation 3.4 to give Equation 3.9 from which I_{spon} can be determined in real units if the collection geometry can be determined and only spontaneous emission coupled into the waveguide is measured.

$$\beta I_{spon} = \frac{1}{C(1-R)} \times \left[\frac{I_{meas}(1)^2}{I_{meas}(1+2) - 2I_{meas}(1)} \times \frac{1}{L} \ln\left(\frac{I_{meas}(1+2)}{I_{meas}(1)} - 1 \right) \right] = \frac{1}{C(1-R)} I_{spon}^{meas}$$

<div align="right">Equation 3.9</div>

The term in the square brackets of Equation 3.9 is the measured unamplified spontaneous emission (I_{spon}^{meas}) extracted directly from measurements of ASE and has arbitrary units. An example of I_{spon}^{meas} measured using the segmented contact method is shown in Figure 3.4.
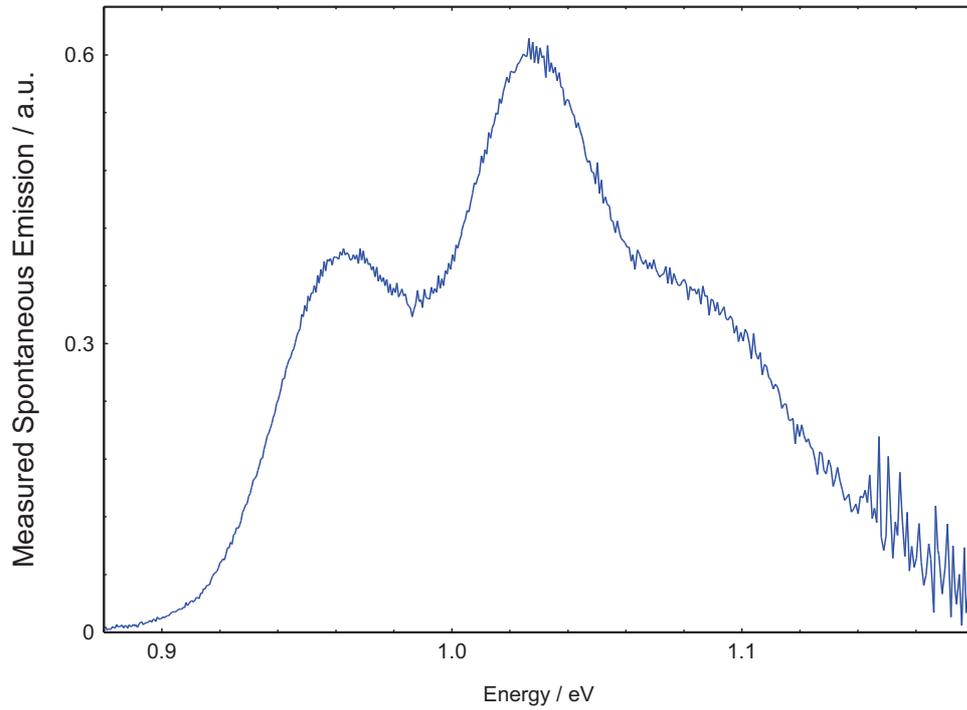
Figure 3.4. Measured spontaneous emission measured for the p-doped sample in arbitrary units.

As discussed above, it is possible to calibrate I_{spon} into units of photons per second per unit area per unit energy interval if the collection geometry of the system can be quantified. This is done using the population inversion factor (P) given in Equation 3.10.

$$P(hv) = \frac{f_2 - f_1}{f_2(1-f_1)} = \left[\frac{n^2(hv)^2}{3\pi^2 \hbar^3 c^2} \cdot w_{mod} \right] \left(\frac{G^p(hv)}{I_{spon}(hv)} \right)$$

<div align="right">Equation 3.10</div>

An overall calibration factor (C') is defined that relates the measured I_{spon}^{meas} to I_{spon} and this is given in Equation 3.11.

$$C' = \beta C(1 - R)$$

<div align="right">Equation 3.11</div>

This converts Equation 3.10 into Equation 3.12 which only contains measured quantities.

$$P(hv) = C'\left[\frac{n^2(hv)^2}{3\pi^2\hbar^3 c^2} \cdot w_{\text{mod}}\right]\left(\frac{G^p(hv)}{I_{spon}^{meas}(hv)}\right)$$

<div align="right">Equation 3.12</div>

Equation 3.10 shows that P is unity, when considering transitions between two states, if the upper state is fully occupied [$f_2 = 1$] or when the lower state is completely empty [$f_1 = 0$]. By dividing our measured G and I_{spon}^{meas} a measured population inversion factor (P_{meas}) of the form of Equation 3.13 is obtained.

$$P_{meas}(hv) = \left[\frac{n^2(hv)^2}{3\pi^2\hbar^3 c^2} \cdot w_{\text{mod}}\right]\left(\frac{G^p(hv)}{I_{spon}^{meas}(hv)}\right)$$

<div align="right">Equation 3.13</div>
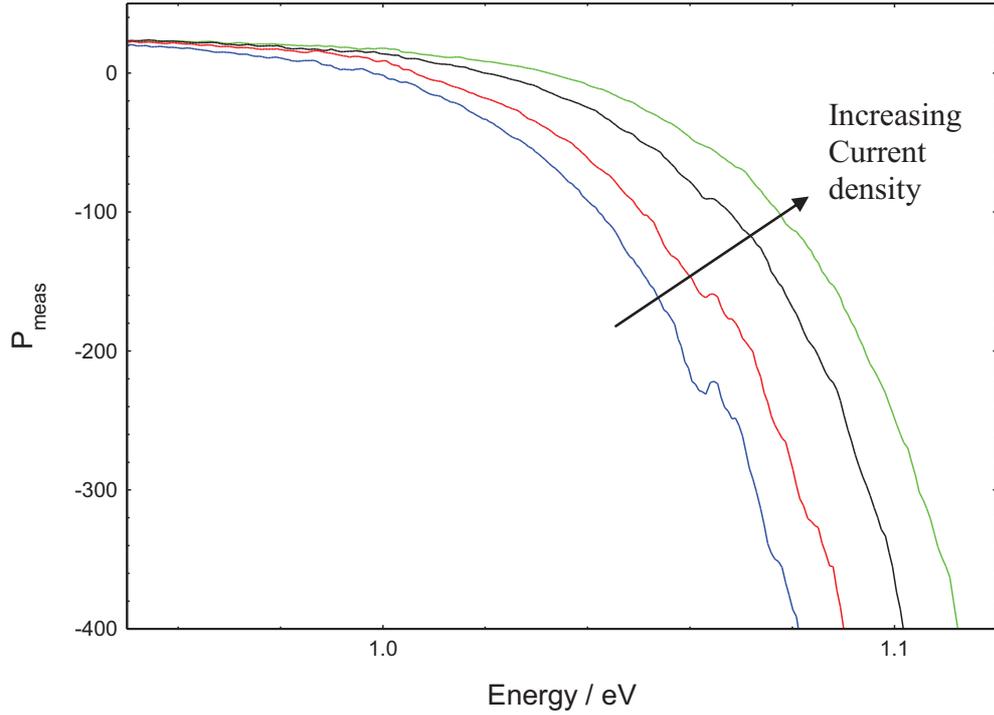
Figure 3.5. Measured Population inversion functions obtained for the p-doped sample at 300 K for injections levels of 166.6, 200, 266.6, and 333.3 Acm⁻².

Figure 3.5 shows P_{meas} obtained from ASE measurements for a range of injection levels. From these P_{meas} if a region can be identified where full inversion has occurred [$P = 1$] then C' can be obtained from the inverse of the P_{meas} at that point. All the P_{meas} shown in Figure 3.5 converge at the same maximum value at low photon energy. This saturation with respect to increasing injection shows that the upper state is fully occupied [$f_2 = 1$] or that the lower state is completely empty [$f_1 = 0$] or both are true which is full inversion. So C' can be been determined from Figure 3.5 and I_{spon} can be converted into real units by multiplying I_{spon}^{meas} by the inverse of C' as shown by Equation 3.9 and Equation 3.11. An example of I_{spon} converted into real units using this calibration process is given in Figure 3.6.
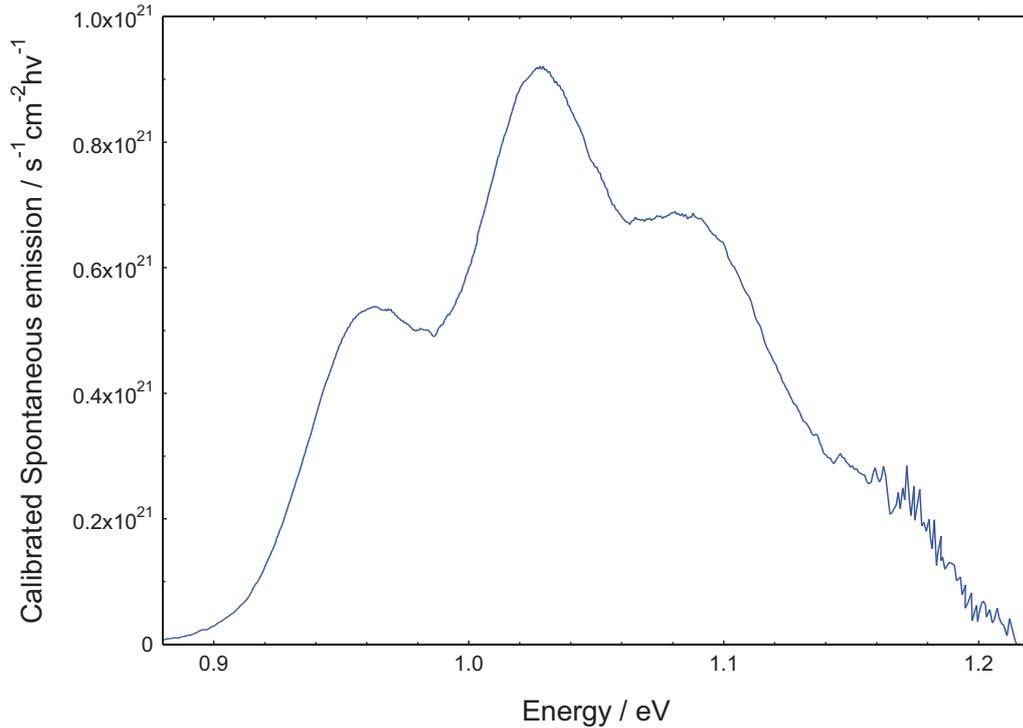
Figure 3.6. Spontaneous emission, in real units, measured for the TE mode the p-doped sample.

The I_{spon} shown in Figure 3.6 is for a single TE mode, as the spontaneous emission is defined for a single mode and so the ASE is always measured after it has passed through a polariser, so is for a specific mode. It is assumed that I_{spon} is identical for the two TE modes (TE_x and TE_y) and I_{spon} can be measured for the TM mode by repeating the ASE measurements using a polariser set to the TM position. The calibration must be performed for a specific polarisation, as opposed to an average overall polarisation, in order for the polarisation dependant matrix elements to be cancelled in the ratio of G to I_{spon}. Thus a separate calibration must be obtained for the TM mode measurements, as the measurement apparatus may have a polarisation dependant system response. By integrating $I_{spon}(hv)$ and multiplying by the charge on the electron (e) the radiative current from that polarisation can be determined and thus by combining the contributions from all three polarisations the total radiative current density is found for a given injection level. This is subtracted from the current applied to the sample to reach that level of injection in order to determine the non-radiative currents.

3.2.5. Device Checks.

Any device used to make segmented contact measurements must adhere to a specific set of requirements such that the assumptions made in the derivation of the equations in sections 3.2.2 to 3.2.4 are satisfied.

Before any measurements can be made on samples after they have been cleaved into the devices illustrated in Figure 3.1, they must be mounted onto copper blocks attached to transistor headers. This is so that they can be easily placed in cryostats and electrically driven. The first checks are made during this mounting process where a visual inspection of the front facet is completed before wires are attached to the device. The front facet must be mirror-like with no visible defects that could scatter emitted light. Also the gold adhesion to the top and bottom of the device must be inspected. There must be no areas where the gold has lifted off the semiconductor and it should have no discoloration. This ensures that uniform injection is applied to the samples waveguide during measurement.

Once a device has been mounted with wires attached for electrical pumping, the inter-contact resistance between the sections used during measurement must be measured. The resistance should be sufficiently high so that the sections are electrically isolated and current leakage into adjacent sections is negligible. The resistance must not be too high however. A high resistance is an indication that the contact breaks have been etched to deeply and this may affect the optical mode. Resistances of between 300 Ω and 1000 Ω are acceptable for segmented contact measurements.

Having completed these checks the next step is to measure the current vs. voltage (IV) characteristics of the two front sections used in the segmented contact measurements. The IVs from both sections should have diode characteristics under forward bias, with the same turn on voltage (V_d). Neither IV should have any unexpected features, such as sudden jumps in voltage or plateaus. The voltage difference between the two sections must be within 3% at the maximum current levels used within the segmented contact experiment. Differences between the IVs indicate that the resistance across the sections may be different, possibly caused by poor metallisation, or that there may be extra current paths within the device. The IVs of the two sections must be within this tolerance to ensure that the same current

is applied to each section during measurement and device tests have been completed to establish this 3% tolerance. Examples of IVs from one of the structures used in this thesis are shown in Figure 3.7. IVs measurements are performed pulsed using a 500 ns pulse width with a repetition rate of 5 kHz. ASE measurements are performed using these same conditions. These conditions give a duty cycle of 0.25% which is sufficiently small to prevent internal heating of the device during measurement.
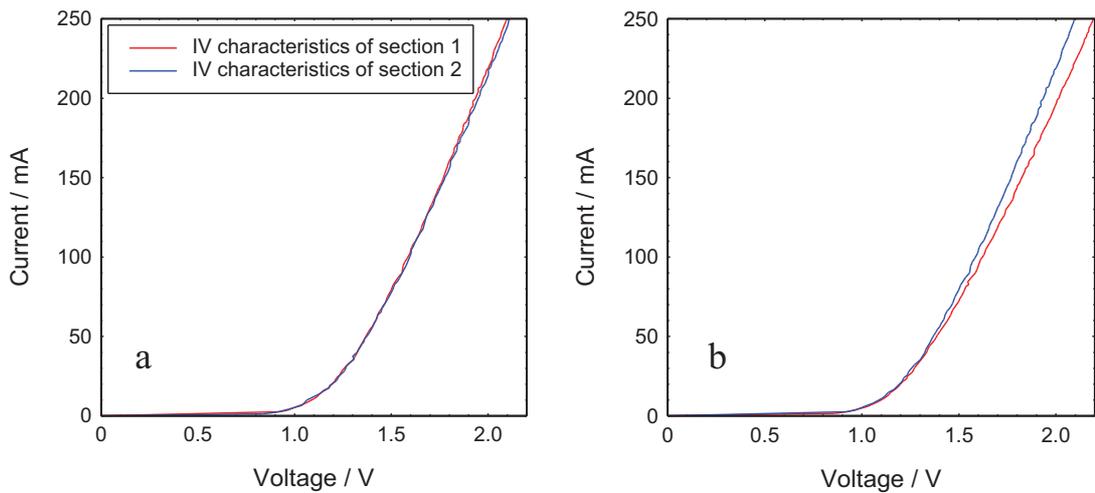
Figure 3.7. Examples of current versus voltage characteristics measured on a) a device with matching IVs and b) a device with IVs that are 10% different at 200 mA.

The last check that must be performed is to observe the near field emission from the facet. Nearfield measurement are made when driving section 1, section 2 and when driving both sections together. These near field measurements must have the same shape, width and position once normalised to the same intensity. This insures that the ASE measured under these three conditions is comparable and that the same current density is applied to each section during measurement. The near field measured when section 2 is driven can be up to 3% wider due to a lack of gain guiding of the optical mode in the un-pumped section 1. If this is the case then as long as the shape and position of section 2's near field is the same as the other two measurements then this width increase has no discernible effect, within the experimental error, in segmented contact measurements. It is also important to confirm that there is no filamentation apparent in the near field of the device; filamentation causes the near field to become non-uniform. Filamentation is a sign that current flows within the sample may be uneven. Non-uniformity in the near

field can also be created if there are defects on the front facet that were not visually apparent during the mounting process. These defects could scatter light and so some may be lost during measurement. Examples of near fields measured on one of the structures used for this thesis are given in Figure 3.8. The near field is also used to quantify the level of current spreading between the top contact oxide isolated stripe and the active region, this is taken as being the full width half max (FWHM) of the near field. The FWHM is an important quantity as it is used to convert pump currents into current densities so that comparisons can be made between materials as well as laser measurements.
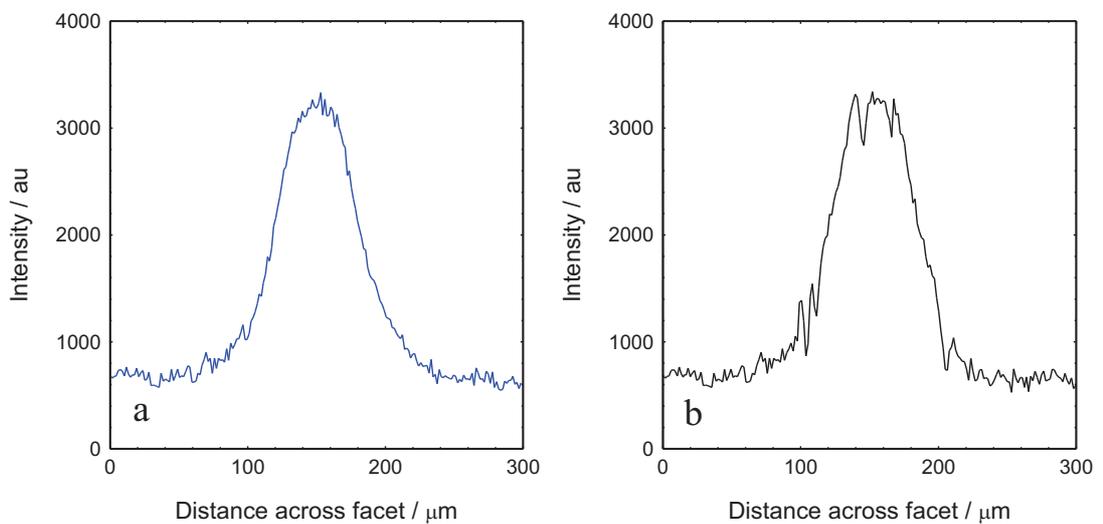
Figure 3.8. Measured near field for a) a sample with uniform (good) Gaussian emission across its facet and b) a sample with non-uniform (poor) emission across its facet.

3.3. Experimental setup.

All segmented contact measurements presented in this thesis were performed using an experimental setup initially developed by Dr. Craig Walker for measurement of threshold current and lasing wavelengths of laser devices as a function of temperature. The setup was then adapted by Dr. Deepal Naidu for measurement of ridge waveguide segmented contact devices down to liquid nitrogen temperatures. I have subsequently further adapted the collection geometry, vacuum system, device alignment stability and temperature calibrations for measurement on samples of the structure illustrated in Figure 3.1 down to liquid helium temperatures. A diagram

illustrating the setup used is given in Figure 3.9. Schematic of experimental apparatus used to measure ASE from segmented contact test structure.
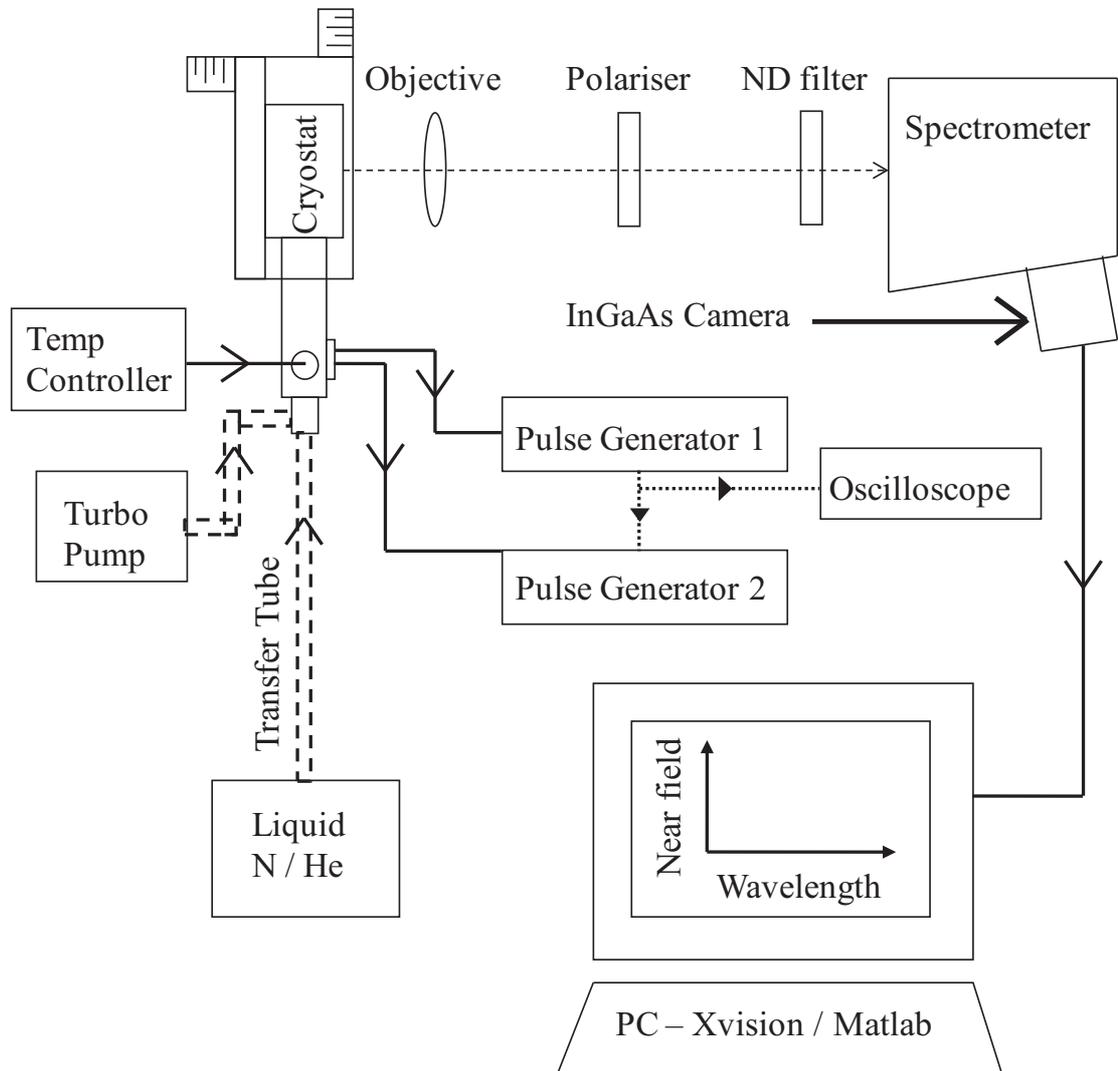
Figure 3.9. Schematic of experimental apparatus used to measure ASE from segmented contact test structure.

Once the device is mounted ready for electrical injection, as described in section 3.2.5, it is placed inside an Oxford instruments Heliostat[N] cryostat where sections 1 and 2 can be driven independently with two pulse generators. This means that the measurement is less sensitive to small differences in the IVs of the two sections as an independent current can be applied to each section individually. The current applied to each section is measured on an oscilloscope using a calibrated current probe. All segmented contact experiments in this thesis were performed under pulsed conditions with a duty cycle of 0.25% to prevent self heating of the device. The cryostat is mounted onto a micro-positioning stage that has 6 degrees of freedom designed so

that the device is placed in the centre of all rotational axes. This allows for the accurate alignment of the light from the facet of the device with long term stability such that no device drift occurs during measurement. The temperature within the cryostat is regulated using an Oxford instruments ITC601 temperature controller that regulates the flow of liquid cryogen onto a copper block within the cryostat that contains a heating element. The device is placed on a cold finger 5 cm away from this copper block and so below 100 K a temperature gradient exists between the device and the copper block. In order to obtain accurate temperature measurement below 100 K a Cernox resistor, calibrated for a temperature range between 1.4 K and 420 K, was positioned within 3 mm of the device on a copper plate used to secure said device in place. To ensure a good thermal contact exists and that the temperature of the sample is the same as that of the Cernox resistor, a thermal heat sink compound is applied between the device and the copper plate and the Cernox resistor is attached to the copper plate using a high thermal conductivity varnish. A four terminal resistance measurement system is used to measure the resistance of the Cernox resistor. These modifications allow for the stable measurement on segmented contact samples down to 20 K using liquid Helium.

The ASE emitted from the front facet of the device is collected by a lens with a numerical aperture (NA) of 0.13 such that the collection half-angle is less than the 8.4° degrees required for no un-pumped ASE to be collected [Lutti, 2005]. This lens focuses the ASE onto the entrance slits of a spectrometer with a NA matching that of the lens. The ASE passes through a polariser before reaching the spectrometer so that either TE or TM emission can be measured.

A Xenics Xeva 1.7-320 Infrared InGaAs camera is placed at the exit slits of the spectrometer for measurement of the ASE from the device. This camera is able to measure light with wavelengths between 800 nm and 1700 nm; however the spectrometer is only able to measure wavelengths up to 1400 nm. The diffraction grating of the spectrometer disperses light in the x-y plane such that the x-axis of the camera measures the ASE's wavelength. The device is orientated with respect to the spectrometer slits such that the y-axis of the camera measures the lateral near-field across the facet, the y-axis direction in Figure 3.1 (i.e. in the plane of the active region). The wavelength measurement from the camera is calibrated using the infrared transition lines of a He-Ne laser. The camera is controlled using Xvision

software, which integrates the light incident on the camera over a period of time defined by the user. Preliminary measurements showed that this light integration only becomes linear for times longer than 20 s; however the ASE intensities emitted from the segmented contact devices are sufficient to saturate the detector with integration periods of this order. To limit the light levels reaching the camera, neutral density (ND) filters are placed in the path of the light focused onto the spectrometer, with the level of filtering chosen to optimise the signal to noise ratio on the camera for the varying intensities of light emitted from the device. It is crucial that the amplitude response of the system is known for the wavelengths that can be measured, so that it can be compensated for within the analysis of the measurements. This is achieved by passing light from a source with a known spectral response, in this case an Oriel quartz tungsten halogen lamp from Newport, and comparing the measured response to that quoted by the manufacturer. This was used to determine the systems wavelength amplitude response for the entire optical path of the experimental setup. To ensure that response used to calibrate the measured ASE was always correct I repeated this system response measurement once all thesis results were completed and confirmed that this matched the original response measurement.

The Xvision software outputs the data from the camera as a text file containing an array of numbers associated with each pixel of the camera. I wrote a Matlab program to analyse the data outputted using the theory outlined in sections 3.2.2 to 3.2.4. The program integrates the ASE measured over a set number of pixels in the lateral near field plane where the user can define this pixel range as well as the part of the near field integrated over. The code stitches together camera images taken for multiple grating centre wavelengths, required due to the broad spectrum associated with the materials measured in this thesis, and then calibrates the ASE with respect to the system response. The modal gain, spontaneous emission and population inversion functions are then calculated and output to the user.

3.4. Material structure.

All the materials investigated in this thesis have InAs quantum dot active regions grown inside quantum wells to form a dot-in-a-well (D-WELL) structure and emit at 1.3 µm at room temperature. They were grown by Mark Hopkinson and Hui Yun Liu using solid source molecular beam epitaxy at the EPSRC III-V facility at the

University of Sheffield. The structures have nominally identical growth conditions except that they incorporate different modulation doping in the active region, both p and n-type, with one sample left un-doped for comparison. The general structure of the samples is given in Figure 3.10. The doped structures have Be (p-type) or Si (n-type) atoms within 6 nm of the GaAs spacer layer, placed 9 nm from the next D-WELL. Atomic force microscopy (AFM) measurements on un-capped samples grown under similar conditions determined that the dot density was 4.3×10^{10} cm^{-2} [Liu, et al., 2004] and this density was used to dope the samples to a level of approximately 15 dopants per dot. The samples were grown using "high growth temperature spacer layers" [Liu, et al., 2004].

1550 nm $Al_{0.4}Ga_{0.6}As$

25 nm GaAs

5x

50 nm GaAs

InAs dots on $In_{0.15}Ga_{0.85}As$ (8 nm)

75 nm GaAs

1550 nm $Al_{0.4}Ga_{0.6}As$
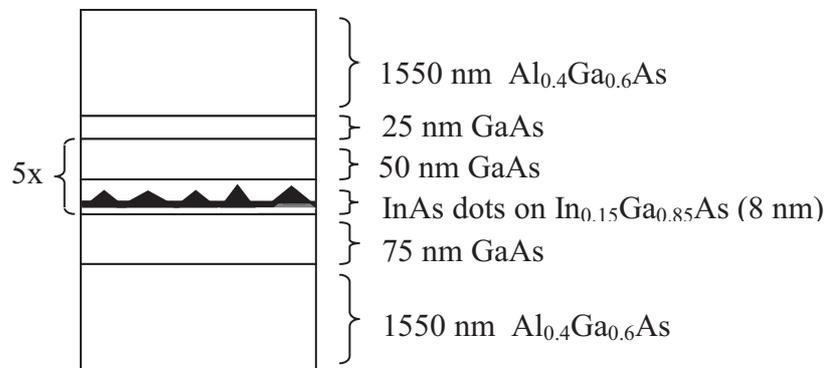
Figure 3.10. General structure of samples investigated in this thesis. Be atoms for p-type doping, Si atoms for n-type doping, over 6 nm of the 50 nm GaAs spacer layer, placed 9nm from next DWELL.

3.5. Summary.

In summary, this chapter has outlined the segmented contact technique and shown how this can be used to obtain the modal gain, absorption and spontaneous emission of a material, all in real units, simply from measurement of edge emitted ASE. The subsequent results chapters utilize this technique to fully characterise the complex nature of carrier population in quantum dot materials by observing how the quantities derived in this chapter evolve with injection.

Chapter 4. Modulation doping in InAs Quantum Dots.

4.1. Introduction.

In this chapter the measurements made on the three quantum dot structures, two containing modulation p and n type doping and one un-doped comparator structure, are described. All measurements shown in this chapter use the technique outlined in chapter 3 and give an overview of the characteristics of the three structures. Subsequent chapters will utilise novel methods of interpretation to explain the observations made throughout this chapter.

4.2. Motivations for incorporating modulation doping.

QD lasers were first proposed as a structure that would yield near ideal laser threshold performance due to the fact that only a single electron-hole pair would be required to reach transparency in a two state system [Arakawa and Sakaki 1982, Asada, et al., 1986, Vahala, 1988]. In self assembled In(Ga)As QD-wetting layer materials there is an inherent inhomogeneous broadening. In such systems, thermal occupation spreads carriers over a wider energy range with increasing temperature thus increasing the carrier density needed for threshold. In addition to this in III-V materials the valence mass is much larger than the corresponding conduction mass, meaning there exists a greater number of closely spaced hole states than electron states in these QD systems. This leads to a large asymmetry in the movement of the quasi-Fermi levels. In the QDs the electron quasi-Fermi level lies within the electron dot states, leading to high occupation, however the hole quasi-Fermi level is above the hole dot states. This leads to a very low occupation probability of holes in the QD states thus heavily limiting the level of gain achievable.

In quantum well (QW) materials the asymmetry of the quasi-Fermi levels was reduced using compressive or tensile strain leading to improved laser performance, including lower threshold current densities [Chand, et al., 1991, Turner, et al., 1998]. However, in QD materials it is not easy to engineer the levels of strain required to overcome the asymmetry due to the self-assembly growth process. The inclusion of

p-type modulation doping was also proposed as a means of overcoming the asymmetry of the quasi-Fermi levels in QW materials [Vahala and Zah, 1988]. Modulation doping places acceptor or donor ions (p-type or n-type doping) into the barrier region close to the active region. Providing there is sufficient thermal energy, these are ionised into the barrier, then fall into the active region. In the case of p-type doping this would fill the hole states and allow greater gain levels to be achieved. However, to reach a reasonable population of additional carriers in the active region a much larger number of ions than the number of states in required, as not all acceptor atoms are ionised and each state can accommodate two carriers due to spin degeneracy. In QW materials, where there are a large number of states, very high levels of doping are required which leads to adverse effects such as increased optical mode loss and non-radiative recombination. It was realised however, that p-type modulation doping would be beneficial [Takahashi, et al., 1988] for QD systems as lower doping levels would be required due to the fewer available states [Shchekin, et al., 2002].

P-type modulation doped In(Ga)As QD lasers have been studied by several groups [Otsubo, et al., 2004, Fathpour, et al., 2004, Mikhrin, et al., 2005] and are the source of particular interest due to reports of temperature insensitive thresholds and improved modulation bandwidths. Modelling of p-type modulation doped QDs has been reported [Deppe, et al., 2002] and this predicted the reduced threshold current and improved modulation response being due to an increased peak modal gain and differential gain and this has been shown to be consistent with experimental data, including laser wavelength measurements as a function of cavity length [Shchekin, et al., 2002]. It has been suggested however, that the positive effects of p-doping are limited at best as groups have reported increased threshold current density which they ascribed to be due to increased non-radiative recombination, when compared to intrinsic materials [Fathpour, et al., 2004, Mikhrin, et al., 2005].

4.3. Characterisation of samples

The samples detailed in section 3.4 were investigated using the segmented contact method outlined in chapter 3. From these measurements modal absorption, modal gain and spontaneous emission spectra were obtained from the un, p and n-doped samples so that comparisons can be made. The next sections will outline these

comparisons and give examples of results used in the analysis shown in the subsequent chapters in this thesis.

4.3.1. Modal Absorption.

The absorption measurements shown in this section were completed using the method outlined in section 3.2.3, but to ensure that carriers generated by absorption are rapidly removed, a reverse bias is applied to the un-pumped section during measurement. This voltage extracts the excess carriers present in the dot states so they do not impede the absorption of further carriers by Pauli state blocking. For each sample the modal absorption was measured for increasing reverse bias voltages until a level was reached where the modal absorption did not change for further increases in reverse bias. It was found that at 300 K a reverse bias of 2 V was sufficient to achieve this in all three samples. Modal absorption spectra obtained for the three samples measured when a 2 V reverse bias is applied to the un-pumped section are given in Figure 4.1.
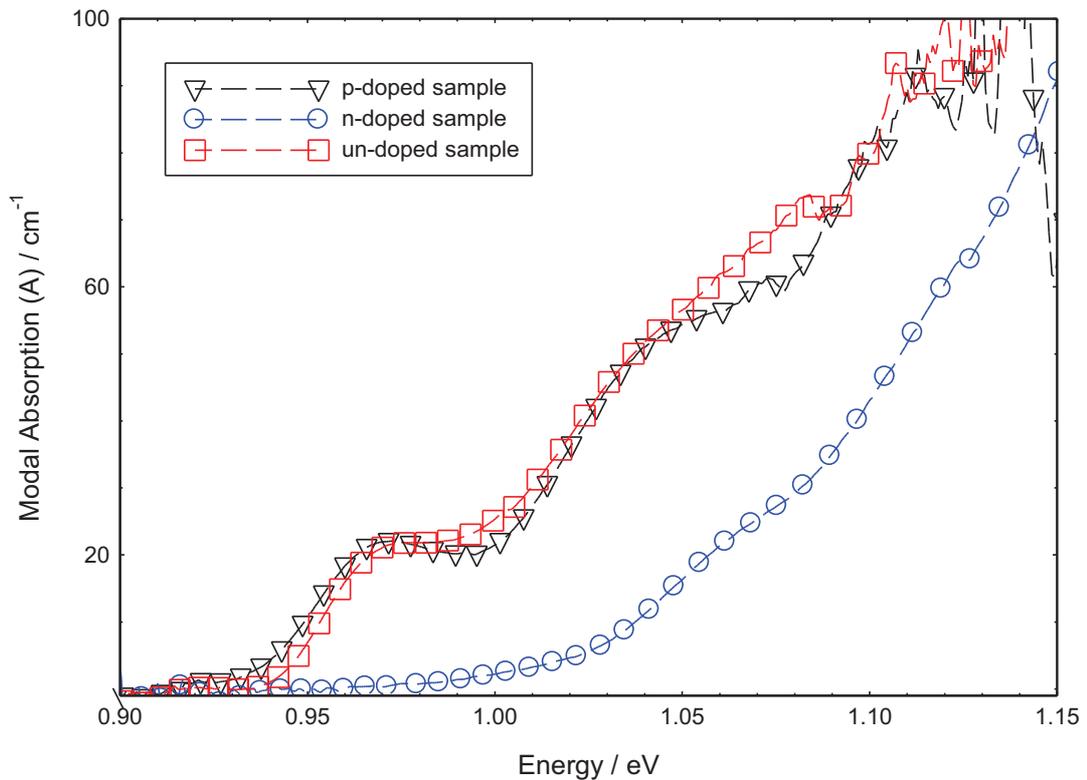

Figure 4.1. Modal absorption as a function of photon energy, with a 2 V reverse bias applied, for the un-doped (red squares), p-doped (black triangles) and n-doped (blue circles) samples.

Several interesting conclusions can be drawn from these results. In both the un-doped and p-doped sample the states associated with the ground and excited states of the QDs occur at the same energy, 0.975 eV for the ground state (GS) and 1.06 eV for the excited state (ES), and all states exhibit similar broadening and absorption amplitude. From these observations It can be concluded that the electronic dot states of the un-doped and p-doped samples are the same and thus the growth of the quantum dots is unaffected by the incorporation of p-type dopant. The measured modal absorption for the n-doped sample is very different to that of the un and p-doped samples. It appears that in this sample the QD states have been shifted to higher energies and significantly broadened. So from these observations It must concluded that the growth of the quantum dot layer has been affected by the inclusion of n-type dopant.

In order to fully characterise these modal absorption spectra, Gaussian distributions, in energy, representing inhomogeneously broadened quantum dot states were fitted to the measured modal absorption spectra shown in Figure 4.1. There is evidence from previous work using transmission electron microscopy (TEM) [Anders, et al., 2002] and photoluminescence measurements [Schmidt, et al., 1998 and Zhang, et al., 2001] to study InAs QDs that show a bimodal size distribution was exhibited in these dots. AFM measurements [Liu, et al., 2004 and Walker, at al., 2003] made on wafers grown under similar conditions to the samples studied here, suggested that they also had a bimodal size distribution consisting mostly of 'large' dots with a subset of 'small' dots. These measurements also showed that the GS transition of the smaller dot subset was similar to that of the ES transition energy of the large dot subset. In order to have complete confidence in any fit however, it must first be assumed that in these samples there is simple one subset of QDs. If this approach requires unrealistic fitting parameters then this is evidence that these QDs have a bimodal distribution of dot sizes. So assuming a monomodal distribution of QDs exists within the sample's three Gaussians representing the GS, ES and second ES of the distribution are fitted. Figure 4.2 shows the modal absorption spectrum of the p-doped sample where the sum of the three fitted Gaussians gives good agreement with the measured data. The high energy measured data is not considered as the experimental error associated with these points is large due to the lack of signal measured where the absorption is significant.
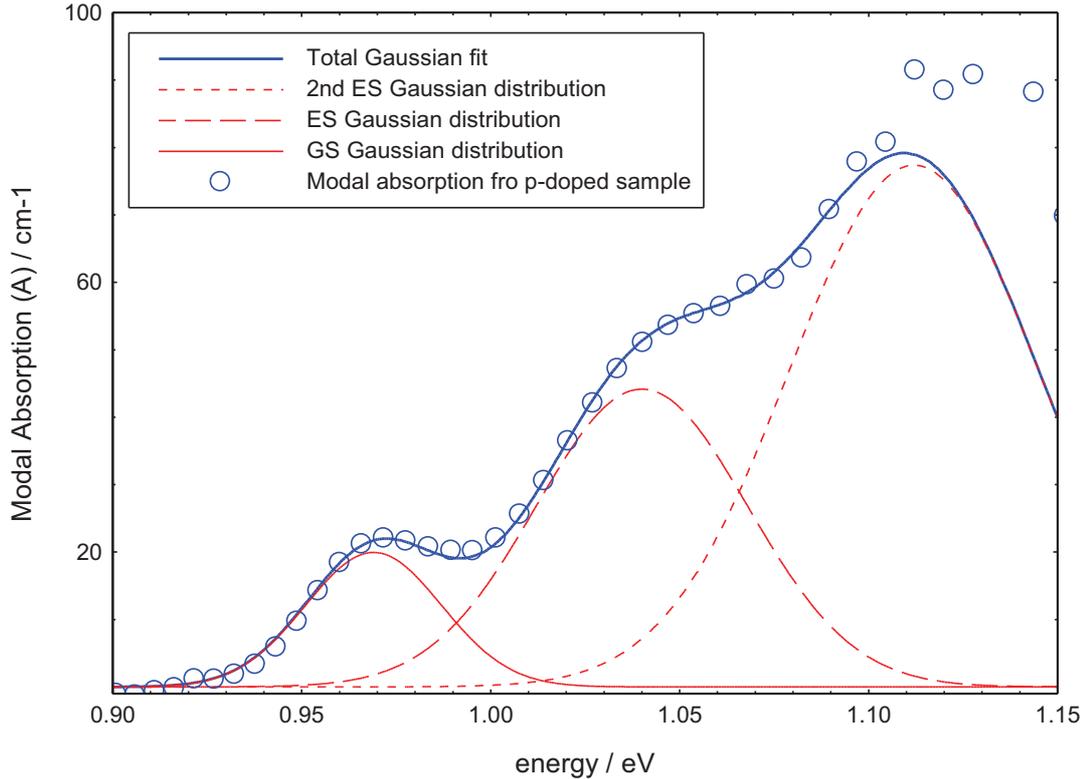
Figure 4.2. Modal absorption (circles) for p-doped sample and fitted monomodal Gaussian total (solid blue line) of GS (solid red line), ES (dashed Red line) and 2nd ES (dotted red line) distributions.

The good visual fit shown in Figure 4.2 was obtained using Gaussians centred on 0.969 eV for the GS, 1.041 eV for the ES and 1.116 eV for the second ES that are inhomogeneously broadened by 17 meV, 29 meV and 33 meV respectively. The area under the Gaussians is proportional to the number of states inhomogeneously broadened about the transition energy of the Gaussian. So by comparing the areas between the GS and two ES states it is possible to determine the degeneracy of the ESs. The ratio of the areas under the GS and first ES is 1:(3.9±0.2). This ratio suggest that the first ES has a fourfold degeneracy which is contrary to observations made where the transition strengths of the GS and ES is 1:2 due to a twofold degeneracy brought about by the size and shape of the quantum dots [Deppe, et al., 1999, Kim, et al., 2003, Osbourne, et al., 2004 and Park, et al., 1998]. Although fourfold degeneracy has been reported [Drexler, et al., 1994, Jiang and Singh, 1997, Pettersson, et al., 1999, Zhou, at al., 1999] in InAs quantum dots for both theoretical and experimental results, brought about by rotational symmetry and spin degeneracy in the ES, the degeneracy of the second ES gives reason to believe that this is not the

case in these QDs. The ratio of the areas under the GS and second excited state is 1:(8.2±0.3) and this degeneracy has no physical justification. A threefold degeneracy is predicted from a simple harmonic oscillator model of the energy states [Deppe, et al., 1999 and Park, et al., 1998]. The inhomogeneous broadening used to fit these Gaussians give further evidence that a monomodal fitting approach is not appropriate. A much greater broadening is required to fit the ESs than the GS and an increase of this magnitude has no physical reason. A monomodal modal fitting approach was also applied to the un-doped and n-doped sample modal absorption spectra and these yielded similarly improbable fitting parameters.

Having obtained strong evidence that these samples could not be monomodal, Gaussians assuming a bimodal dot size distribution were fitted. In order to fit the measured modal absorption spectra with a bimodal distribution of QD states that overlap extensively, six Gaussians representing the GS, ES and second ES of the large and small dot subsets were fitted and the total of these Gaussians compared with the modal absorption spectra. Figure 4.3 shows these six Gaussians fitted to a good agreement with the modal absorption of the p-doped sample.
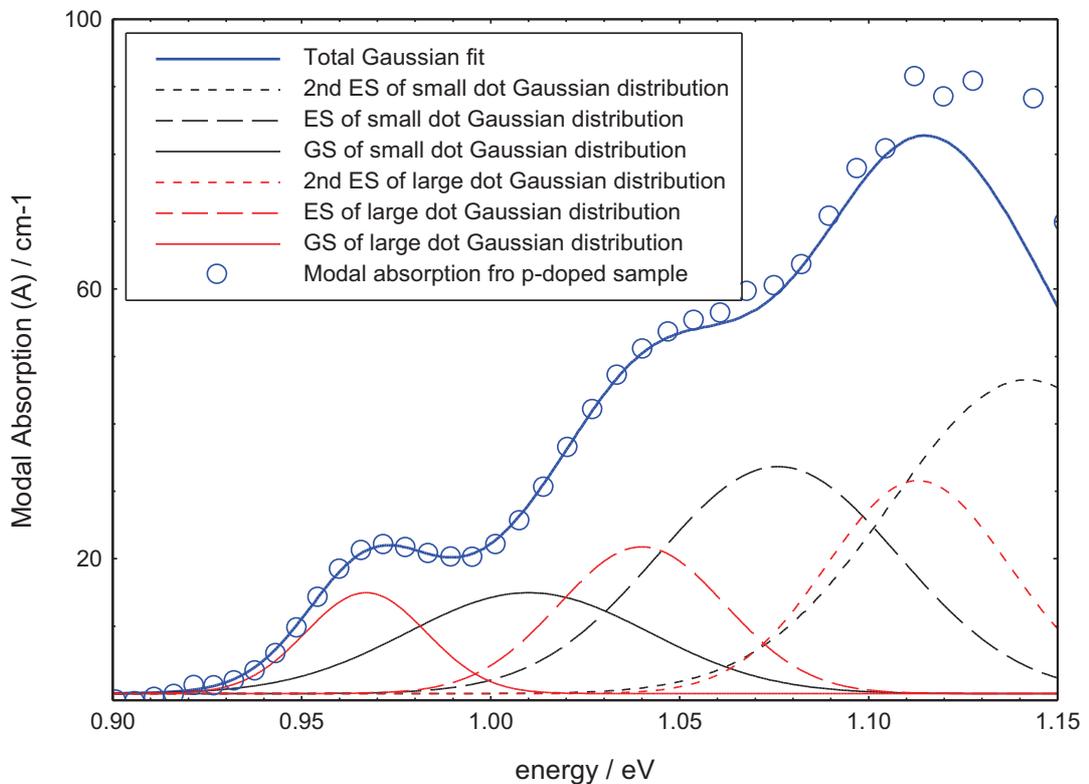

Figure 4.3. *Modal absorption (circles) for p-doped sample and fitted bimodal Gaussian total (solid blue line) of Large (red) and Small (black) dot distributions.*

The peak transition energies of and standard deviations of the Gaussians used to give the fit seen in Figure 4.3 are summarised in Table 4-1.

Table 4-1. Fitting parameters used for bimodal fit of p-doped sample (Figure 4.3)

	Peak Energy (eV)	Standard Deviation (meV)
Large Dot Subset		
Ground State	0.967	16
1st Excited State	1.04	22
2nd Excited State	1.113	24
Small Dot Subset		
Ground State	1.01	32
1st Excited State	1.076	33
2nd Excited State	1.142	36

Using this bimodal fitting approach gives GS to ES to second ES ratios of 1:(2±0.2):(3.15±0.30) for the large dot subset and 1:(2.25±0.20):(3.45±0.40) for the small dot subset. Both these ratios agree well with the 1:2:3 degeneracy's between the ground, excited and second excited states predicted by the simple harmonic oscillator model of energy states.

This fitting approach uses a large number of parameters so it is crucial to gain confidence in any fit. This confidence is obtained in a number of ways. Firstly the inhomogeneous broadenings between the ground and excited states of the two subsets are considered. In the monomodal fitting approach a significant increase in broadening was required to fit the ESs relative to the GS which had no physical justification. The broadenings used in the bimodal fitting approach, seen in Table 4-1, seem much more reasonable. There is only a small increase in the broadening used to fit the ES relative to the GS for the two subsets. The energy state distribution is narrower for the large dots subset than the small dot subset; this can be explained by the fact that a larger spread in energy is expected for a narrower, deeper potential well.

To gain further confidence the ratios between the GSs (and ESs) of the large and small dots were considered, this ratio gives the relative absorption strength of each dot subset and is related to the number of dots in each subset. The ratio between the

GSs and the two ESs should be the same as they have the same degeneracy. ratios of 1:(2±0.3), 1:(2.25±0.30), 1:(2.2±0.4), are obtained between the GSs, ESs and second ESs respectively. These ratios agree well within the tolerances of the fits and so It can concluded that the Gaussian fits do indeed represent those from two dot subsets where there are roughly twice as many small dots than large dots, assuming that their absorption (optical) cross section are the same.

This fitting process was also applied to the un-doped sample. Peak positions and ratios of GS to ESs similar to those obtained from the p-doped absorption fitting were observed. The ratios between the same states of the different dot subsets also showed there to be twice as many small dots as there are large dots. This confirms my previous conclusions that growth of the QDs is unaffected by the incorporation of p-type dopant and that the un and p-doped sample have the same electronic structure.

It was concluded from the measurement of the n-doped sample's absorption spectrum, shown in Figure 4.1, that the incorporation of n-dopant had affected the growth of the QDs, however this conclusion was based on the observed absorption being the true absorption and that all excess carriers had been successfully removed during measurement. To test the plausibility of the n-doped absorption spectrum, attempts to fit it with a bimodal state distribution were made to see if the ratios between the states were sensible. This would provide confidence in the measurement process. Figure 4.4 shows six Gaussians fitted to the n-doped samples modal absorption spectrum for best agreement.
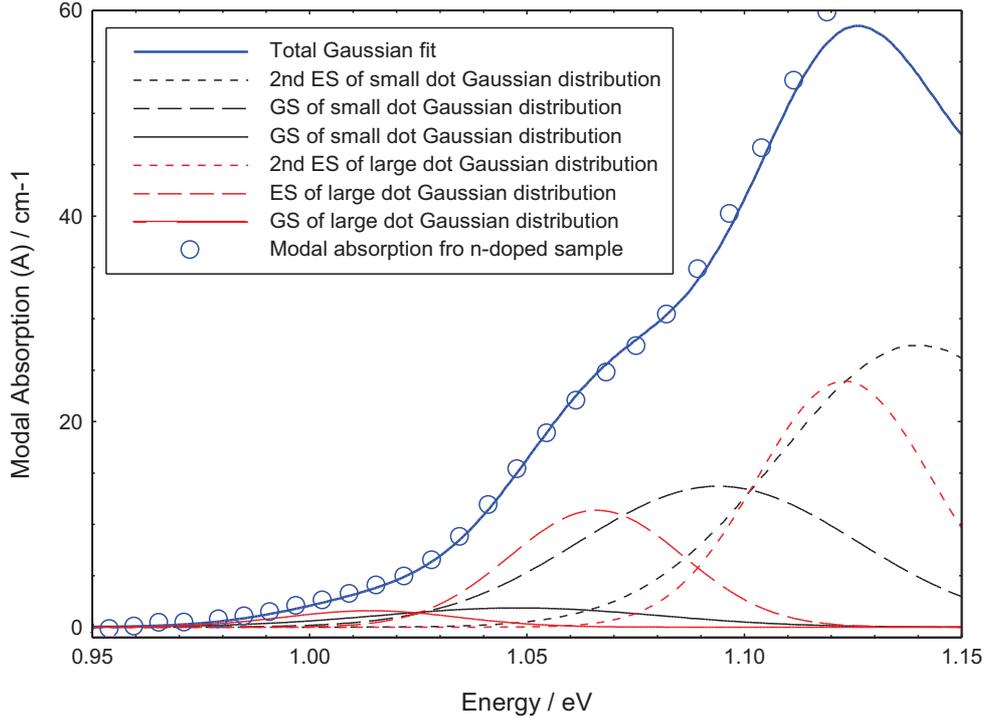
Figure 4.4. Modal absorption (circles) for n-doped sample and fitted bimodal Gaussian total (solid blue line) of Large (red) and Small (black) dot distributions.

The peak transition energies of and standard deviations of the Gaussians used to give the fit seen in Figure 4.4 are summarised in Table 4-2.

Table 4-2. Fitting parameters used for bimodal fit of n-doped sample (Figure 4.4)

	Peak Energy (eV)	Standard Deviation (meV)
Large Dot Subset		
Ground State	1.014	19
1st Excited State	1.066	20
2nd Excited State	1.123	20
Small Dot Subset		
Ground State	1.048	32
1st Excited State	1.097	32
2nd Excited State	1.14	33

The first thing to note from the fit in Figure 4.4 is that the GS peak transition energies for the large and small dots have been shifted to higher energy, 47 meV and 38 meV respectively, compared to the p-doped sample. This suggests that the n-

dopant has caused the QDs to decrease in size or alter in composition during growth and so form potentials with greater energy separation. The size difference between the large and small dot subset is less than in the p-doped sample as the energy difference between the peak GS distribution of each subset is roughly 10 meV smaller. Looking more closely at the Gaussians in Figure 4.4, you can see immediately that the relative absorption strength of the GSs of each subset is significantly less than that of the ESs. This is reflected in the ratios of GS to ES to second ES which are 1:(7.1±0.4):(15.0±0.6) and 1:(7.3±0.4):(14.7±0.6) for the large and small dot subsets respectively. These degeneracies are far too large to have any physical meaning and so it is concluded that the measured absorption spectrum for the n-doped sample does not represent the true absorption of the material. In this sample it is apparent that not all carriers are removed from the highly populated zero dimensional QD electronic conduction band states under zero injection, due to the n-dopant. The level of reverse bias required to remove these carriers is significantly greater, as these electron states are deep compared to the hole states (where carriers are relatively easily removed in the p-doped sample) and so this level is above the breakdown voltage of the band structure. Evidence that a Pauli blocking effect from excess carriers is leading to a failure to measure the true absorption and it is not simply that the QD states are no longer there comes from considering the lack of absorption strengths from the GSs of the subsets. The ES degeneracy's seem reasonable when compared without considering the GS. This leads to the conclusion that the GS absorption is being suppressed to a higher extent than the ESs which would be expected if due to Pauli blocking as the deeper GSs would be the hardest to remove carriers from. More evidence that QD states still exist in the n-doped sample comes from considering the ratios between the ESs of the large and small dots. The fit in Figure 4.4 yields ratios of 1:(1.9±0.3), 1:(1.8±0.4) between the ES and Second ES respectively. Both these ratios agree with those found for the p-doped sample and this would be expected as the materials have identical growth conditions apart from the doping.

The nature of the measured absorption spectrum for each sample suggests that the inclusion of n-dopant within the growth has possible affected the QD states however the full extent of this cannot be determined due to the difficulties in the measurement. Although this means that direct comparisons between the samples

will be qualitative it is still relevant to make these comparisons as it is important to fully characterise the effect that incorporating modulation doping has on InAs QDs and determine any advantages or disadvantages that this could lead to for any particular application.

4.3.2. Modal Gain at 300 K.

Net modal gain spectra were measured for the three samples for various levels of injection between 25 K and 400 K using the method outlined in section 3.2.3 of chapter 3. All Gain measurements shown in this section are for TE polarised light. Net modal gain spectra measured for the un-doped sample at 300 K are shown in Figure 4.5.
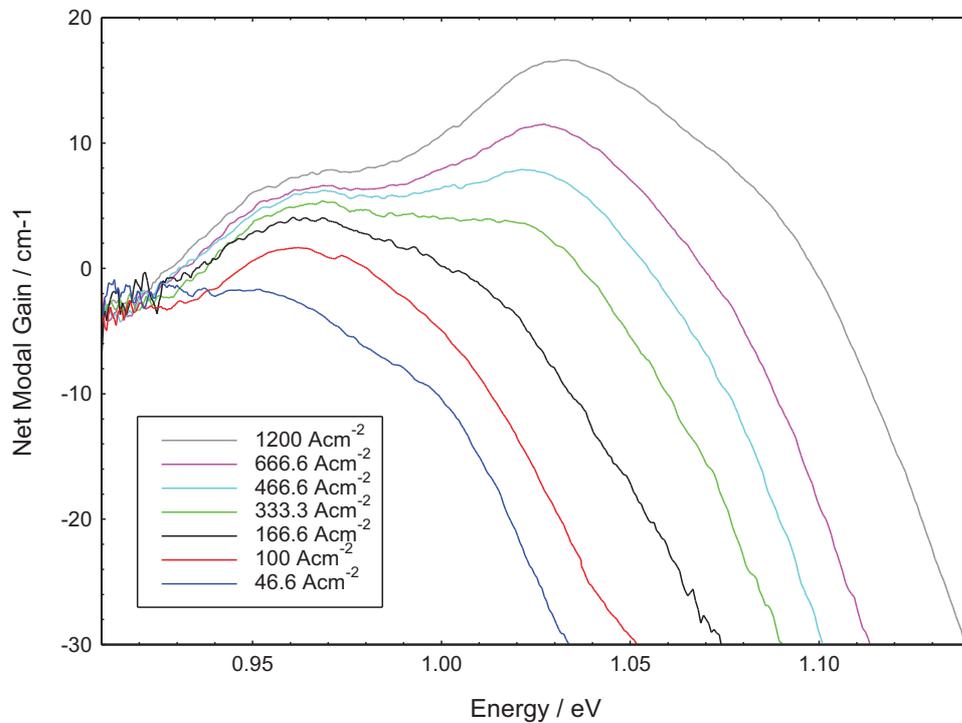
Figure 4.5. Net modal gain spectra for un-doped sample measured at 300 K for injections of 46.6, 100, 166.6, 333.3, 466.6, 666.6 and 1200 Acm^{-2}.

All spectra in Figure 4.5 converge, as expected, at low energies giving an α_i value of 2 ± 2 cm^{-1} which is consistent with previous measurements, where the value of α_i was inferred from external differential efficiency measurements performed on devices of different length [Shchekin et al., 2002]. For this sample, gain is exhibited from both the ground and excited states with two clear peaks centred on 0.96 eV and 1.03 eV, these peaks correspond to lasing wavelengths of 1.3 µm and 1.21 µm. A

blue shift to higher energies of both the gain peaks is observed for increasing injection as the states become filled with carriers. The highest peak gain switches from the GS to the ES at a current density of around 300 Acm^{-2} and this would result in a lasing wavelength shift of 1.3 μm to 1.21 μm. This would be detrimental for its application in telecommunication where a lasing wavelength of 1.3 μm is required to match the transparency window for silica optical fibres.

Net modal gain spectra measured for the n-doped sample at 300 K for various levels of injection are shown with its absorption spectrum measured at 300 K in Figure 4.6.
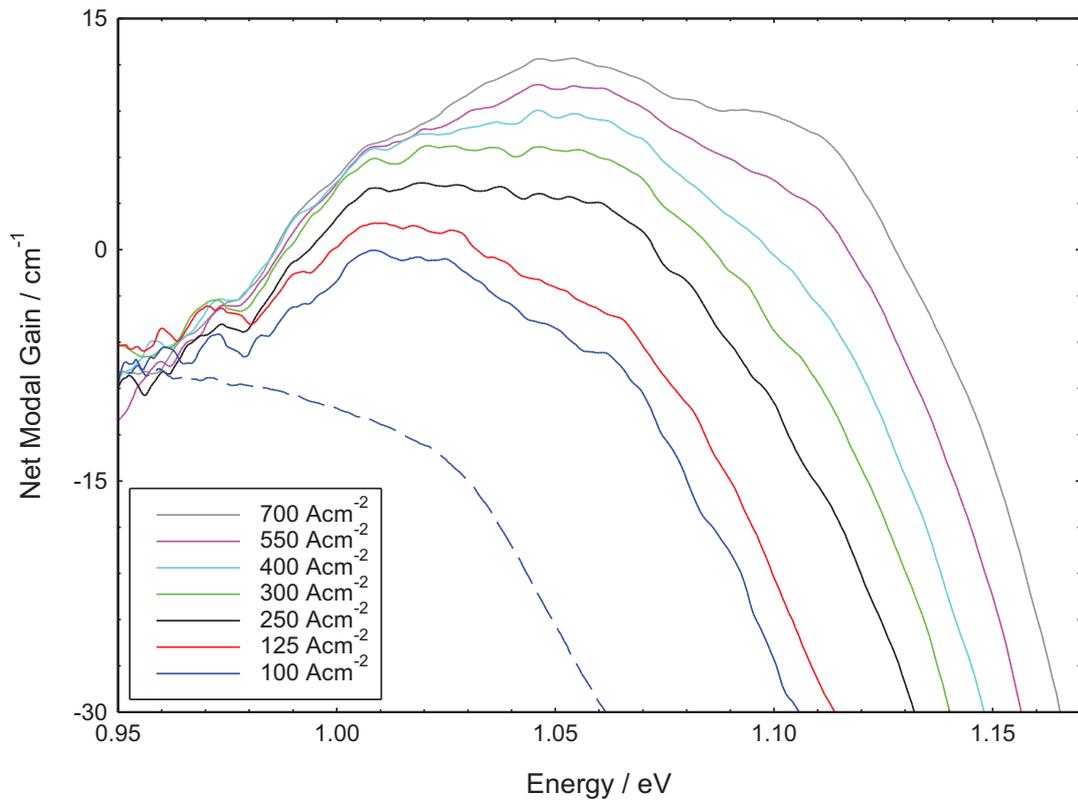
Figure 4.6. Net modal gain spectra for n-doped sample measured at 300 K for injections of 100, 125, 250, 300, 400, 550 and 700 Acm^{-2}.

Several interesting observations can be made from the spectra shown in Figure 4.6. Like the previous sample, all spectra converge at low energies, but this sample has an α_i value of 7 ± 2 cm^{-1} which is significantly higher than that of the un-doped sample. This suggests that the n-dopant has increased free carrier absorption or created defect states within the material. It is only possible to differentiate between the gain from the ground and excited states at very low injection where gain is only experienced by the GS. This suggests that the there is significant overlap of the states in the sample

due to large inhomogeneous and homogeneous broadening. The low injection gain peak is centred on 1.01 eV with this shifting to 1.05 eV at the highest injection levels. This would correspond to a lasing wavelength of 1.23 µm shifting to 1.18 µm. The measured absorption spectrum for the n-doped sample has been included in Figure 4.6 to illustrate that it cannot possibly be the true absorption for this sample. At the GS energy of 1.01 eV the modal absorption is measured to be 4 cm^{-1} however, at this energy, gains as high as 14cm^{-1} are measured. Even though broadening allows for states at these energies to interact with higher energy states where the absorption is greater, this 10 cm^{-1} discrepancy seems extremely unlikely.

In characterising a laser material an important consideration is the threshold current. This can be predicted from measurement of net gain spectra by considering how these spectra evolve with injection. Net gain versus current density graphs can be constructed by plotting the peak net modal gain at a function of drive current. In the case where there are two clear peaks in the gain spectra, from the GS and ES (un and p-doped sample), both peaks are plotted individually. Figure 4.7 shows this analysis applied to the measurements of net modal gain made on all three samples at 300 K. The error bars in Figure 4.7 are calculated separately for each axis. The current density axis (x-axis) errors were calculated by applying an error in the nearfield and section length measurement when converting injection currents to current densities (this error is dominant over errors associated with reading the currents). An error of ± 5 % was established from measurement of the sample nearfields, due to noise in the signal, and an error of ± 1 % is associated with slight differences in the length of the sections, caused by small uncertainties in the placement of the scribe whilst cleaving the front facet. The error in peak net modal gain (y-axis) is calculated from noise on the ASE by considering the rolling average of each ASE energy increment. This allows for the energy dependence of the error value to be determined.
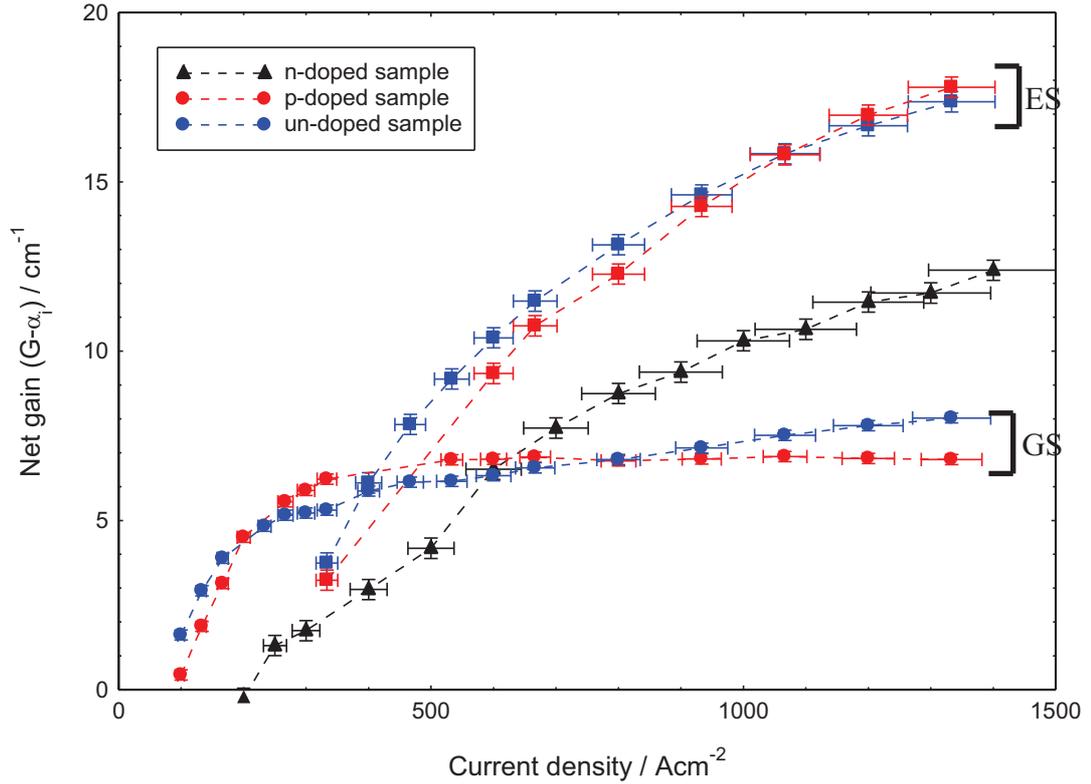
Figure 4.7. Net modal gain as a function of drive current density for the un-doped (blue) and p-doped (red) sample's GS (circles) and ES (Squares) peaks and the n-doped (Black triangles) sample's single peak measured at 300 K.

A number of interesting conclusions can be inferred from Figure 4.7. The most obvious conclusion is that the n-doped sample has significantly poorer peak net gain performance compared to the other two samples, i.e the peak net gain is always less than that achieved in the un and p-doped samples. This is directly down to the significant increase in α_i measured in this sample over the others, if the n-doped sample had the same α_i as these samples then it would show superior threshold gain performance. Although it is important to remember that this sample would lase at 1.18 μm which is not valid to the application for which they are designed. Considering the behaviour of the un-doped and p-doped samples, at first glance they seem similar but the subtle differences will result in notable lasing performance variances. The main similarity is that both samples show a strong saturation of the GS gain for increasing injection; this is expected due to the finite number of available QD states. Above (200 ± 15) Acm^{-2} a higher net gain is achieved in the p-doped sample until the ES of the un-doped sample begins to dominate at (400 ± 30) Acm^{-2}. The p-doped sample does not begin to operate on the ES until (485 ± 36) Acm^{-2}. From this it can concluded that above 200 Acm^{-2} the p-doped sample would

lase with a lower threshold current density and 1.3 μm lasing would be maintained to a greater current density compared to the un-doped sample. These differences in net gain versus current density characteristics become particularly prominent when you consider the performance of particular length laser devices. The threshold gain requirement can be determined for a particular length laser from equation 2.1 in chapter 2. From this it can be shown that a 2mm laser requires a net gain of 6cm^{-1} in order to lase and so the current density required to achieve this level of gain can be determined from Figure 4.7. The p-doped sample would have the lowest threshold current density of the three samples, at (307 ± 23) Acm^{-2}, with the un-doped sample having a threshold of (400 ± 30) Acm^{-2} and the n-doped sample having the highest threshold at (579 ± 43) Acm^{-2}. More importantly however is that for a 2 mm device length only the p-doped sample would operate with a lasing wavelength of 1.3 μm.

4.3.3. Modal gain as a function of temperature.

The behaviour of the net gain versus current density characteristics were studied between 25 K and 400 K for all three samples. Figure 4.8 and Figure 4.9 shows the data for the un-doped samples GS peak and ES peak respectively.
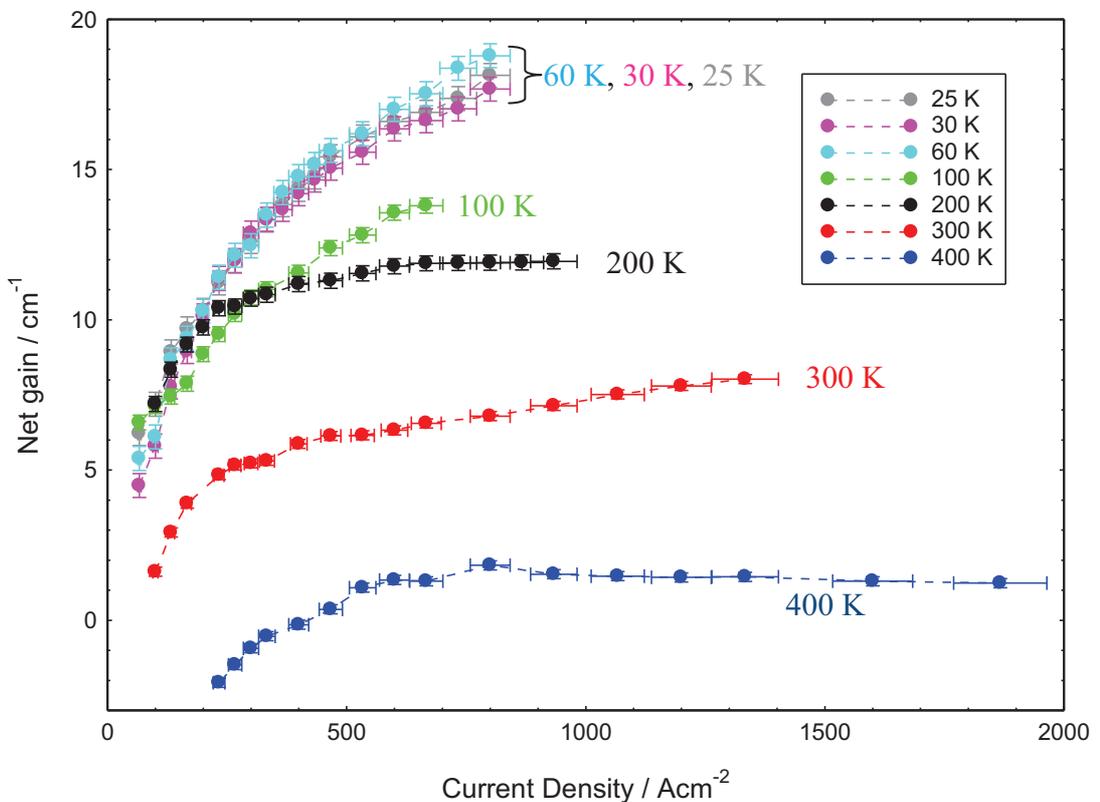

Figure 4.8. Un-doped sample's GS peak net modal gain measured between 25 K and 400 K.

Un-doped sample – Ground state.

Figure 4.8 shows that the level at which the gain peak saturates increases for decreasing temperature from 400 K down to 200 K. This behaviour is consistent with the QD states being in thermal equilibrium with the wetting layer and not becoming fully occupied before the wetting layer states become filled [Matthews, et al., 2002]. As the temperature of the sample is reduced the Fermi function becomes sharper and so the effect of the wetting layer states is reduced thus increasing the occupancy of the QD states. At 100 K, the gain current curve shows subtly different behaviour to that at 200 K. For low injection levels, below 300 Acm^{-2}, the gain achieved at 100 K is lower than that achieved at 200 K for the same injection level, then above 300 Acm^{-2} the gain at 100 K is always greater than that at 200 K. This is evidence that at 100 K the rate at which carriers thermally escape from the dots to the wetting layer is significantly reduced compared to that at 200 K and so these dot states are beginning to become decoupled from the wetting layer. This means that the dot states are no longer filled according to Fermi-Dirac statistics and so for any given level of injection a greater spread of states are occupied and gain is spread across more states. So at low injection levels less peak gain is achieved compared to at higher temperatures where dots are populated according to Fermi-Dirac statistics, then when saturation of the peak gain occurs at the higher temperature the gain at 100 K increases above that at 200 K.

At 60 K and below the gain no longer increases for decreasing temperature and appears to saturate, for increasing current density, at a value of (18 ± 0.5) cm^{-1} for the maximum injection level. This behaviour suggest that at 60 K and below the QD states are fully decoupled from the wetting layer states so carriers can no longer be thermally excited to these states thus maximum occupancy on the QD states can be achieved. This decoupling of the wetting layer states means that the available QD states are not occupied according to Fermi-Dirac statistics [O'Driscoll, et al., 2010] and in fact are occupied independently of energy. This process of occupation does not fully explain the observed behaviour however, if the states were populated independently of energy then you would expect the gain to saturate at a magnitude equal to that of the absorption at that energy, as this corresponds to a valence occupancy of 1 and a conduction occupancy of 0 and so is equal to the maximum gain available by completely inverting the population of the QD states. The

magnitude of the absorption, measured at 25 K, at this energy is (24.0 ± 0.5) cm^{-1} and so clearly not all the available GSs have been occupied. The gain and absorption spectra are related to each other through the occupancy factors of the electron and hole states when the sample is pumped. Between two QD states, E_2 and E_1, this relationship is of the form in Equation 4.1 assuming that the occupancy of the two states can be described by probability of occupancy factors, f_c and f_v.

$$G(E_2 - E_1) = A(E_2 - E_1)[f_c(E_2) - f_v(E_1)]$$

Equation 4.1

The transition energy (hv) is given by the separation of the states ($E_2 - E_1$) when effects that depend on carrier density, namely band gap narrowing, are negligible. Equation 4.1 can be used to determine the level of population inversion, (f_c - f_v), at the GS peak energy. Homogeneous broadening allows an overlap of optical transitions meaning that it is possible for light at specific photon energy to originate from transitions between states with a spread of occupation probabilities, not just the occupation corresponding to the photon energy itself and so Equation 4.1 may not be completely valid; however this approach is still useful for quantitative analysis. This approach also assumes that there are no many body interactions occurring. To account for the shift in the gain peak energy due to state filling the magnitudes of the gain and absorption peaks are used in Equation 4.1 as opposed to the gain and absorption magnitudes for a given energy separation. For the un-doped sample at 25 K, the degree of population inversion (f_c - f_v) at the GS peak energy is (0.75 ± 0.04). So the GS is not fully inverted.

Un-doped sample - Excited state.

More evidence that the occupation of the dot states is not simply described by a random capture process can be obtained by considering the net gain versus current density characteristics of the ES. The peak ES net gain is plotted against current density for the un-doped sample between 25 K and 400 K in Figure 4.9.
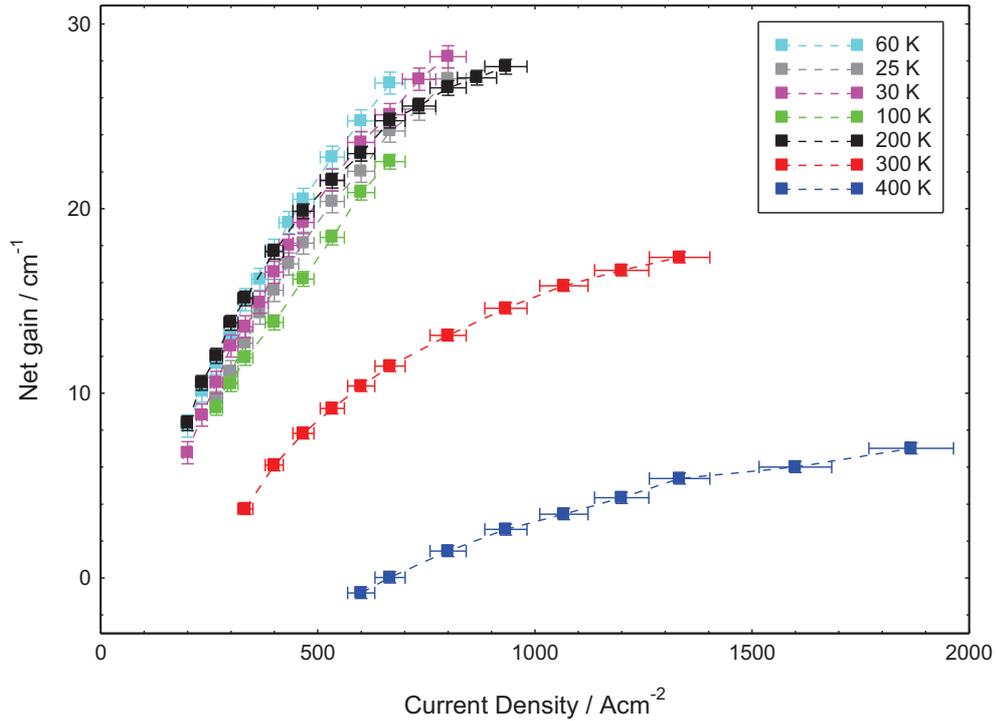
Figure 4.9. Un-doped sample's ES peak net modal gain measured between 25 K and 400 K.

Figure 4.9 shows that the peak ES net gain versus current density has the same behaviour with decreasing temperature as that of the GS above 200 K. However at 200 K and below the behaviour appears to be significantly more complex than that seen for the GS. At first glance the plots in Figure 4.9 suggest that the gain no longer increases for decreasing temperature at 200 K and below. However this would contradict the conclusions drawn from Figure 4.8 that this behaviour occurs due to the decoupling of the QD and wetting layer as if this was the case then the deeper GSs would decouple at a higher temperature than the ESs. In order to understand these observations, the low temperature data for both the GS and ES must be studied more closely.
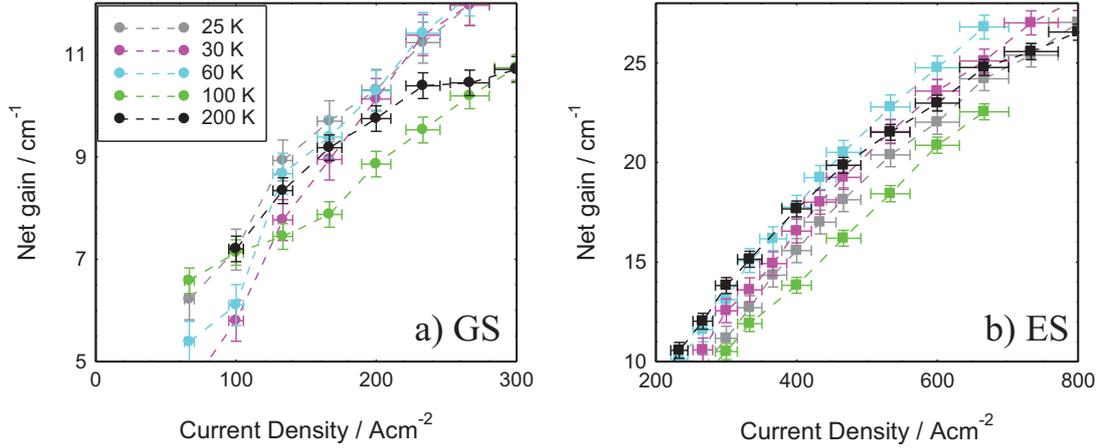
***Figure 4.10. a) Un-doped sample's GS peak net modal gain measured between 25 K and 200 K. b) un-doped sample's ES peak net modal gain measured between 25 K and 200 K.***

Figure 4.10 shows just the 200 K and lower data from Figure 4.8 and Figure 4.9 plotted so that clearer observations can be made. The GS data is plotted in the low injection, i.e. low occupancy level, region. Figure 4.10 shows that the ES data has very similar behaviour to the GS data. In both plots the 200 K, 60 K, 30 K and 25 K temperature data points are indistinguishable within the errors of the experiment. Also the 100 K data shows a similar linear relationship for increasing injection with the gain level lower than that achieved at 200 K for the same injection. Therefore, it is concluded that the injection level used in the experiment is not sufficient to saturate the ESs and in fact only a very low occupancy is achieved. This invalidates the "first glance" observations made from Figure 4.9 as the observations seen in Figure 4.8 occur at high occupancy where the GS gain is saturated.

In order to compare the behaviour of the GS and ES it is possible to fit a function to the ES gain versus current density data using an empirical equation of the form of Equation 4.2 [Ustinov, 2003] to extrapolate to higher injection levels.

$$G = G_\infty \left\{ 1 - \exp\left[\frac{-\gamma(J - J_{tr})}{J_{tr}} \right] \right\}$$

Equation 4.2

where G_∞ is the maximum gain achieved as the current density tends to infinity, J_{tr} is the transparency current density and γ is a dimensionless non-ideality parameter. Equation 4.2 has been fitted to the ES data measured at 200 K and below. At 200 K

the best fit was achieved with a G_∞ of (31.1 ± 0.3) cm^{-1} whilst at 25 K G_∞ was found to be (37.8 ± 1.3) cm^{-1} showing that at 200 K the maximum ES occupancy has not yet been achieved. The G_∞ obtained from fitting 60 K and 30 K where (39.4 ± 0.9) cm^{-1} and (40.1 ± 1.1) cm^{-1} respectively, so below 60 K the gain no longer increases for decreasing temperature, which agrees with the observations made from the GS peak gain. These extrapolated G_∞ can be used to estimate the maximum occupancy of the ES at 25 K using Equation 4.1 and compare this with the occupancy of the GS at this temperature. The magnitude of the absorption at the ES peak energy at this temperature is (62.3 ± 0.5) cm^{-1} which means that the degree of population inversion of the ES is (0.61 ± 0.02). If the dot states were occupied simply by a random capture process then you would expect the GS and ES to have the same occupation probability and so be inverted to the same degree, however in this sample the ES is less inverted than the GS at 25 K. It is possible that while carrier capture into the dot states is random there may be trickle down between the ES and GS causing the lower states to become more inverted. More complex analysis techniques will be implemented on these samples in the subsequent chapters of this thesis to obtain a complete picture of carrier occupation in QDs and explain the observations seen in these gain spectra.

p-doped sample – Ground state.

The net modal gain versus current density characteristics were also studied for the p-doped sample between 25 K and 400 K and Figure 4.11 shows this plotted for this samples peak GS net gain.
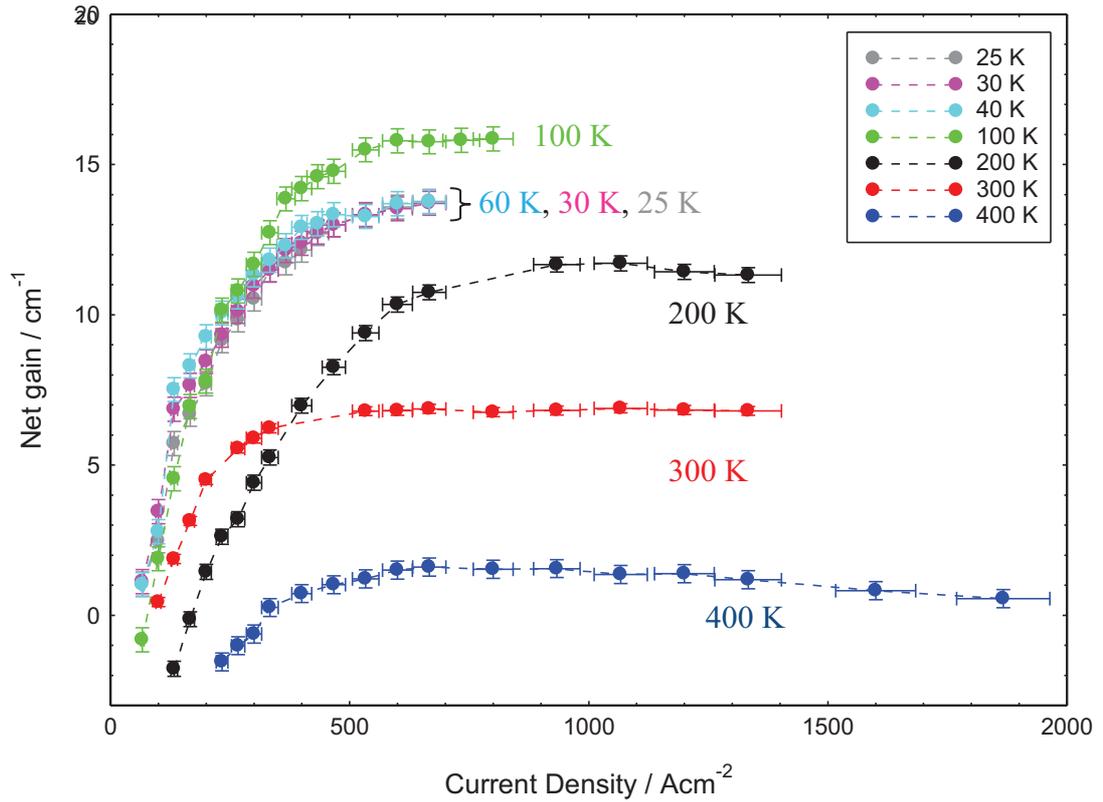
Figure 4.11. p-doped sample's GS peak net modal gain measured between 25 K and 400 K.

The p-doped sample shows similar gain versus current density behaviour as the un-doped sample with decreasing temperature however there are differences observed that suggest this sample performs differently under these conditions. The peak gain saturation increases in the expected fashion as the temperature decreases to 100 K however, at 200 K the gain at any injection level below (371 ± 19) Acm^{-2} is less than that at 300 K, then above this injection level the gain saturates at 300 K whilst the 200 K gain data continues to increase up to saturation at (11.50 ± 0.25) cm^{-1}. This is the same behaviour as that observed in the un-doped sample but in that sample it occurred between 100 K and 200 K. So like in the un-doped sample this is evidence that the wetting layer states are becoming decoupled from the QD states and so population is non-thermal, but now this is happening in the p-doped sample at the higher temperature of 200 K. The transition from thermal to non-thermal population occurring at higher temperatures for p-doped samples compared to un-doped samples has been reported previously [Smowton, et al., 2007] where in similar structures a minimum in laser threshold current was observed at 200 K and 270 K for an un and p-doped structure respectively, this being attributed to a transition to non-thermal population behaviour below those temperatures. The peak gain for the p-doped

sample at 100 K is always greater than that at 200 K as expected and saturation occurs at a value of (15.8 ± 0.4) cm^{-1} however, at 40 K whilst the gain level at low injection is roughly matched to that at 100 K the gain peak saturates at the lower value of (13.7 ± 0.4) cm^{-1}. Below 40 K the gain versus current density plots are identical. In the un-doped sample the similar gain saturation values below 60 K was evidence that maximum occupancy of the GS was achieved and that these states are fully decoupled from the wetting layer states at 60 K and below. In this p-doped sample the higher gain saturation, and thus higher maximum occupancy, at 100 K compared to 40 K suggests that the population of these dot states is complex and cannot simply be evidence for a transition from non-thermal to random population.

To explain this result the radiative recombination for a fixed level of gain at these two temperatures must be considered at the energy of the peak gain used to construct Figure 4.11. As the population becomes non-thermal, more higher lying energy states become filled for any given injection, this increases the width of the spontaneous emission spectrum and so increases the total radiative rate, however for a low energy GS transition the intensity of the spontaneous emission will not increase as the state becomes non-thermally occupied. The spontaneous emission obtained for a fixed gain of 12 cm^{-1} at 100 K and 40 K is shown in Figure 4.12. The y-axis error bars are calculated in a similar manor to those for Figure 4.7.
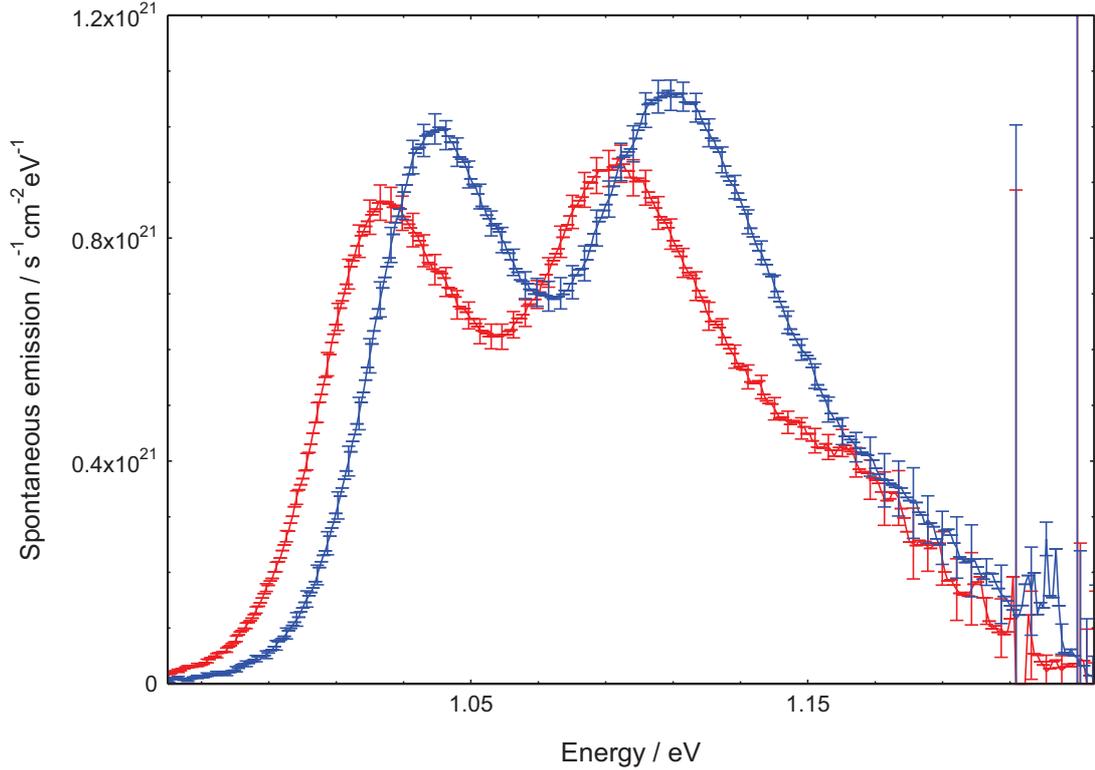
Figure 4.12. *Spontaneous emission spectra plotted against photon energy for p-doped sample measured at 100 K (red) and 40 K (Blue) for a fixed injection of 12 cm^{-1}.*

Between 100 K and 40 K the GS absorption spectrum shifts by 16 meV and this is reflected in the spectrum shown in Figure 4.12. A striking observation from Figure 4.12 is that the intensity of the spontaneous emission at the peak GS energy is greater at 40 K than at 100 K. This is an unexpected result as the spontaneous emission is plotted for fixed G and so this means that for the same inversion level ($f_2 - f_1$) the radiative recombination ($\sim f_2(1-f_1)$) is greater. In this p-doped sample the hole states are filled to a greater extent than in the un-doped sample meaning that f_1 is small. At a gain of 12 cm^{-1} the occupation level is roughly 0.5 so for small f_1 values $f_2(1-f_1)$ will also be close to 0.5. If f_1 (and f_2 by the same amount) is increased then $f_2(1-f_1)$ can increase up to 10 %. In Figure 4.12 a (8.0 ± 0.5) % increase in spontaneous emission, at the peak GS energy, is observed as the temperature is reduced from 100 K to 40 K. So from this it is concluded that the number of holes in the GS has reduced between these temperatures. The ionisation energy of Be acceptors in AlGaAs has been reported as a function of Al concentration in [Galbiati, et al., 1997]. For 0 % Al (i.e. GaAs) the ionisation energy was found to be (27.5 ± 0.7) meV using a similar level of doping as used in the p-doped structure studied

here. For acceptors to populate the hole states of the p-doped samples they must first ionise to the GaAs states of the structure. At room temperature kT is 25 meV and so acceptors are easily ionised in the p-doped structure, as the temperature is reduced so is kT and thus the Be is harder to ionise. The increase in radiative recombination of the GSs for a fixed gain observed between 100 K and 40 K is evidence that fewer Be atoms are ionised at 40 K compared to 100 K, where kT has reduced by a third, and so f_1 is greater at 40 K than 100 K. This also explains why the gain saturates at the lower level of (13.7 ± 0.4) cm^{-1} at 40 K. It is also interesting to note that the maximum population inversion of the GS at 40 K in this p-doped sample is (0.57 ± 0.03) which is lower than that for un-doped sample. Although some interesting insight has been discussed using these gain versus current density observations, definitive conclusions cannot be drawn using them alone. The ES data for this p-doped sample has not been shown here as the same behaviour, with decreasing temperature, as the GS is observed.

n-doped sample.

The peak net modal gain versus current density characteristics were measured for the n-doped sample as a function of temperature. In Figure 4.6 a significant overlap of the ground and ESs was observed for the n-doped sample and so only single gain peak can be measured. The is peak net modal gain is plotted versus current density between 25 K and 350 K for the n-doped sample in Figure 4.13.
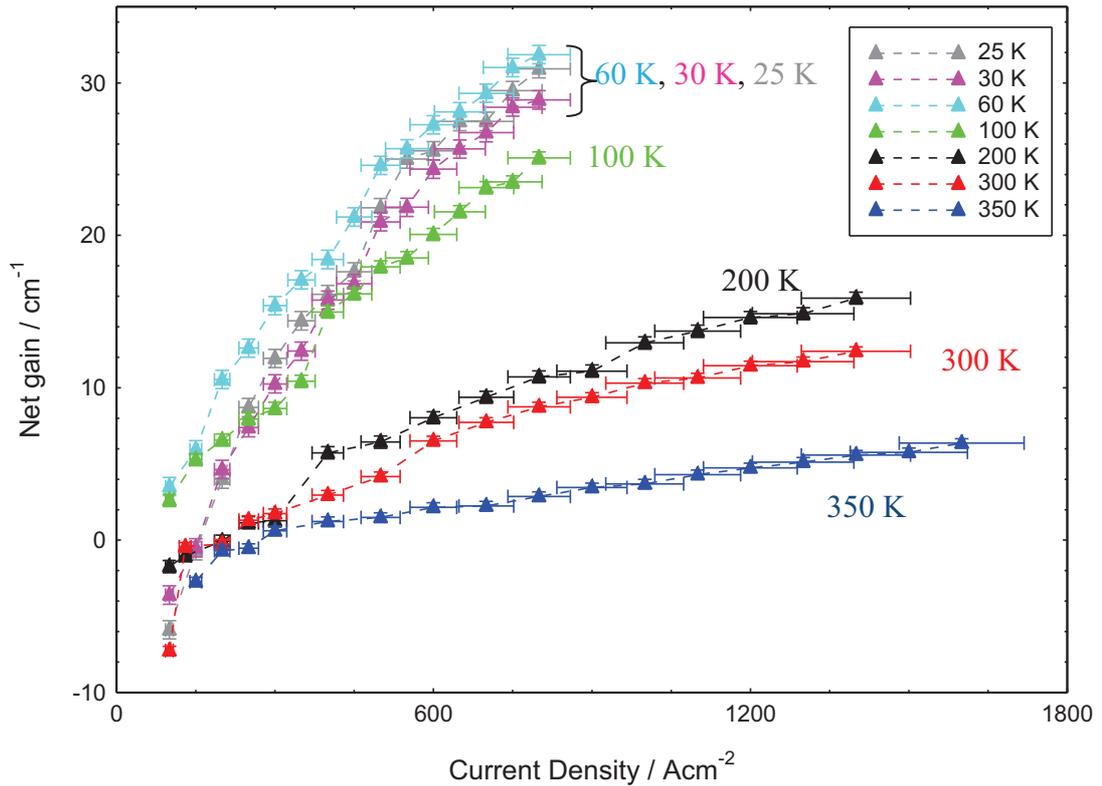
Figure 4.13. n-doped samples peak net modal gain measured between 25 K and 350K.

In Figure 4.13 we observe the expected trend in the gain versus current density with decreasing temperature down to 60 K. At 30 K and 25 K the gain is the same at any given injection and is less than that at 60 K for low injection which is evidence, as with the other two samples, for a decoupling of the wetting layer and QD states. The peak gain values are similar at any given injection above roughly 16 cm^{-1} at 60 K and below, however peak gain saturation has not been achieved and so decisive conclusions can be drawn from this data alone.

4.3.4. Radiative and total current densities.

The spontaneous emission was measured in real units for all samples by applying the calculations described in section 3.2.4 of chapter 3 to the segmented contact measurements. The spontaneous emission measured at 300 K for TE polarised light is shown in Figure 4.14 for the three samples at the same current density.
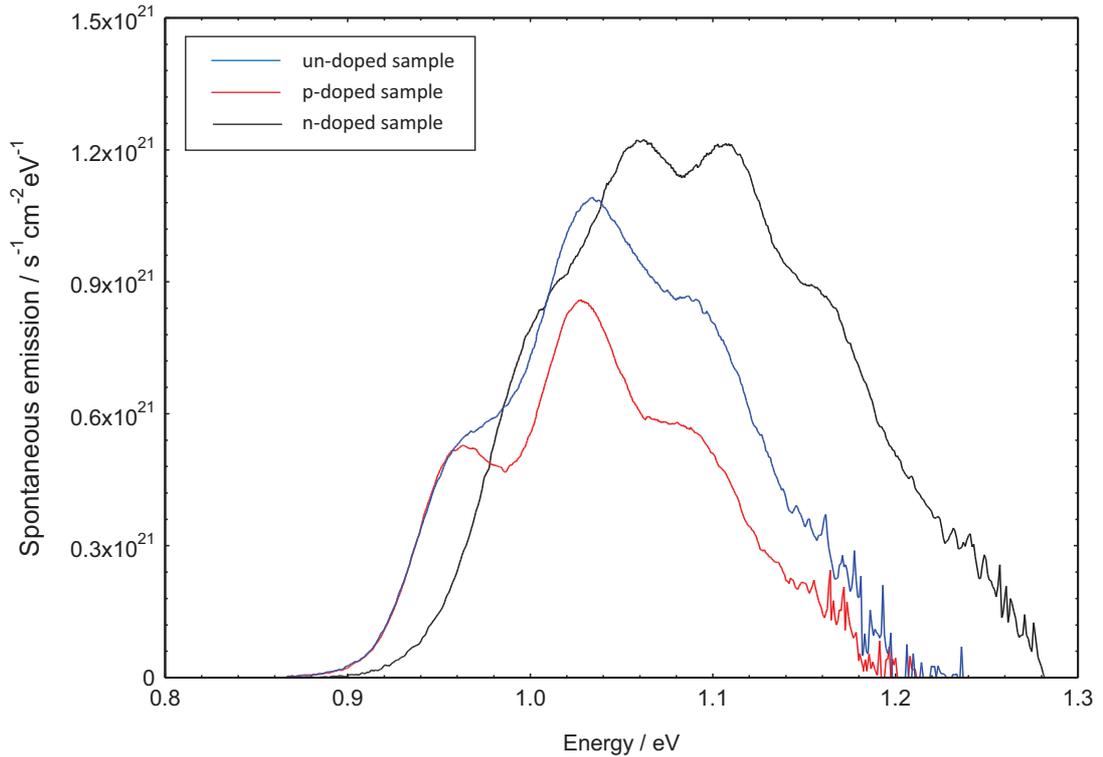
Figure 4.14. *Spontaneous emission spectra plotted against photon energy for the un-doped (blue), p-doped (red) and n-doped (black) samples measured at 300 K for the same current density.*

From Figure 4.14 it is clear that, for the same current density, the total spontaneous emission from the n-doped sample is greater than both the other sample's, as its spectrum is significantly broader and higher in intensity at all energies (accounting for the state shifts to higher energy seen in the n-doped sample from the altered dot growth from the doping). This means that this sample has the largest radiative efficiency of all three samples at this current density. One might expect this to be a positive characteristic. However, it is important to remember that only the radiative emission for a limited energy range contributes towards lasing in a device and so all emission outside of this is detrimental to its performance. The n-doped sample has a broader spectrum as there appears to be a significant level of emission from the excited states of this sample. So much so that a fourth emission peak is present in the n-doped sample compared to the three peaks observed in the other samples. It is also interesting to note that the GS peak emission in the un and p-doped sample is roughly the same intensity and this corresponds to lasing of the desired wavelength of 1.3 μm. To characterise the radiative and non-radiative emission in these samples the radiative current density (calculated by integrating the spontaneous emission)

versus total current density is plotted. This is shown for the three samples at 300 K in Figure 4.15. The errors for this plot are calculated in a similar fashion to those in Figure 4.7.
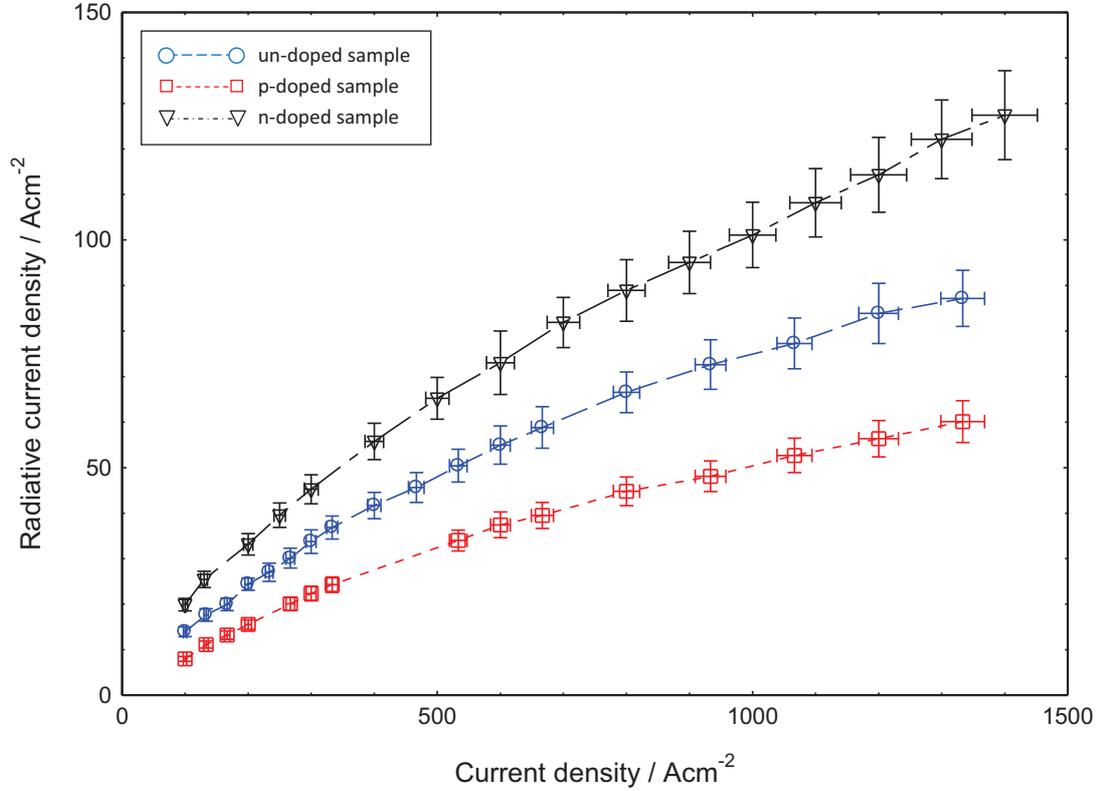
Figure 4.15. Radiative current density versus current density for the un-doped (blue circles), p-doped (red squares) and n-doped (black triangles) samples at 300 K

This plot shows that the observations made in Figure 4.14 are true at all current densities. Using the plots in this figure along with the gain versus current density data shown in Figure 4.7 it is possible to calculate the radiative and total threshold current density corresponding to particular length lasers at 300 K. Using the laser threshold roundtrip conditions shown in section 2.2.1 of chapter 2 we obtain an equation for the net gain (G_{th}-α_i) required to overcome the losses in a cavity. This equation is repeated here in Equation 4.3.

$$(G_{th} - \alpha_i) = \frac{1}{L} \ln\left(\frac{1}{R}\right)$$

Equation 4.3

where L is the length of the laser cavity and R is the reflectivity of the facets (assuming they are equal). Using this equation it can be shown that a net gain value

of 6 cm^{-1} is the threshold requirements of a 2 mm long laser. So the threshold current of these length lasers can be determined for each sample. Using Figure 4.7 the radiative current density at this threshold can be determined from Figure 4.15. This process can be used to calculate the threshold and radiative current densities over the entire measured temperature range for the three samples. The radiative current density versus temperature is shown for all three samples at a net gain of 6 cm^{-1} in Figure 4.16 (a). The total threshold current density versus temperature is shown for all three samples at a net gain of 6 cm^{-1} in Figure 4.16 (b).
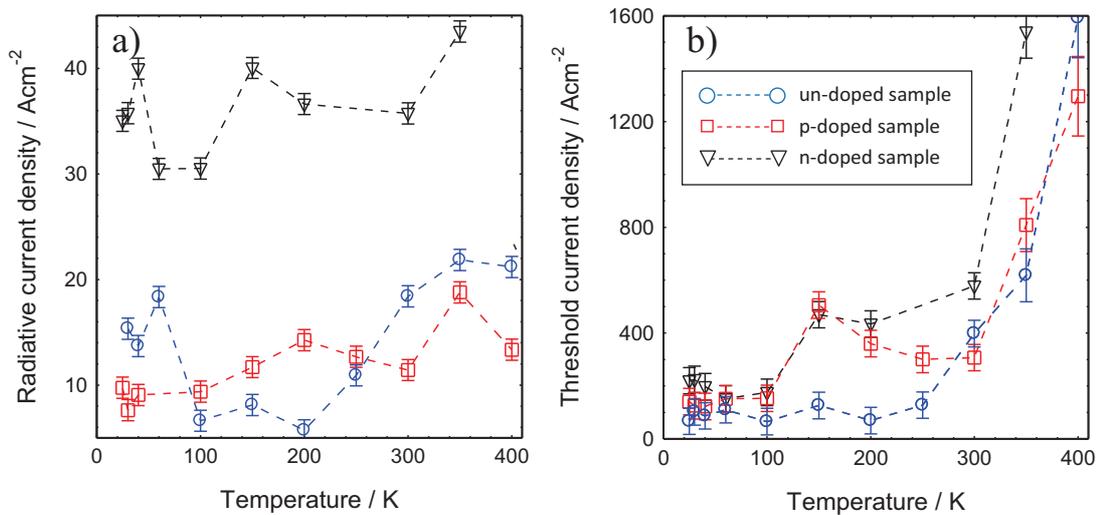
Figure 4.16. a) Radiative current density versus temperature and b) Total current density versus Temperature for the un-doped (blue circles), p-doped (red squares) and n-doped (black triangles) samples at a fixed net gain of 6 cm^{-1} (2 mm laser).

The un-doped sample's radiative current density increases from 200 K to 350 K and then does not increase up to 400 K. The behaviour of this sample above 350 K is unusual as you would expect an increase in the thermal spread of carriers leading to greater radiative recombination from the higher lying states. The p-doped sample shows weaker temperature dependence than the un-doped sample however above 300 K there is an increase in the radiative current density up to 350 K and then is seen to decrease as the temperature is raised to 400 K. It seems that there is some process limiting the radiative recombination in these two samples above 350 K that is more apparent in the presence of p-doping. The radiative current density obtained for the n-doped sample above 150 K shows the weakest temperature dependence of the three samples and is also a factor of three greater than that of the p-doped sample. The threefold increase in radiative recombination in the n-doped sample is due to the

significant overlap of the QD states (apparent from the modal gain measurements), this intermixing spreads carriers, at any given injection, across a greater number of ESs than the two other samples and these ESs have twice the degeneracy of the GSs. Below 150 K the radiative current density for the un-doped sample increases as the temperature decreases to 60 K and then remains the same down to 25 K. The threshold current density of this un-doped sample is constant below 200 K so from this it is concluded that there is a reduction in non radiative recombination in this sample below 150 K. This reduction in non radiative recombination occurs as the wetting layer decouples from the QD states and so less carries thermally escape the QD states.

The threshold current density of the un-doped sample shows a monotonically increasing threshold current density from low to high temperatures. The threshold current density of this sample is dominated by currents lost to non-radiative recombination. The p-doped structure shows a decreasing threshold current with increasing temperature up to 300 K followed by a sudden increase in threshold current above 300 K. This minimum in threshold current density is attributed to the transition from thermal to non thermal QD population as discussed in section 4.3.3 [Smowton, et al., 2007]. The sudden increase in threshold above 300 K, observed in all samples, is mostly attributed to recombination in the wetting layer. The threshold current density of the n-doped sample is always greater that of the other two samples above 200 K which is due to the significantly increased radiative recombination. At 150 K the threshold current density of the p-doped sample has increased to such an extent that it matches that of the n-doped sample. This suggests that there is an increase in non radiative recombination at 150 K in the p-doped sample as the radiative current density decreases between 200 K and 150 K. This is followed by a considerable decrease in non radiative recombination from 150 K down to 100 K. A similar reduction in non radiative recombination is observed in the n-doped sample from 150 K down to 100 K. All three samples have the same threshold current density at 100 K below and below.

4.4. Conclusions.

In this chapter modal absorption spectra, modal gain spectra and spontaneous emission spectra measured for three samples, two modulation doped and one

intrinsic sample, have been discussed. These results show that the inclusion of p-type modulation doping has no effect on the growth of the QD active region, whilst incorporation of n-type modulation doping appears to change the dot size distribution and appears to cause significant overlap of the QD states. Although the true absorption could not be measured to confirm this conclusion the gain and spontaneous emission measurements for the n-doped sample showed evidence of significant state overlap. This means that devices made from this material would lase at 1.18 μm, not the 1.3 μm telecommunication wavelength which the other sample would emit. The n-type dopant also increases the losses in the gain medium with an α_i 5cm^{-1} larger than the un and p-doped samples. This is due to increased free carrier absorption or scattering due to the creation of defect states within the material.

Net modal gain versus current density plots have shown evidence for a transition from thermal to non-thermal QD occupation occurring between 200 K and 100 K in the un-doped sample and between 300 K and 200 K in the p-doped sample. In the p-doped sample observations of decreasing net gain values for fixed injection between 100 K and 40 K is evidence that there is a significant decrease in the number of dopants that are able to ionise to the GaAs states in the material between these temperatures, due to the decrease in kT relative to Be's ionisation energy in GaAs.

Measurements of spontaneous emission spectra made on these samples have allowed me to determine the radiative current density versus current density characteristics of these samples and using these along with the net gain versus current density plots radiative and total current density versus temperature plots corresponding to a laser length of 2 mm have been constructed for the three samples. In the subsequent chapters of this thesis, novel analysis techniques will be implemented in order to identify the exact nature of the carrier occupation in these QDs and observe the transition from non-thermal to random population. These observations will be used to explain the radiative and total current density plots for these samples as well as the observations made from the net gain versus current density data.

Chapter 5. Measurement of carrier temperature in InAs Quantum Dots.

5.1. Introduction.

In this chapter details of a new method for analyzing the energy distribution of carriers as they occupy the available states of a QD material will be describe. This method is able to determine the nature of occupation in dot states. It can identify the temperature at which the transition from a thermal to random distribution of carriers occurs for any given QD material, directly from experimental measurements of amplified spontaneous emission, with greater precision than previous methods. This is a powerful tool for fully understanding the processes and characteristics that determine the different regimes of operation in QDs and so allow these to be engineered to obtain improved device performance.

5.2. Motivation.

QDs have showed very promising characteristics so far but have not yet fulfilled their potential, partly due to difficulties in predicting or measuring how the available states are populated with carriers. It is commonly thought that at room temperature QDs grown by the Stranski–Krastanow method are populated via thermal coupling with the wetting layer and equilibrium is achieved between the spatially separated dot states. This means that the occupation probability of each dot state should be determined by global Fermi-Dirac statistics over all energies. At low temperature, it is thought that there is a breakdown of the thermal coupling between the dots and the wetting layer, and the dot states are occupied independently of their energy. It has been shown that this brings about a minimum in the radiative current density for a fixed gain at 200 K [O'Driscoll, et al., 2009] while in p doped structures this minimum may even occur at room temperature [Smowton, et al., 2007]. This characteristic is of particular importance as a low and temperature insensitive threshold current is needed for efficient device operation. However, the temperature and energy at which a device's QD states decouple from the wetting layer is still unclear as the point at which it occurs is mainly determined from plots of the

radiative current density versus temperature, and quantitative comparisons to a thermal model [O'Driscoll, et al., 2009]. The ability to directly measure the carrier distribution characteristics will provide the insight necessary to improve the design of QD materials and fully exploit their properties.

5.3. Important definitions.

In section 2.5 of chapter 2 the definitions of three phrases used to describe the nature of the carrier occupation within the QD samples were given. They are repeated here for convenience as they are of particular importance in this chapter.

- **Thermal occupancy** – the QD and wetting layer states are all in thermal equilibrium and occupation of all states can be described by a global Fermi-Dirac distribution in energy.

- **Non-thermal occupancy** – Occupation within any given dot is dependent on energy and can be described by a Fermi-Dirac distribution however the temperature describing each dots distribution does not match that of the lattice.

- **Random Occupancy** – QD states are decoupled from the wetting layer states. The rate of recombination from the dots is significantly faster than the thermal excitation of carriers to the wetting layer so carriers cannot redistribute between spatially separated QDs. Capture into a QD is independent of energy whist emission is dependent on energy so now emission is eliminated, carriers are distributed independently of energy across the dot states.

5.4. Population inversion.

The population inversion factor P is an important quantity used to provide information about how carriers populate the available states of a semiconductor material. It is a number consisting only of the occupations probabilities of states that have a certain energy separation hv. This quantity was introduced in section 2.4.6 and it was discussed how this can be calculated using the segmented contact method in section 3.2.4. These sections describe how a function of the form of P can be

obtained from division of the gain and spontaneous emission spectra, measured for the samples outlined in section 3.4, and this gives information about the energy dependence of carrier population under injection. P was calculated for the un-doped, p-doped and n-doped sample between 25 K and 400 K. Figure 5.1 shows P measured for the un-doped sample at 300 K over a range of injection levels.
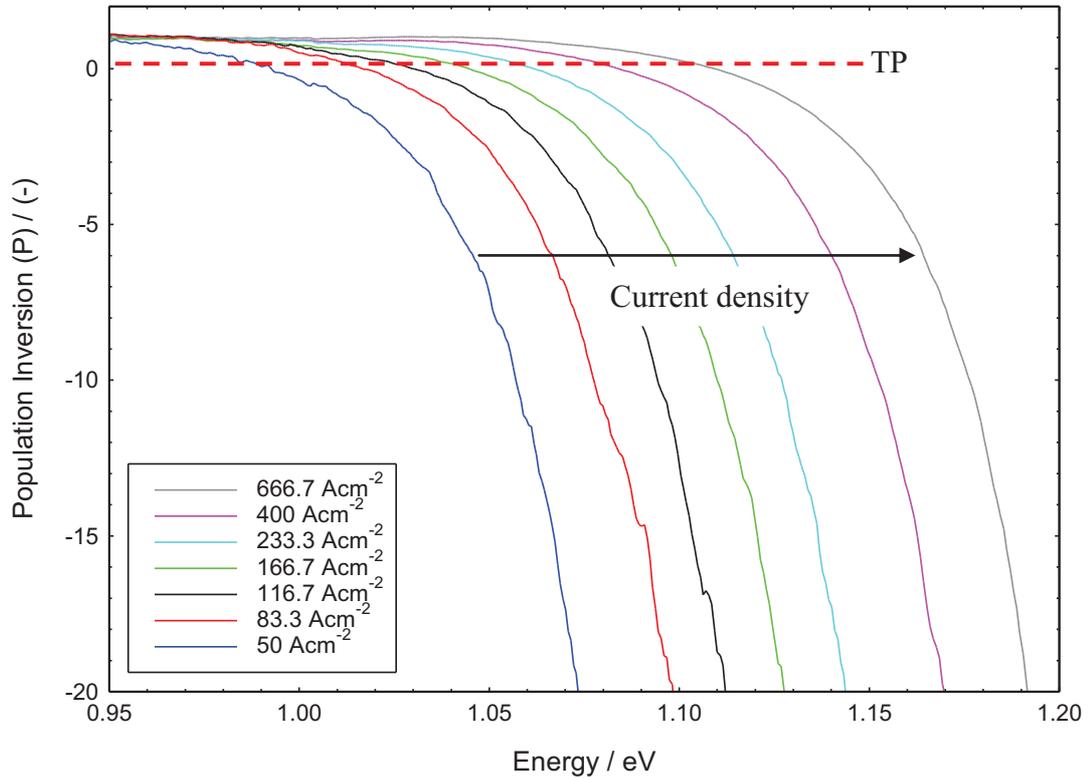
Figure 5.1. Population inversion functions (P) for the un-doped sample plotted against photon energy, measured at 300 K for current densities of 50 Acm^{-2}, 83.3 Acm^{-2}, 116.7 Acm^{-2}, 166.7 Acm^{-2}, 233.3 Acm^{-2}, 400 Acm^{-2}, 666.7 Acm^{-2}.

In Figure 5.1 the typical form of P as a function of photon energy for increasing injection is observed. All functions converge at the same value at low energy and this convergence is evidence that full inversion has been achieved. This is used to calibrate the spontaneous emission. From this the measured P functions can be converted into a form that only includes the occupation probabilities of the electronic states involved with a transition at any given photon energy. As the injection applied to the un-doped sample increases the higher lying states (increasing photon energy) are populated to a greater extent and full inversion is achieved over a larger range of photon energies. The transparency point (TP), as defined in section 3.2.3, is found at

the point at which $P = 0$ and in Figure 5.1 you see that transparency occurs at increasing photon energy as more carries are injected into this un-doped sample.

Simple observation of the P functions in Figure 5.1 does not give any information about the nature of the carrier population within this sample. It is possible to fit a Fermi function of the form in Equation 5.1 (repeated from Equation 2.25 in chapter 2) to the measured P functions at any given injection using the relevant quasi-Fermi level separation obtained from the TP.

$$P = 1 - \exp\left(\frac{E - \Delta E_f}{kT}\right)$$

Equation 5.1

Equation 5.1 was fitted to three P measured for the un-doped sample at various injection levels, this is shown in Figure 5.2.
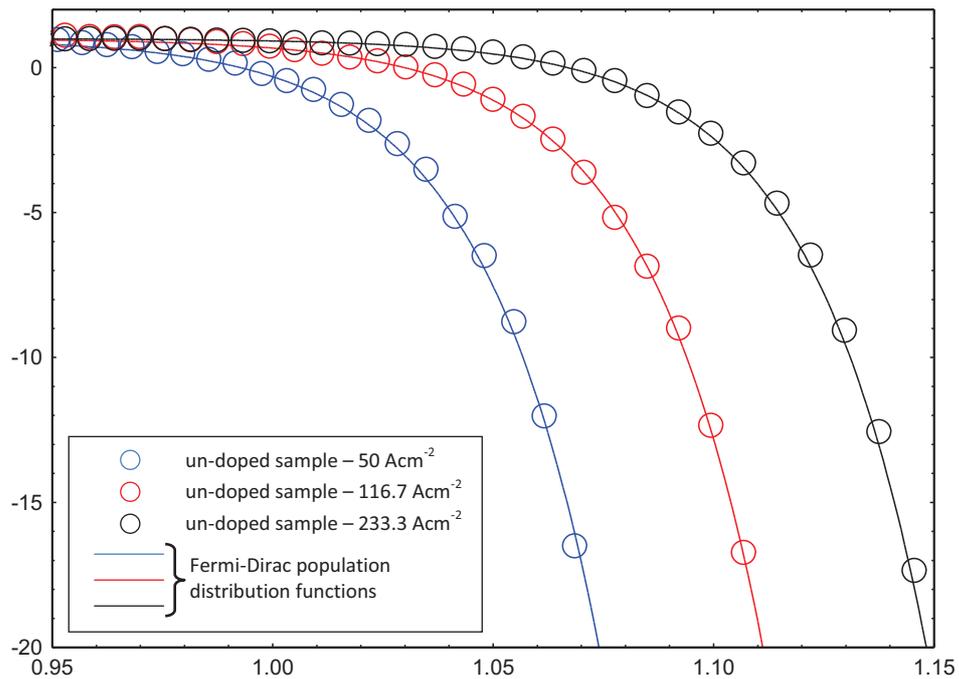

Figure 5.2. Population inversion functions (P) measured at 300 K for the un-doped sample at various injection levels (open circles) fitted with 300K Fermi-Dirac population distribution functions (Solid lines).

A reasonable fit of Equation 5.1 can be made to the P functions shown in Figure 5.2 using a temperature of 300 K however it is difficult to visually define when a good

fit is achieved, leading to large uncertainty in the temperature used to fit the *P* functions. So this method of analysis can only provide evidence of significant changes in nature of the occupation of carriers within any given sample. This fitting approach also assumes that the temperature of the fit is independent of photon energy and so any possible energy dependence that may occur cannot be observed and studied. Such energy dependences could originate from break down of thermal communication between the carriers occupying the spatially separated bimodal distribution of QDs.

In the subsequent sections of this chapter a new method for determining the temperature of carriers as they populate the available states of the QD structure is described. This method is based upon Equation 5.1 but uses a linear fitting approach that provides more information about the energy dependence of occupation than the previous methods whilst reducing ambiguity in the fit. This analysis technique is applied to the three samples described in section 3.4 and the new insight it reveals about these samples is discussed.

5.5. Extraction of carrier temperature.

As discussed this new analysis technique is based upon Equation 5.1, this equation assumes that the carriers populate the available states according to Fermi-Dirac statistics. In its current form it also assumes that equilibrium is reached across all electronic states. Equation 5.1 can be rearranged into the form in Equation 5.2.

$$\ln[1 - P(h\nu)] = \frac{1}{kT_C}.(h\nu) - \left(\frac{\Delta E_f}{kT_c}\right)$$

<div align="right">Equation 5.2</div>

where T_C is carrier temperature. If indeed the carriers adopt a Fermi-Dirac distribution characterised by a T_C, then a logarithmic plot of $[1-P(h\nu)]$ versus photon energy is linear with T_C given by the slope. The key factor however, is that whilst a linear plot shows that the carrier distribution is thermal and can be characterised by T_C, it is not necessarily in equilibrium with the lattice. Variations from linearity indicate a non-thermal distribution of carriers between the QD states.

Logarithmic plots of [1-*P(hv)*] versus photon energy were constructed from the experimental measurements made on all three samples. Figure 5.3 shows an example of one such plot obtained from measurement of the un-doped sample over a range of injection levels at 300 K.
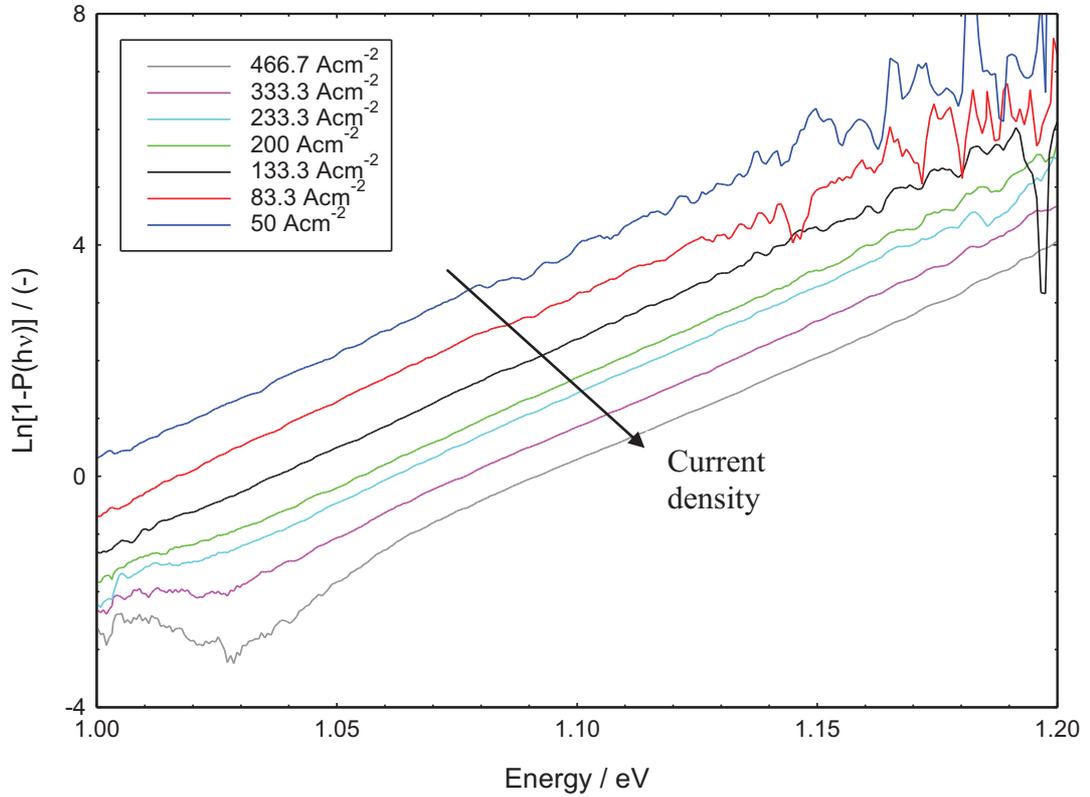
Figure 5.3. Logarithmic plots of [1-P(hv)] versus photon energy for the un-doped sample at measured at 300 K for current densities of 50 Acm^{-2}, 83.3 Acm^{-2}, 133.3 Acm^{-2}, 200 Acm^{-2}, 233.3 Acm^{-2}, 333.3 Acm^{-2}, 466.7 Acm^{-2}

Figure 5.3 shows a set of linear plots that appear to have similar gradients, with the highest and lowest current densities shown giving T_Cs of (322 ± 5) K and (316 ± 10) K respectively. The linearity of the plots suggest that the occupation within QD states themselves can be described by Fermi-Dirac statistics, thus a single T_C can be defined at each injection level, and that there is no discernible dependence of T_C on injection at this temperature. These plots give an average T_C of (325±10) K at this temperature (300 K). If T_C matches the temperature at which the sample was measured, which is defined as the lattice temperature T_L, then the QD states are in thermal equilibrium with the wetting layer and lattice. If T_C does not match T_L then it indicates that there is some non-thermal equilibrium processes occurring.

The fact that the measured T_C for this un-doped sample is greater than T_L was an unexpected result as it is commonly thought that, at room temperature, the dot and wetting layer states are in thermal equilibrium. To determine the origin of the small increase in measured T_C above the T_L, the sample has been modelled using an inhomogeneous ensemble of dots occupied according to Fermi-Dirac statistics [O'Driscoll, et al, 2009]. This model was used to produce modal gain and spontaneous emission spectra from which logarithmic [1-$P(hv)$] plots were calculated and T_Cs were extracted from these plots. At this temperature, increasing levels of homogeneous broadening (HB) were modelled, up to those expected for the injection levels used in our experiments [Borri, et al, 2002]. It was found that for small values of HB, 1 meV at 300 K, the calculated T_C was very close to the actual lattice temperature, within 1 K, however increasing the level of HB raised the calculated T_C. At 300 K it was found that a HB of 6 meV increased the apparent T_C to 326 K. HB allows for an overlap of optical transitions meaning that it is possible for light of a specific photon energy to originate from transitions between states with a spread of occupation probabilities, not just the occupation corresponding to the photon energy itself. This results in an apparent increase in T_C and explains the observations made in my experimental data. Therefore, it can concluded that at 300 K the QD states of this un-doped are in thermal equilibrium with the wetting layer and lattice states.

5.6. Carrier temperature results.

Logarithmic plots of [1-$P(hv)$] versus photon energy were constructed from the experimental measurements made on all three samples between 25 K and 400 K. T_C was extracted from these plots and then plotted against the measured T_L for each of the three samples. So that the injection level of the extracted data is consistent at each temperature, T_C is plotted for fixed levels of gain between 6 cm^{-1} and 20 cm^{-1} at each T_L.

5.6.1. Un-doped sample.

Figure 5.4 shows this data plotted for the un-doped sample. Included on Figure 5.4 are the modelled TC calculations for this sample, used to explain the increased T_C above T_L at 300 K, at all T_L (Solid black line). The temperature dependence of the HB [Borri, et al., 2002] was included in the model calculations.
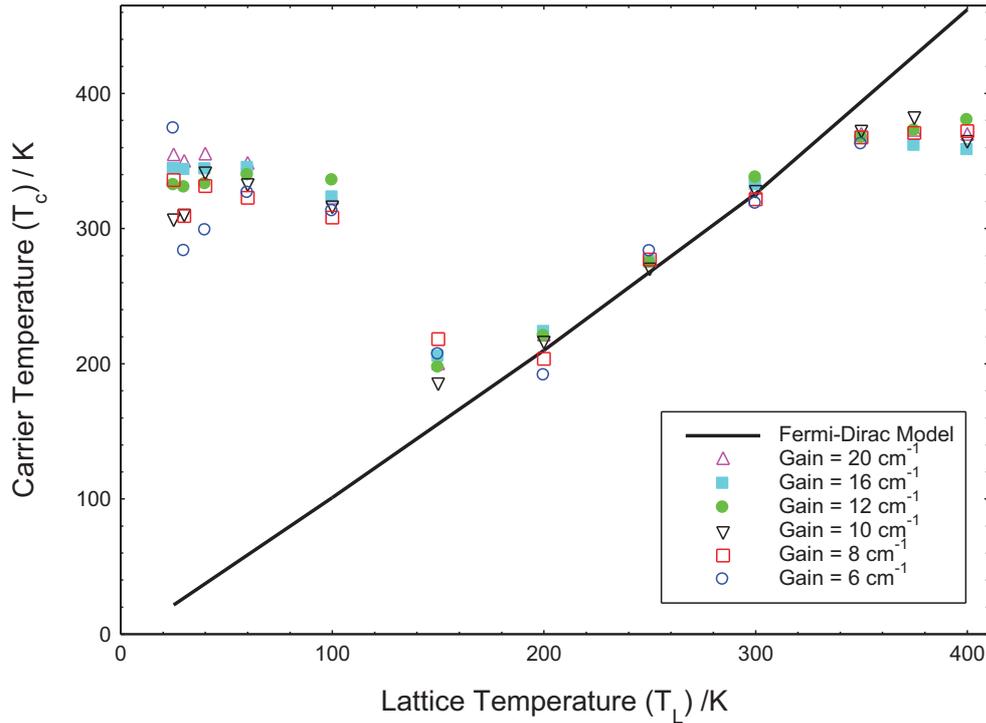
Figure 5.4. *Carrier temperature (T_C) at fixed levels of gain between 6 cm^{-1} and 20 cm^{-1} plotted against lattice temperature (T_L) for the un-doped sample. Also plotted is T_C calculated from the Fermi-Dirac model of the QD ensemble including HB (Solid black line).*

In Figure 5.4 excellent quantitative agreement is observed between the measured T_C and those calculated from the model between 200 K and 300 K with the slight increase in T_C above T_L in this range being explained by HB of the emission from the sample. So it can be concluded that the QD states are in thermal equilibrium with the wetting layer and the lattice between 200 K and 300 K. At a T_L of 150 K, T_C is measured to be (200 ± 15) K. This significant increase in T_C above the T_L is evidence that the dot states are no longer in thermal equilibrium with the lattice, so a larger proportion of higher lying states become occupied. The transition to non-thermal occupancy agrees with measurements of similar samples showing a minimum in radiative and threshold current density at 200 K, attributed to this transition [O'Driscoll, et al., 2009].

T_C at $T_L \leq 150$ K.

As the T_L is decreased from 150 K down to 25 K, T_C increases before a plateau is reached at a T_L of 60 K and below, where T_C fixes at a value of (340 ± 15) K. This suggests that the dot states that are occupied are spread over a much wider energy

range than expected for thermal occupation. I will now show how the pinning of T_C at 60 K and below is evidence that the occupation of states has become random. This agrees with previous work on similar samples showing QD state occupation to be random at these temperatures [O'Driscoll, et al., 2010]. If the occupation of QD states was in fact truly random, then the probability of occupancy would be totally independent of energy and so P would have a constant value up to the TP. This would result in the logarithmic plot of [1-$P(hv)$] having a constant value and so an infinite T_C would be measured. The fact that T_C pins at a real temperature of 340 K at a T_L of 60 K and below indicates that this simple understanding of random population is incomplete. To understand the behaviour of T_C at 60 K and below all recombination, relaxation and excitation processes occurring within the QD and wetting layer states of this sample must be considered. Figure 5.5 shows a simple depiction of two possible state population models that might occur within any given QD sample. In both cases radiative (red arrows) and non-radiative (black arrows) processes are indicated.
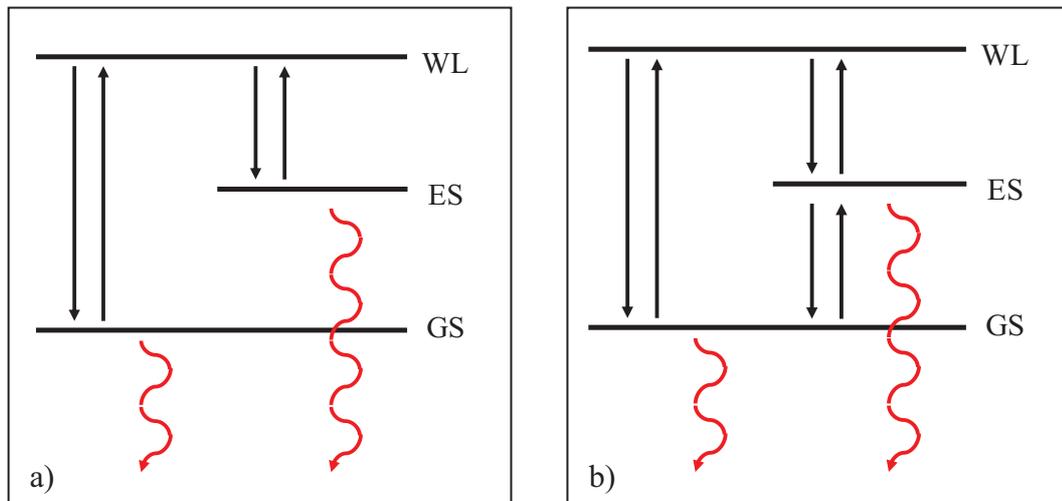
Figure 5.5. *A simple depiction of two possible state population models that might occur within any given QD sample. a) Interaction between Wetting layer (WL) and ground and excited states of the QDs. b) as a) but also includes interaction between ground and excited state within each QD. Both radiative (red arrows) and non-radiative (black arrows) processes are illustrated.*

Model a) in Figure 5.5 includes electronic transition processes between the wetting layer and QD excited states (ES) and ground states (GS) and radiative recombination from those QD states. If these ESs and GSs are then populated randomly from the wetting layer then occupation would be totally independent of energy and so would lead to an infinite T_C. This model is not complete however, model b) in Figure 5.5

shows the complete set of possible processes. On top of those shown in a), interaction between the QD ESs and GSs exist within the same dot. In a random population case the ES and GS are still occupied individually independently of energy. However, now any carrier captured into the ES of a dot can relax into the GS of that same dot. Once inside the QD carrier occupation is energy dependant and so as the temperature of the states (T_L) is reduced then occupation of the lowest energy states (GSs) becomes greater with respect to the higher energy ESs. This means that the occupation probabilities of the GS and ES are different and this causes the $P(hv)$ to have an energy dependence. So a non-infinite T_C will be achieved within any sample occupied according to model b).

In section 4.3.3 the gain versus current density characteristics obtained for this un-doped sample were described. This data showed evidence that this sample was non-thermal at 100 K but was not strong enough evidence to make a solid conclusion. The T_C measured for this sample at 100 K provides the evidence to confirm that this sample is non-thermal at 100 K. At 60 K and below the gain no longer increased for decreasing temperature and saturated with respect to increasing current at the same value. This was attributed to the carrier occupation of the QD states becoming random at 60 K and below but could not confirm this conclusion using these results alone. Again the T_C measurements for this sample can confirm this conclusion but also showed that although the ESs and GSs of the QD are occupied individually independently of energy however, now any carrier captured into the ES of a dot can relax into the GS of that same dot. This trickle down lowers the ES occupancy relative to the GS occupancy. This was observed in the gain data where at 60 K and below the maximum population inversion achieved on the ES was lower than that on the GS.

T_C at $T_L \geq 300$ K.

The T_C characteristics for the un-doped sample above 300 K are surprising. Whereas at a T_L of 300 K a Fermi-Dirac model of QD occupancy quantitatively reproduces the measured T_C at that temperature, at 350 K and 400 K the measured T_C is lower than expected from this thermal distribution model. This implies that at these T_L the QDs are not in thermal equilibrium with the wetting layer states. This was an unexpected result as thermal equilibrium was achieved between all states at 300 K and one

would assume that occupation would remain thermal at higher temperatures. Stringent experimental methods (described in section 3.3 of chapter 3) were implemented to ensure that the measurement of the sample's temperature was accurate and so it is not possible for the sample to be colder than the measured T_L. So T_C is not lower than expected for that reason. T_C being lower than the sample's T_L at 350 K and 400 K means that the QD occupation distribution is not one you would achieve if they were decoupling from the wetting layer states, as this would lead to carriers having a wider spread in energies and thus the measured T_C would be greater than T_L.

To hypothesize why T_C is lower than the T_L above 300 K the available states within a QD structure must be considered. III-V materials have a much larger valence mass than the corresponding conduction mass, meaning that in QDs made from such materials there exists a greater number of closely spaced hole states than electron states. Previous work [Smowton and Sandall, 2007] on InAs QDs used a model including this asymmetry in the number of hole and electron states, with the hole states having a much smaller separation in energy. The large number of closely spaced hole states in the QDs means that the exact number of these states within a QD is sensitive to the size of that dot. So in an ensemble of inhomogeneous QDs, with a range of dot sizes, it is possible that dots of a certain size will have a different number of hole states than other dots of a different size. This means that for neutral dots with equal numbers of electrons and holes, each set of dots of a given size and number of hole states will have a given quasi-Fermi level separation (ΔE_f) and different sized sets of dots, with a different numbers of hole states, will have a different ΔE_f. This is because the quasi-Fermi level for holes and electrons is calculated from the available state distribution and the occupation probability. The effective mass for the hole states is significantly larger than that of the electron states and so the hole quasi-Fermi level stays fixed, so to maintain charge neutrality within QDs that have fewer hole states the occupation probability on the electron states must decrease. Therefore, QDs with fewer hole states will have an electron quasi-Fermi level closer to the hole quasi-Fermi level than those with a greater number of states. This means that ΔE_f is dependent on the number of hole states in a set of dots and therefore the size of those dots. A smaller QD will have fewer hole states as the state separation increases as well width decreases. So the smaller the QD the smaller

the ΔE_f a set of those QDs will have. Equation 5.2 shows that the y-axis intercept of a logarithmic plot of [1-$P(hv)$] versus photon energy is proportional to ΔE_f. Figure 5.6 shows a schematic of three "ideal" ln[1-$P(hv)$] plots for increasing ΔE_f (red lines).
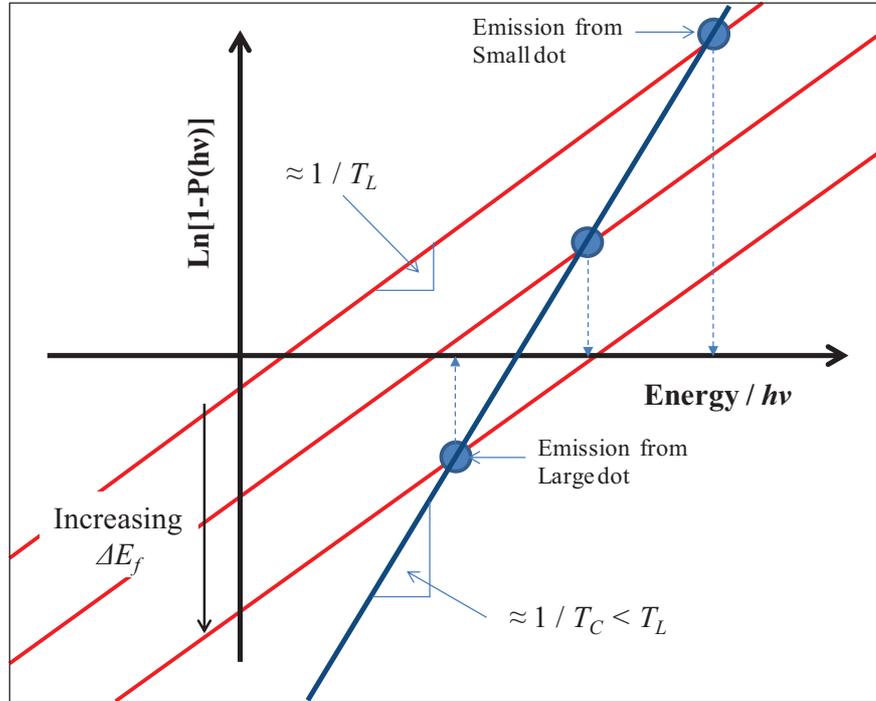

Figure 5.6. Schematic of three "ideal" ln[1-P(hv)] plots for increasing ΔE_f (red lines) obtained for QDs in thermal equilibrium with the lattice so, neglecting HB, so their gradients are given by T_L. The combined emission from these three dots (Blue line) intersects the ln[1-P(hv)] plot for each dot at the energy at which that dot emits. This combined ln[1-P(hv)] plot therefore has a larger gradient and so lower effective T_C.

The schematic logarithmic plots of [1-$P(hv)$] versus photon energy shown in Figure 5.6 illustrate the effect of increasing ΔE_f on plots obtained from a QD that is in thermal equilibrium with the lattice so, neglecting HB, their gradients are given by the T_L. This figure also illustrates how the ln[1-$P(hv)$] plot obtained from a large dot will have a more negative intercept than that obtained from a smaller dot that has fewer hole states. The total emission from an inhomogeneous ensemble of QDs consists of emission from individual dots that is homogeneously broadened. This means that states with a range of different energy separations (different dot sizes) can contribute to emission at single photon energy, this effectively "smoothes" the emission spectrum across all states. Considering the simple case for the three different sized dots shown in Figure 5.6, if you where to combine the emission from

those different size dots you would obtain a ln[1-$P(hv)$] plot that intersects the ln[1-$P(hv)$] plots for each dots different ΔE_f, at the photon energy at which that dot emits. This creates a combined ln[1-$P(hv)$] plot with an increased gradient and thus a lower T_C would be extracted. This is what happens for an ensemble of dots where the measured ln[1-$P(hv)$] plot is created from a combination of all the different dot sizes that lead to a different number of hole states. The T_C measured for the un-doped sample is only lower than the T_L above 300 K because this effect is only apparent when carriers have a wide enough thermal distribution that the higher lying hole states, that exist in the larger dots only, become populated. So although the QD states are almost certainly in thermal equilibrium with the lattice at temperatures above 300 K the emission from a device does not reflect these Fermi-Dirac statistics.

The results obtained by applying the above analysis to the doped samples are now discussed, all the knowledge obtained from studying the T_C versus T_L characteristics of the un-doped sample and its model calculations are used to interpret the observations made for these samples.

5.6.2. P-doped sample.

Figure 5.7 Shows T_C for fixed levels of gain between 6cm^{-1} and 20 cm^{-1} plotted against T_L for the p-doped sample.
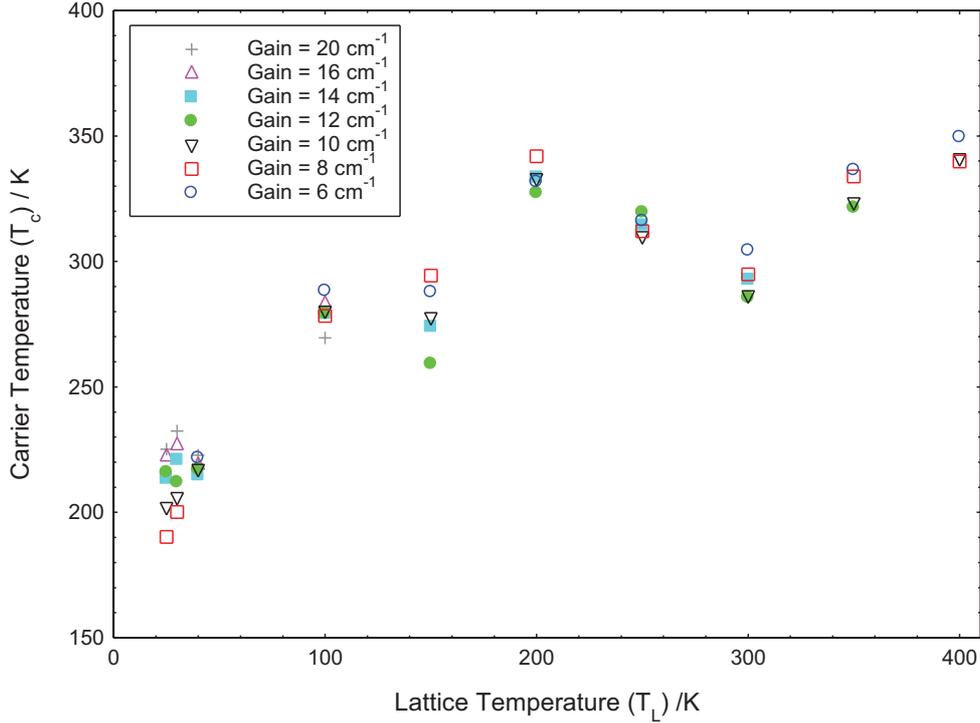
Figure 5.7. Carrier temperature (T_C) at fixed levels of gain between 6cm^{-1} and 20 cm^{-1} plotted against lattice temperature (T_L) for the p-doped sample.

It is clear that the T_C versus T_L characteristics in this p-doped sample are strikingly different to those obtained for the un-doped sample. At 300 K T_C has a value of (295 ± 10) K and although the T_L is within the error of this result, if the QD states where in thermal equilibrium with the lattice at this temperature, the measured T_C would be greater than T_L due to HB. This indicates that at 300 K this sample is showing similar behaviour to that observed for the un-doped sample at 350 K and above. In this p-doped sample the measured T_C is lower than the T_L at a 50 K colder T_L than the un-doped sample. At 350 K and 400 K the T_Cs measured for this p-doped sample are lower than those measured for the un-doped sample at the same T_L. The measured T_C is lower than T_L due to the asymmetry in the effective masses of the hole and electron states leading to there being more, closely spaced, hole states than electron states. This means that dots of different size can have a different numbers of hole states and so individual effective ΔE_f exists for a set of dots depending on how many hole states exist in those dots. In this p-doped sample, more of the hole states are occupied under low injection than in the un-doped sample. This means that the higher lying hole states, and so the states that only exist in the larger dots, are populated at a lower

temperature in the p-doped sample than the un-doped sample so the differences in ΔE_f are apparent at a lower T_L. This explains why the measured T_C is lower than T_L and why this occurs at a lower T_L than that observed for the un-doped sample.

Between 300 K and 200 K, T_C is significantly higher than the T_L and increases for decreasing T_L. From this it is concluded that as in the un-doped sample below 200 K, the QD states are no longer in thermal equilibrium with the wetting layer and lattice, and have a wider energy spread than that corresponding to the lattice temperature. At 200 K T_C reaches a value of (330 ± 10) K but then decreases to (280 ± 15) K as the T_L is reduced to 150 K, T_C then remains constant down to 100 K. This behaviour, although unexpected at first, can be explained by recalling the observations made from the gain verses current density data for this sample (section 4.3.3). It was shown that in this sample as the temperature is reduced, the Be dopant ionisation energy becomes large compared to kT and so fewer and fewer acceptors are ionised into the QD states as the temperature decreases. This has the effect of increasing the spontaneous emission from the QD states at any given gain. From my observations of the un-doped sample, T_C remaining constant between 150 K and 100 K is evidence that the QD states are completely dissociated from the wetting layer and so occupation of the QDs is random.

It was shown how the temperature at which T_C fixed at, under this random occupancy, is related to the relative occupancy levels of the GSs and ESs in the QDs. The greater the difference between the occupancy of the GS and ES, the lower the T_C measured. In the p-doped sample a reduced hole occupation (increased f_1) at fixed inversion (f_2-f_1) was postulated in section 4.3.3 of chapter 4, due to the decreasing ionisation of the Be dopants, to explain the increasing spontaneous emission with decreasing temperature for a fixed gain. Here the same reduction in hole occupation naturally increases the proportion of GS occupation to ES occupation, as the GSs are preferentially filled. This means that the difference in the occupancies of the GS and ES increases as fewer holes are injected into the QDs, so a lower T_C is measured. This explains why T_C reduces between 200 K and 150 K. Between 100 K and 40 K T_C reduces to (215 ± 15) K and then remains fixed down to 25 K. T_C reduces further as even fewer Be atoms are ionised between these temperatures and so the difference in occupancies on the GS and ES increases further. From Figure 5.7 it can be

concluded that in the p-doped sample the occupation of the QD states becomes random at 150 K and below, compared to 60 K in the un-doped sample. This T_C analysis has provided evidence that the Be atoms begin to be unable to ionise, and provide acceptors to the QD states, below 200 K. This effect was not observed in gain verses current density data until the temperature was below 100 K.

5.6.3. N-doped sample

The T_C analysis was applied to the measurements taken for the n-doped sample. Figure 5.8 Shows T_C for fixed levels of gain between 6cm^{-1} and 20 cm^{-1} plotted against T_L for the that sample.
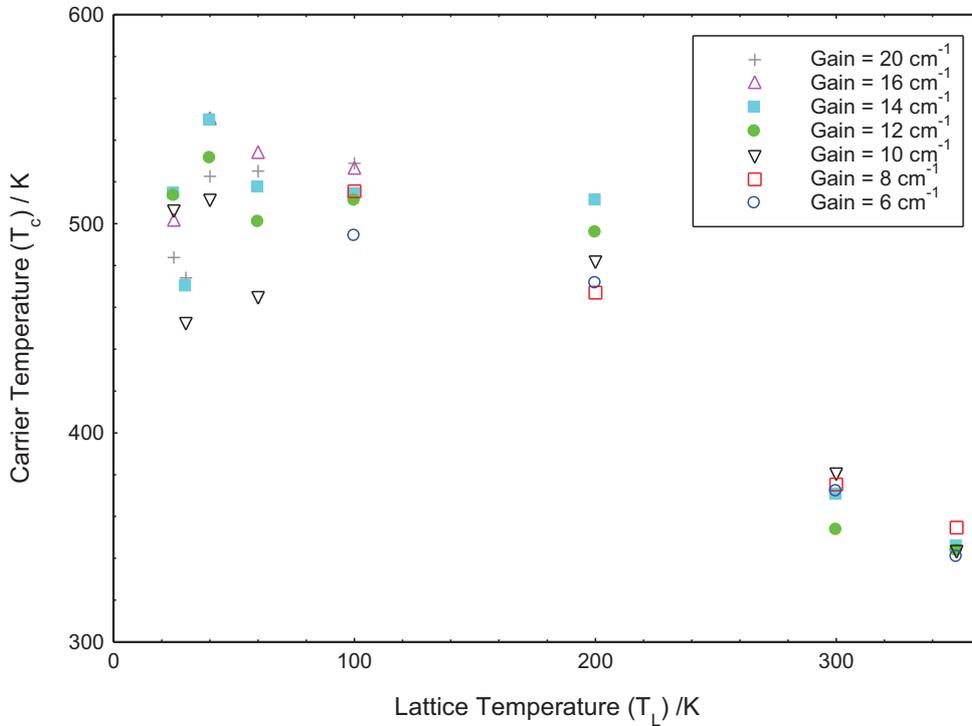
Figure 5.8. Carrier temperature (T_C) at fixed levels of gain between 6cm^{-1} and 20 cm^{-1} plotted against lattice temperature (T_L) for the n-doped sample.

The T_C versus T_L behaviour observed for the n-doped sample is very different to both the un-doped and the p-doped samples. At 300 K the measured T_C is (375 ± 10) K and increases as T_L is reduced from 350 k and 200 K, to a value of (490 ± 20) K. from this it is concluded that over this temperature range the QD states are not in thermal equilibrium with the wetting layer. T_C then remains fixed at (515 ± 20) K from 100 K down to 25 K from which it can be concluded that the occupation of the

QD states with carriers is random at 100 K and below. The gain versus current density data obtained for this n-doped sample (Figure 4.13 in section 4.3.3) did not provide enough evidence to make decisive conclusions about the nature of the QD state occupation in this sample below 100 K but the insight obtained from the T_C measurements shows that the gain data for this sample does concur with the conclusion that QD occupation is random below 100 K.

5.6.4. Comparison between samples.

Some interesting insight can be obtained by comparing the T_C versus T_L behaviour of these samples at temperatures where the QD occupation is not random. Figure 5.9 shows T_C plotted for fixed gain against T_L between 200 K and 400 K for the three samples. This figure includes the T_C calculated from the Fermi-Dirac QD model. This temperature range is particularly relevant as most commercial applications will require devices to operate efficiently within this range.
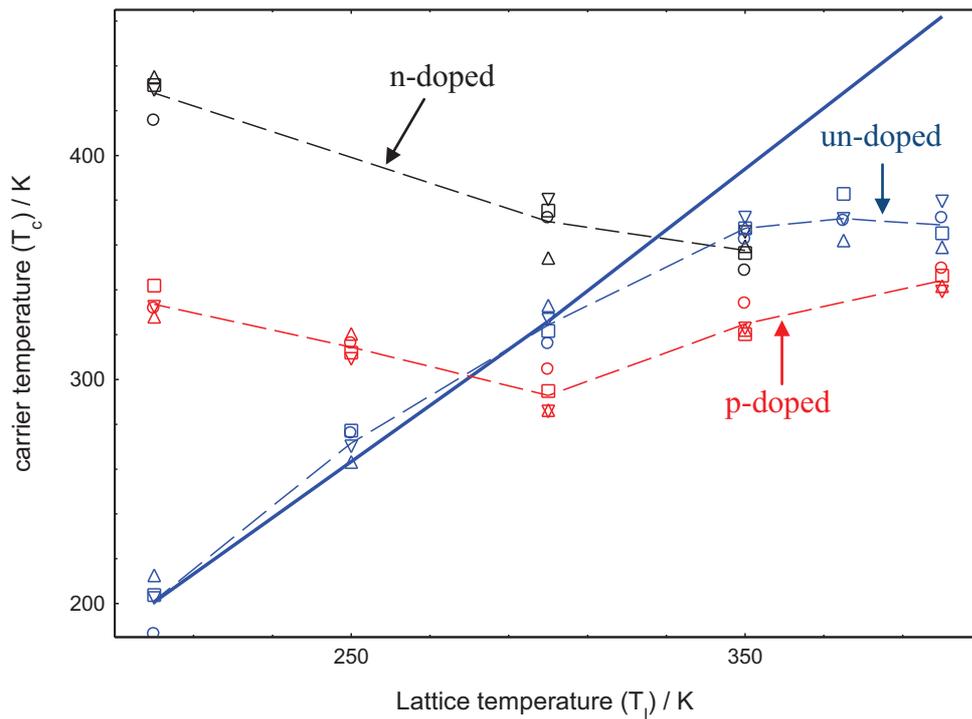

Figure 5.9. *Carrier temperature (T_C) versus Lattice temperature (T_L) for un-doped (blue dashed), p-doped (red dashed), and n-doped (Black dashed) samples as well as Fermi-Dirac model calculations (blue solid).*

The striking feature of Figure 5.9 is that at any T_L, the measured T_C is different in the differently doped samples. Below 300 K T_C of p and n-doped samples is

significantly higher than T_L and increases with decreasing T_L in both sample's, so the occupied dot states are no longer in thermal equilibrium with the wetting layer and have a wider energy spread than that corresponding to the T_L. At 350 K and above, T_C for all the samples is lower than expected from the thermal model calculations at those T_L. This surprising result is observed independently in all three samples and is attributed to there being a larger number of closely spaced hole states than electron states in these QDs due to the asymmetry in the effective masses of these states. This makes the number of hole states in an given dot dependent its size. The effect is most significant in the p-doped sample which provides strong evidence that the state asymmetry is the indeed the cause of the measured T_C being lower than T_L as the hole states are more occupied in the p-doped sample at any given injection. The measured T_C of the un-doped and n-doped sample are within experimental errors at 350 K, this is expected as in the n-doped sample the electron states are more occupied for any given injection, however the lowering of the T_C is due to the closely spaced hole states so this doping has no impact on the T_C measurement. In the next section of this chapter it will be shown that this behaviour is also manifest in the temperature dependence of radiative and threshold current densities of these samples. The p-doped sample has the lowest T_C of the three samples at 300 K. As discussed these T_C have direct consequence on the temperature dependence of the radiative and so threshold current density of a working device and so the understanding and insight this analysis provides is of great importance.

5.7. Temperature dependence of Threshold and radiative current density.

The radiative and threshold current density were discussed in section 4.3.4 where it was described how these were calculated from segmented contact measurements. The data obtained for all three samples was shown and the observations made from the results were described. Here these results are explained using the T_C observations made on the samples. The radiative current density versus temperature is shown for all three samples at a net gain of 6 cm^{-1} in Figure 5.10.
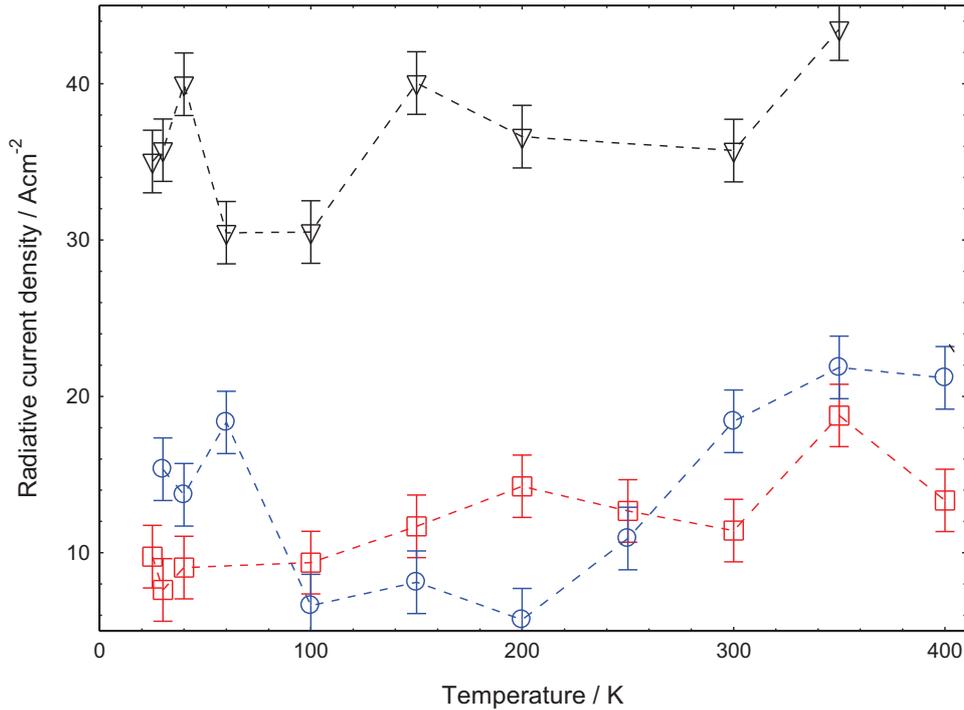
Figure 5.10. *Radiative current density versus temperature for the un-doped (blue circles), p-doped (red squares) and n-doped (black triangles) samples at a fixed net gain of 6 cm⁻¹ (2 mm laser).*

The un-doped sample's radiative current density increases from 200 K to 350 K and then stays constant up to 400 K. This is a direct result of the T_C for this sample where this was shown to increases up to 350 K and then stayed constant as the T_L increased to 400 K. It was concluded from T_C measurements that in all three samples the large number of hole states in these QDs lead to them having a size dependant ΔE_f and when carriers had a wide enough thermal spread in energy, above 300 K, the measured T_C was lower than T_L. These QDs have many more, closely spaced, hole states than electron states due to the asymmetry in the valence masses of these states. This means that when carriers populate the higher lying hole states there is no equivalent electron for it to radiatively recombine with. So for any given injection the radiative recombination is reduced and so the level. In the p-doped sample the higher lying hole states are populated to a greater extent than the un-doped sample at low injection and this explains why in Figure 5.10 the radiative current density for the p-doped sample decreases between 350 K and 400 K. Below 300 K the temperature dependence of the p-doped sample is weak but it does follow the same trend as that seen in the T_C versus T_L for that sample. The radiative current density for the un-doped sample increases as the temperature is decreased from 100 K to

60 K and then remains constant down to 25 K. This mirrors the behaviour of the T_C over this temperature range. Therefore, from this it can be concluded that the increase in radiative current density occurs as the QDs become completely decoupled from the wetting layer and occupation of the QD states becomes random.

The threshold current density versus temperature is shown for all three samples at a net gain of 6 cm^{-1} in Figure 5.11.
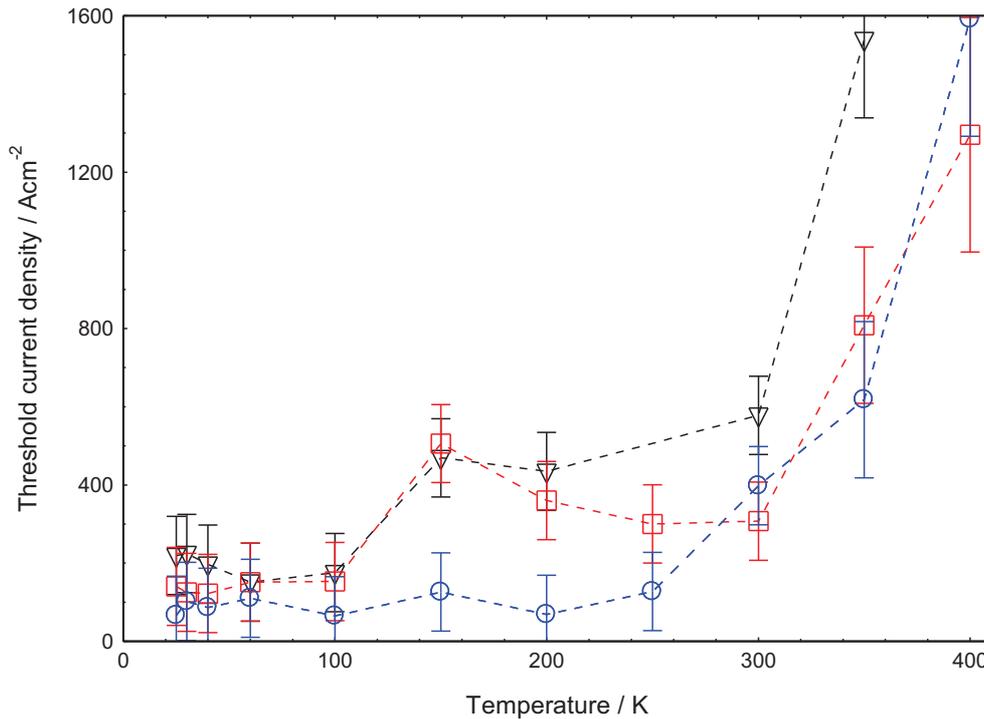
Figure 5.11. Total current density versus Temperature for the un-doped (blue circles), p-doped (red squares) and n-doped (black triangles) samples at a fixed net gain of 6 cm^{-1} (2 mm laser).

The minimum in threshold current density observed for the p-doped sample, giving it the lowest of the three samples at 300 K, is a direct consequence of the minimum in T_C for this sample at this temperature. The threshold current density of the n-doped sample is always greater that of the other two samples above 200 K, this is a result of it having the highest T_C of the three samples. A sudden decrease in threshold current density is observed for the p and n-doped samples below 150 K, the T_C measurements for both these samples show that there is a transition from non-thermal to random QD occupation below 150 K. Random occupation of the QDs results in a reduction in non-radiative recombination in the wetting layer of the sample as carriers cannot escape the QD states before they radiatively recombine.

The threshold current density of the un-doped sample is constant below 200 K however the radiative recombination in this sample increases strongly below 100 K as the QD state occupancy becomes random. For the threshold to remain constant there must be a reduction in the non-radiative recombination below 100 K, this is again due to the complete decoupling of the QD and wetting layer states.

5.8. Conclusions.

In this chapter a novel technique able to study the carrier distributions in QD materials has been described. Using this analysis it is possible to determine the nature of the occupation in the QDs and this is related to key device performance characteristics. The carrier distributions of the un, p and n-doped samples described in section 3.4 of chapter 3 were studied.

The QD states of the un-doped sample were shown to be populated thermally down to 200 K, then between 200 K and 100 K these dot states are not in thermal equilibrium with the wetting layer and the distribution of carriers within the dots was non-thermal. At 60 K and below T_C pinned at (340±15) K showing that the QD states are decoupled from the wetting layer and QD occupation is random. T_C pins at a non-infinite temperature because once a carrier is randomly captured into a dots ES it can relax down to the GS of that same dot before it recombines. This leads to the ES having a lower occupancy than the GS giving a real measured T_C. These results explained the gain verses current density data for the un-doped sample, shown in section 4.3.3 of chapter 4, where those observations could only provide evidence for non-thermal occupation.

The p-doped sample was shown to be non-thermal between 300 K and 200 K where at 150 K the occupation of QDs became random. The T_C measured for this sample reduced between 200 K and 150 K, and 100 K and 40 K, whilst remaining constant between these temperatures. This was attributed to fewer and fewer Be atoms being ionised as the temperature was decreased. The p-doped sample had the lowest T_C of the three samples at 300 K and this leads to it having the lowest threshold current density at that temperature.

The n-doped sample was also shown to be non-thermal between 300 K and 200 K with the T_C then fixing at the highest value of the three samples, (515 ± 20) K, below

100 K showing that the QD occupation was had become random at this temperature and below.

These results show that the T_C within QDs is strongly influenced by doping, with the measured T_C being very different in the three samples at any given T_L. These T_C versus T_L characteristics are mirrored in the radiative and threshold current densities of the samples showing that these processes are strongly influenced by the carrier distribution in the structures. The most striking observations were made above 300 K where, independently in all three samples, the measured T_C was lower than that predicted by a Fermi-Dirac distribution. This was attributed to the asymmetry in the effective masses of the conduction and valence states of these QDs leading to a greater number of more closely spaced hole states than electron states in the dots. This means that the number of hole states in a QD can be different in different size dots and so an individual ΔE_f exists for a given set of dot sizes. This means that emission from an ensemble of dots is "smoothed" across different ΔE_f levels leading to a reduction in the apparent T_C. The implications of these results are that the threshold performance of QD lasers will not be reproduced by calculations in which the carriers on the dots are in quasi-thermal equilibrium with the lattice.

Chapter 6. Temperature dependence of the gain peak in p-doped InAs Quantum Dot lasers.

6.1. Introduction.

In this chapter the modal gain and absorption spectra, shown in chapter 4, are used to extract information about the temperature dependence of the gain peak in these samples. The understanding of this is crucial for development of vertical cavity lasers as in these structures the materials gain spectrum must closely match the reflectivity spectrum of the Bragg mirrors, as these spectra have narrow frequency windows and reflectivity falls of rapidly outside of this window. This analysis requires the existence of a clearly defined peak in the gain and absorption spectra and so is not applicable to the n-doped sample. So this chapter focuses on a comparison between the p-doped and un-doped samples where model calculations are used to explain the observations made.

6.2. Motivation

Inhomogeneous and homogeneous broadening of the states in self-assembled quantum dot (QD) laser structures strongly influence their optical spectra. The inhomogeneity leads to a departure from an idealised density of states and gives rise to disadvantageous characteristics such as an intrinsic temperature dependence of threshold current [Zhukov, et al., 1997] but also benefits such as a broad gain spectrum with potential for short pulse generation [Kuntz, et al., 2007]. The optical spectra of QD devices are also influenced by state-filling, shifting the gain peak to higher energy, and by many body interactions, shifting the gain peak to lower energy, that occur as carriers populate the inhomogeneous states. In some cases the gain peak shifts to energies where there is no absorption [Osborne, et al., 2004]. This is of particular importance for QD vertical cavity lasers, which are of current interest [Lott, et al., 2011], where the gain spectrum should be matched to the reflection spectrum of the mirrors. The effect of incorporating p-type modulation doping has been a key aspect of this thesis where it has been shown how p-doping modifies the

temperature dependence of threshold around room temperature. Here the temperature and injection dependence of the gain peak in the un-doped and p-doped samples studied in this thesis are compared. The results are relevant to the design of QD lasers particularly where the gain peak and its temperature dependence is important.

6.3. Gain peak analysis.

This section describes how a quantitative measure of the shift in the gain peak with current density is extracted from the modal gain measurements, initially described in section 4.4.2 of chapter 4, and then the results obtained are discussed. To fully understand the processes behind these gain peak shifts a measure of injection is chosen, independent of processes that may differ in the two samples, so that comparisons can be made between them. This gives insight into the current density dependence of the gain peak. Then the use a model, first developed by Helen Pask [Pask, 2006] and modified by Ian O'Driscoll, to explain the results obtained from the experiments is described.

6.3.1. Extraction of data.

As discussed in chapter 4, measurements of net modal gain and absorption for various injection levels between 25 K and 400 K have been taken for the un and p-doped samples. This analysis focuses on the data taken between 200 K and 350 K as at these temperatures the occupation of dot states is not random and there is sufficient gain from both samples to make observations with good precision. Random occupation means that state filling occurs independently of energy. So little to no shift in the gain peak is observed with increasing injection in samples where occupancy is random and so is not relevant to this chapter. Figure 6.1 shows gain spectra measured for the p-doped sample over a range of current densities measured at 25 K. This figure illustrates how the gain spectrum evolves for increasing injection when the QD energy states are occupied randomly.
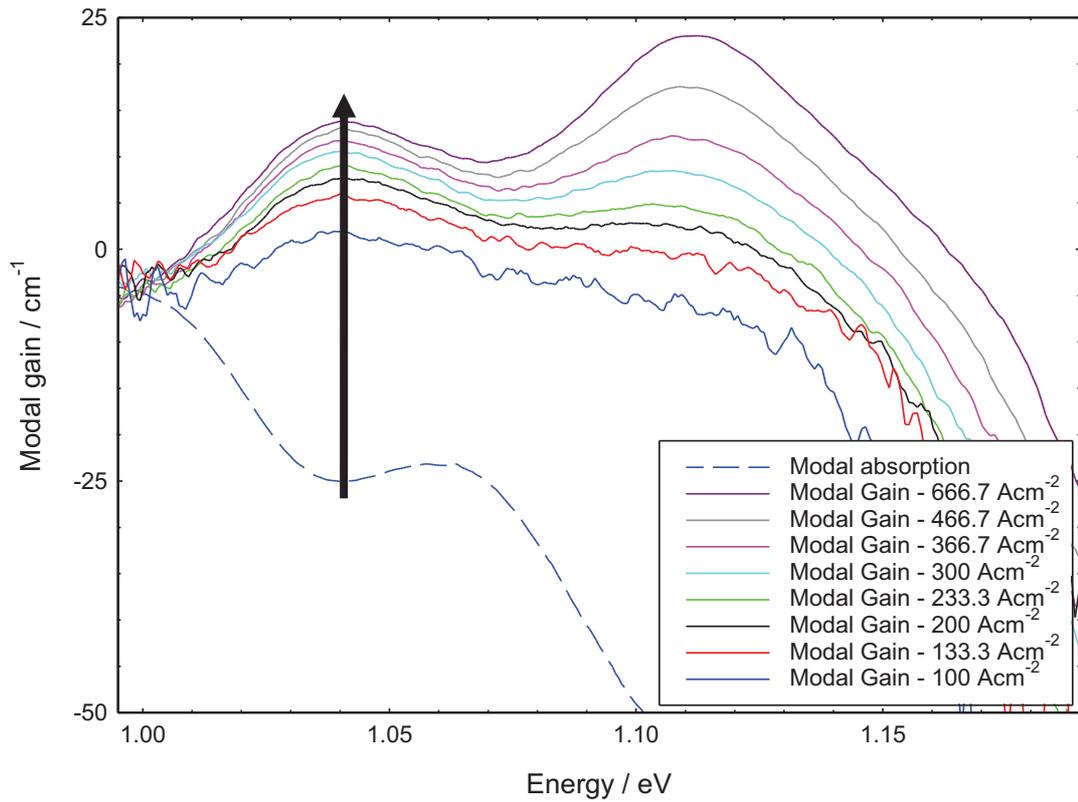
Figure 6.1. Modal gain spectra (solid lines) measured for the p-doped sample at 25 K measured over a range of injection currents densities: 100 Acm⁻², 133.3 Acm⁻², 200 Acm⁻², 233.3 Acm⁻², 300 Acm⁻², 366.7 Acm⁻², 466.7 Acm⁻², and 666.7 Acm⁻² along with the modal absorption spectrum (dashed line) for the p-doped sample at 25 K.

It can be clearly seen in Figure 6.1 that the lowest energy gain peak occurs at 1.04 eV at all current densities and this is the same energy that the first absorption peak occurs at, this shows that these states are occupied independently of energy and so you only observe the inhomogeneous occupation of the QD states. Very similar behaviour is observed for the second gain peak which is associated with the excited states of the QDs showing that these sates are also occupied independently of energy.

The net modal gain spectra measured for the doped structure at 300 K for various injection levels is shown in Figure 6.2 together with the modal absorption measured at that temperature.
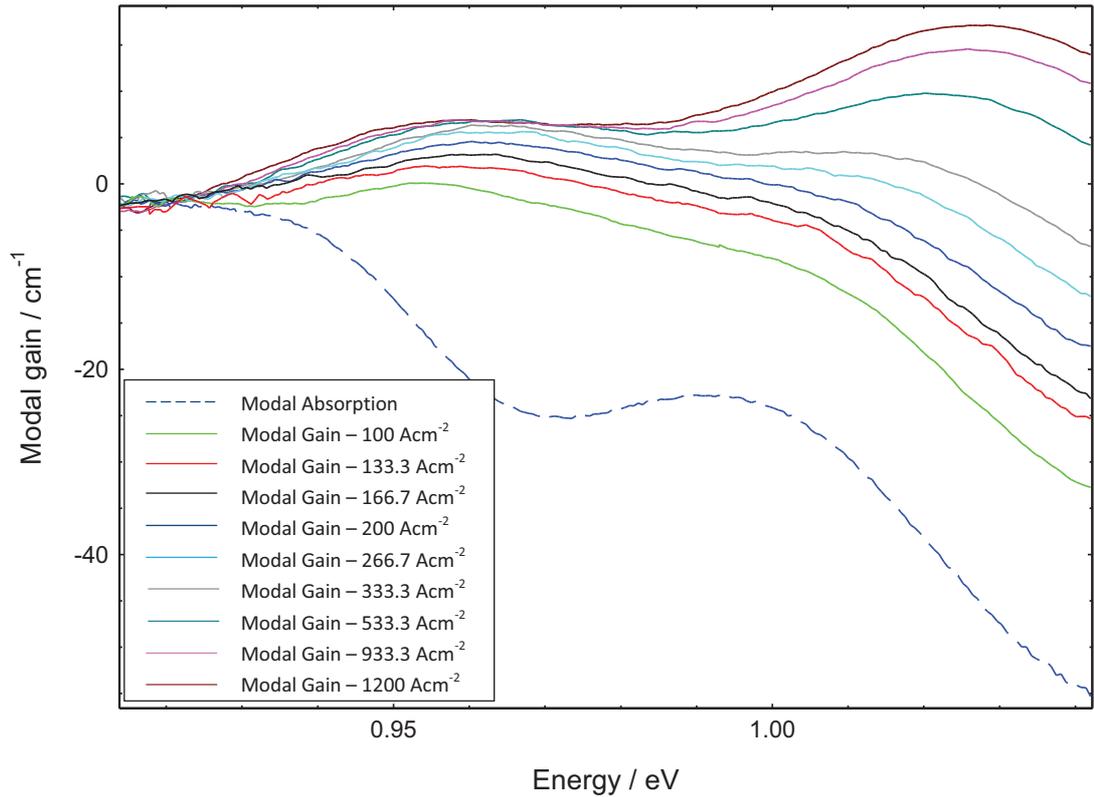
***Figure 6.2. Modal gain spectra (solid lines) over a range of injection currents: 100 Acm⁻²,
133 Acm⁻², 167 Acm⁻², 200 Acm⁻², 267 Acm⁻², 333 Acm⁻², 533 Acm⁻², 933 Acm⁻², 1200 Acm⁻², 1333
Acm⁻² along with the modal absorption spectrum (dashed line) for the p-doped sample at 300 K.***

For this study only the lowest energy gain peak is considered which, in Figure 6.2, is at a lower energy than the first absorption peak (0.972 eV) for all injection levels. As was discussed in chapter 4, the lowest energy peaks of the modal gain and absorption are associated with the ground state transitions only. At the lowest current the gain peak is 18 meV below the absorption peak then initially the gain peak moves closer to the absorption peak with increasing injection, which illustrates the shift in energy due to the filling of the inhomogeneous states in a thermal regime. At higher currents, as the peak gain saturates, a shift to lower energies, away from the absorption peak, is observed and studies [Schneider, et al., 2001 and O'Driscoll, et al., 2010], have shown this to be due to many body effects caused by Coulomb interactions between carriers. Figure 4.5 in chapter 4 shows that qualitatively similar behaviour is observed in the un-doped sample.

To analyse the experimental results and compare the doped and un-doped samples, it is necessary to identify an independent measure of the degree of inversion of the

state in the structures. Although the drive current density, used in chapter 4, is the most relevant measure for real world devices it includes non-radiative processes. While this was an appropriate measure of inversion for those observations, here it is not applicable as for this analysis comparisons require non-radiative contributions to be separated as they have been shown to be different in the two samples. Separating non-radiative contributions is important as this means comparisons will give the important insight into the processes behind the gain peak shifts and the effect of doping, and from this understanding the dependence of the gain peak shifts with current density and temperature can be inferred. Often the quasi-Fermi level separation obtained from the transparency photon energy (discussed in section 3.2.3 of chapter 3) is used as a measure of inversion in the system however, this includes injection dependant shifts by unknown "bandgap narrowing". The magnitude of the ground state peak gain has been chosen as a proxy for the degree of inversion. In chapter 4 it is discussed how this it is proportional to the difference in electron occupation probabilities of upper and lower states at the gain peak (f_c-f_v) and so is independent of non-radiative currents. Also variation in many body enhancements over the range of injections used and between the samples is small so this quantity is a sensible choice to determine the level of inversion. To quantify the shift in the GS gain peak with inversion the difference between this and the first absorption peak energy was measured, as this takes into account the shift in the bandgap with temperature and is a readily definable point of reference. This was then plotted as a function of the magnitude of the ground state peak gain.

6.3.2. Results.

The difference between the GS gain peak energy and the first absorption peak energy (ΔE) is plotted against the magnitude of the GS gain peak for the un-doped sample in Figure 6.3.
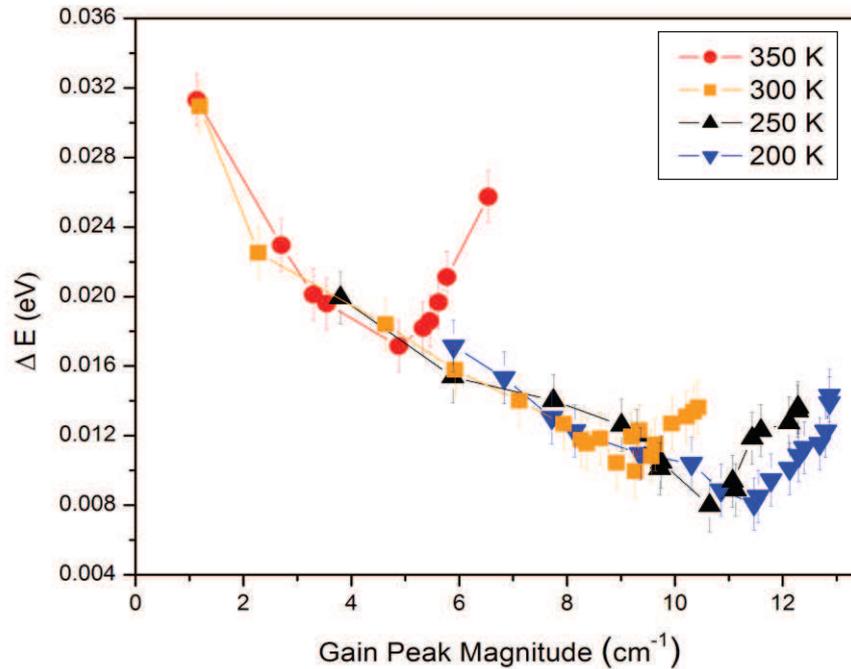
Figure 6.3. Plot of the experimentally measured modal absorption peak energy minus gain peak energy, ΔE, versus gain peak magnitude for the un-doped sample at 350 K, 300 K, 250 K and 200 K

In Figure 6.3 the low injection data points are in a similar range within the experimental error for all temperatures and shows that the gain peak initially shifts to higher energies towards the absorption peak (smaller *ΔE*) for increasing current (as seen qualitatively in Figure 6.2). This illustrates that the QD states are being populated by a similar thermal mechanism between 200 K and 350 K. This is consistent with the observations made in sections 5.6.1 of chapter 5 where it was shown that the QDs are in thermal equilibrium with the wetting layer above 200 K in this un-doped sample. Also the threshold current density versus temperature results in [O'Driscoll, et al., 2009] show that the local minimum at 200 K was evidence for the transition to non-thermal behaviour (below 200 K) within that un-doped sample and this is a lower temperature than that studied here. The up-turn (increased *ΔE*) seen at the highest injections for all temperatures is ascribed to many body effects (also seen qualitatively in Figure 6.2) as at high injection the carrier density of the states is high enough for many body interactions to occur.

The difference between the GS gain peak energy and the first absorption peak energy (*ΔE*) is plotted against the magnitude of the GS gain peak for the p-doped sample in Figure 6.4.
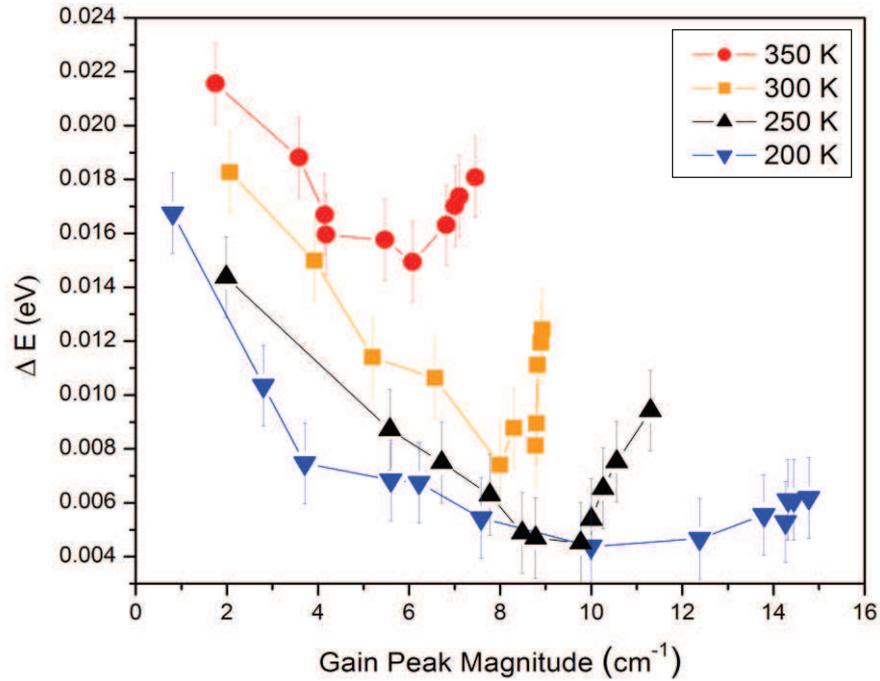
*Figure 6.4. Plot of the experimentally measured modal absorption peak energy minus gain peak energy, ΔE, versus gain peak magnitude for the p-doped sample at 350 K, 300 K, 250 K and 200 K.*

The results for the p-doped sample show a similar movement for the gain peak with injection, at any given temperature, as in the un-doped sample: that is that at low injection the gain peak shifts to higher energy, closer to the absorption peak, due to state filling and at high injection it shifts to lower energies due to many body effects. However, whilst the blue shift due to state filling is the same at all temperatures for a given peak gain magnitude in the un-doped sample, now in this p-doped sample it is clear that the shift due to state filling is different at different temperatures. So as the temperature of the sample is decreased from 350 K to 200 K the energy of the gain peak gets closer to the absorption peak for any given injection. At 350 K the p-doped and un-doped devices show similar quantitative shifts, within the experimental error, in the gain peak energy from the absorption peak at low injection, suggesting that at this temperature the QD states are populated under the same thermal regime. It is possible that the decreasing ΔE with decreasing temperature, for any given injection, is evidence that higher lying states are being populated due to non-thermal population over this temperature range and this is consistent with threshold current density versus temperature measurements showing a minimum at 270 K [Smowton,

et al., 2007], as well as my observations in this p-doped sample, this being within the temperature range measured here. However this effect does not explain the magnitudes of the gain peak shifts with temperatures seen in my experimental results and so does not explain my observations fully. To fully understand the origin of the temperature dependant behaviour seen in the p-doped sample model calculations describing the population of carriers in these QD samples were completed.

6.3.3. Model description.

The model calculations were completed using a model developed by Helen Pask [Pask, 2006] and modified by Ian O'Driscoll. The model is based upon an ensemble of self assembled QDs within two dimensional wetting layer states. The energy states are calculated for harmonic potentials and an inhomogeneous Gaussian distribution of 51 transition energies is constructed. Electronic states corresponding to InAs QDs are modelled with electron and hole effective masses of $0.027m_0$ and $0.34m_0$ respectively (m_0 being the free electron mass). Distributions corresponding to a bimodal distribution of QD sizes are considered with each dot having a ground and 1st excited state distribution. Homogeneous broadening is included in the calculations by applying a Sech function to each transition energy. Although a Lorentzian function is usually used to describe homogeneous broadening, this has infinite tails and so a Sech function that has finite limits is more appropriate. The linewidths used in the Sech function are taken from [Borri et al, 2002] where the temperature dependence of this linewidth is included in the calculations of optical spectra. The Fermi-Dirac carrier distributions across the states of the system are calculated assuming charge neutrality over the whole system. From this, gain and absorption spectra are calculated and the standard deviation of the inhomogeneous broadening input into the model is adjusted until the calculated spectrum matches the experimentally obtained modal absorption spectrum for the samples discussed in this chapter. P-doping is incorporated into the model by including acceptor states in the calculations with an ionisation energy of 28 meV, this being ionisation energy of Be acceptors in GaAs [Galbiati, 1997] for similar levels of doping to that used in this p-doped structure.

6.3.4. Origin of the gain peak temperature dependence.

The model described above was used to construct Figure 6.5 (a) and Figure 6.5 (b) calculated for the un-doped and p-doped samples respectively. Figure 6.5 (a) shows the available ground state inhomogeneous distributions in energy of the electron (top) and hole (bottom) states used in the calculation. Also on this figure are the electron and hole occupation probabilities (f_e and f_h), at 200K and 350 K for a quasi-Fermi level separation of 1.0483 eV, chosen to be greater than the gain peak energy and therefore typical of the quasi-Fermi level separation when the system is inverted. (In this calculation at fixed quasi-Fermi level separation the occupation probability of the electron states goes down with increasing temperature because they are located below the quasi-Fermi energy). From the product of these occupation probabilities and the state distributions, the carrier distributions at the two temperatures have been calculated and this is included on Figure 6.5 (a). At both 350 K and 200 K for this un-doped case the quasi-Fermi level for the electrons (E_{fe}) is well above the ground state inhomogeneous dot distribution and so these electron states are almost fully occupied at both temperatures and so the distribution follows the Gaussian state distribution. This means that there is very little shift in the peak positions of the carrier distributions between the two temperatures and this is consistent with the experimental gain data shown in Figure 6.3.

The same calculations as in Figure 6.5 (a) were completed for the p-doped case using the same state distribution and these are shown in Figure 6.5 (b). The doping has the effect of lowering the quasi-Fermi level for the holes (E_{fh}), relative to the un-doped case, and thus the E_{fe} decreases by the same amount, so that charge neutrality is maintained. E_{fe} is reduced to a level in which it is within the electron inhomogeneous distribution at both temperatures and thus these states are only partially occupied, with the peak of the carrier distribution being within the tail of the Fermi distribution and the Gaussian state distribution. Now a shift in the peak of the occupation distribution is observed between 200 K and 350 K at a fixed gain with the separation between the peak of the electron and hole distribution increasing by 5meV between the two temperatures, at this fixed quasi-Fermi level separation. The shift predicted by this simple model will cause a shift in the energy of the gain peak. The shift observed in the experimental data (Figure 6.4), for fixed gain, is about 8 meV.
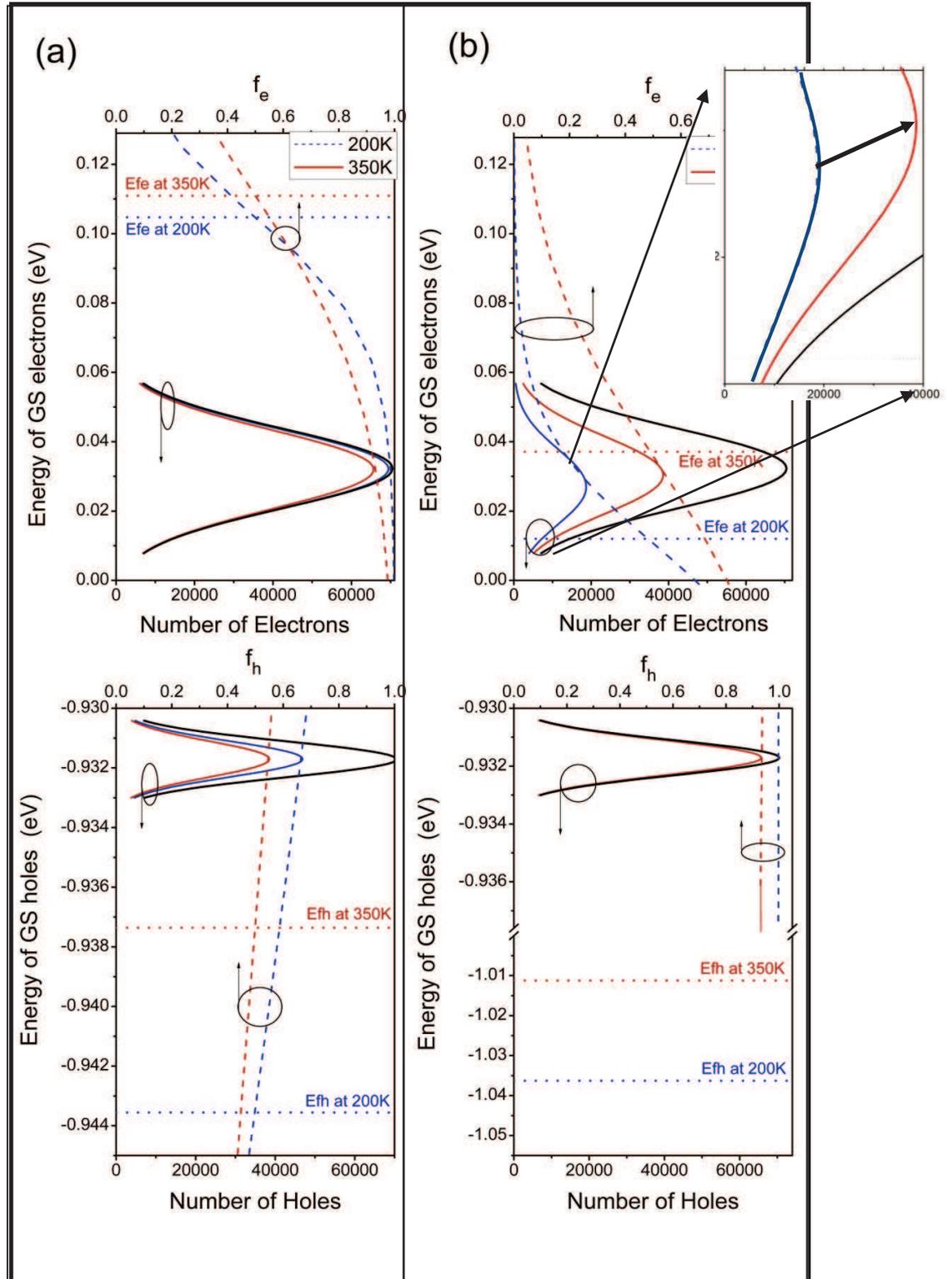
Figure 6.5. *Ground state (GS) distributions of the un-doped (a) and doped (b) samples are shown
as a function of energy, relative to the conduction band edge in the dots, for the electrons (top) and
holes (bottom). The solid black line shows the inhomogeneous state distribution. The distribution
of occupied electron/holes are shown by the solid red and blue lines at 350 K and 200 K
respectively for a fixed quasi-Fermi level separation of 1.0483 eV as well as the calculated
occupation probabilities (upper x-axis). The quasi-Fermi level energies for each temperature are
indicated by the dotted lines.*

There are two origins to the distinct behaviour of the p-doped sample. First, the electron state distribution has a full width at half maximum of about kT at room temperature, whereas the hole distribution is narrower, much less than kT, due to the large effective mass of the valence states in these QDs. Consequently, the distribution of holes follows the inhomogeneous state distribution and does not shift with temperature in either the un-doped and p-doped cases (Figure 6.5). The second factor is the effect of doping on the electron quasi-Fermi level. As discussed, in the un-doped sample, the electron quasi-Fermi level is higher than the electron state distribution (Figure 6.5 (a)), and so most of the electron states are filled and the electron distribution follows the state distribution so is not temperature dependent. However the electron quasi-Fermi level in the doped sample is at lower energy than the electron states (Figure 6.5 (b)), as the doping places carriers in the hole states and so lowers Ef_h. The occupation probability in the electron states is low $(0.2 - 0.4)$, and the carrier distribution is sensitive to the Fermi function, as the distribution now lies within the tail of the Gaussian state distribution. So, the peak of this carrier distribution shifts with temperature as is apparent in Figure 6.5 (b). Thus it is the combination of a wide electron state distribution and the lowering of the electron quasi Fermi level by doping, which results in the temperature sensitivity of the electron distribution and the gain peak in the presence of doping.

6.4. Conclusions.

In this chapter modal gain and absorption measurements, made on the un and p-doped, have been used to determine the temperature dependence of the shift in the gain peak energy. It was shown that the blue-shift of the gain peak due to state-filling in un-doped QD structures is independent of temperature, at a given value of peak gain, over the temperature range studied (200 K to 350 K). Whereas in the p-doped sample the state filling is temperature dependent at any fixed gain. The absorption edge shifts by 50 meV over this studied temperature range and so the experimentally measured 8 meV shift in the state filling in the doped sample is an appreciable quantity compared to this bandgap shift. This behaviour is a consequence of the wide electron state distribution and the lowering of the electron quasi-Fermi level by p-doping relative to the un-doped device. Thus in p-doped QDs the behaviour of the gain peak with temperature and injection is more complex than

in un-doped structures, requiring additional care in the detailed design of devices. While p-doping is often introduced to reduce the temperature dependence of the threshold current it comes at the expense of increasing the temperature sensitivity of the lasing wavelength.

Chapter 7. Conclusions and future work.

7.1. Summary.

In this thesis work new analysis methods that study the carrier distributions in QDs have been developed. These analysis techniques have been applied to three InAs QD structures that are nominally identical except for the doping type in the active region, one p-doped, one n-doped and one left un-doped for comparisons. The results from these analysis methods have been used to explain key properties associated with laser performance including modal gain and radiative and threshold current density. Here the important results drawn from this work are summarised.

The carrier temperature (T_C) has been measured, for the three samples, as a function of lattice temperature (T_L) and this was used to identify the nature of QD occupation at any given T_L. It was found that in the un-doped sample the QD states are in thermal equilibrium with the wetting layer down to 200 K where there is then a transition to non-thermal QD occupation as these states become decoupled from the wetting layer. At 60 K occupation in the QDs becomes random, this is demonstrated by the T_C pinning at (340 ± 15 K) below 60 K. T_C pins at a non-infinite value under random occupation because, although the QD states are occupied independently of energy, the ground and excited states have different occupancies due to a trickle down process. The p-doped sample was shown to be non-thermal between 300 K and 200 K where at 150 K the occupation of QDs became random. The T_C measured for this p-doped sample reduced at 150 K and 40 K whilst remaining fixed between these temperatures, this was attributed to fewer and fewer Be atoms being ionised as the temperature was decreased. The n-doped sample was also shown to be non-thermal between 300 K and 200 K with the T_C then fixing at the highest value of the three samples, (515 ± 20) K, below 100 K showing that the QD occupation was had become random at this temperature and below. In all three samples, above 300 K, the measured T_C was lower than that predicted by a Fermi-Dirac distribution. This unexpected result was attributed to the asymmetry in the effective masses of the conduction and valence states of these QDs, leading to a greater number of more

closely spaced hole states than electron states in the dots and that the number of hole states in a QD can be different in different size dots. This means an individual ΔE_f exists for a given set of dot sizes. So emission from an ensemble of dots is "smoothed" across different ΔE_f levels leading to a reduction in the apparent T_C. The insight that these T_C measurements gave about the nature of QD occupation explained the gain and threshold current density measurements obtained for these three samples. The p-doped sample had the lowest T_C of the three at 300 K and this leads to it having the lowest threshold current density at that temperature. An important implication of these results is that the differences in the observed temperature dependence of threshold of QD lasers due to doping, over the temperature range 200 K to 400 K, will not be reproduced by calculations which assume the carriers on the dots are in quasi-thermal equilibrium with the lattice.

Modal gain measurements made on the un-doped and p-doped samples were used to determine the temperature dependence of the shift in the gain peak energy. The gain peak energy determines the operating wavelength of a device and so understanding the processes behind these shifts is crucial, particularly for vertical cavity lasers where the gain spectrum must closely match the reflectivity spectrum of the Bragg mirrors for efficient operation. It was shown that the blue-shift of the gain peak due to state-filling in un-doped QD structures is independent of temperature, at a given value of peak gain, over the temperature range studied (200 K to 350 K). In the p-doped sample however, the state filling is temperature dependent at any fixed gain with a shift of 8 meV observed between 200 K and 350 K. This was attributed to the wide electron state distribution and the lowering of the electronic quasi-Fermi level by the p-doping. The incorporation of p-dopant in the active region of InAs QD materials was designed to improve the temperature stability of the threshold current densities in laser devices and whilst it was effective in that respect, it has been shown that it comes at the expense of increasing the temperature sensitivity of the lasing wavelength. This renders p-doped materials unsuitable for use in vertical cavity lasers along with any technology application where gain peak wavelength stability is required for efficient operation.

7.2. Conclusions

The principal conclusions from this thesis work are as follows.

- The energy distribution of carriers is different in the un-doped, p-doped and n-doped sample at any given temperature. This directly influences the temperature dependence of radiative and threshold current densities in these devices.

- Above 300 K the carrier distribution in all three samples cannot be described by a Fermi-Dirac distribution with a temperature that matches the lattice. The implications of this are that the threshold performance of QD lasers will not be reproduced by calculations in which the carriers on the dots are in quasi-thermal equilibrium with the lattice.

- The blue-shift of the gain peak due to state-filling in the un-doped QD structure is independent of temperature, at a given value of peak gain. However, the state filling of the p-doped sample is temperature dependant with a shift of 8 meV observed for any fixed gain between 200 K and 350 K. This shift is an appreciable quantity compared to the shift in the bandgap between these temperatures.

7.3. Future work.

The results shown in this thesis have illustrated how the carrier distributions, and so threshold characteristic, cannot be described by a Fermi-Dirac distribution with a global quasi-Fermi level across all electronic states above 300 K. Future theoretical work would be to develop a model that included the asymmetry in the QD hole and electron states that this behaviour is attributed to, this could provide further evidence that my hypothesis is correct. This model would have to describe the population of QD states with carriers such that Fermi-Dirac statistics is not assumed. This could be based on an existing model that calculates QD occupation via rate equations used to compute the radiative and non-radiative processes occurring between the states of the structure [O'Driscoll, et al, 2010]. The implementation of the rate equation requires that each dot has an equal numbers of electron and hole states and the model only describes the emission and recombination processes from a single ground and excited

state in each dot. To develop this model to include asymmetry in the electron and hole states within a QD the implementation of the rate equations would have to be fundamentally altered. If this could be achieved, then the model could be further developed by including dopant states within the calculations in a method similar to that described in section 6.3.3 of chapter 6.

The characterisation technique developed to study the carrier distributions in QD materials could be used to assist in design and creation of a laser device capable of generating high peak power femtosecond optical pulses. The understanding that my analysis techniques provide about carrier distributions is key to utilising the full potential of QDs for the generation of ultra-short optical pulses.

Inhomogeneous and homogeneous broadening in self assembled QDs creates a broad distribution of available states, needed to produce ultra short pulse widths. Theoretically, a common $1.3\mu m$ QD laser with a gain bandwidth of 50 nm could produce pulses as short as 50 fs. It has been shown how the processes by which QD states become occupied with carriers under injection significantly affect the width of the spectra over which these laser media provide gain. At room temperature, equilibrium is achieved between the spatially separated dot states by thermal exchange of carriers with the wetting layer. This inhibits the width of the gain spectrum as the lowest available energy states are preferentially filled. At lower temperatures, it has been shown that dot states are occupied randomly, independently of energy, and this inherently leads to a broadening of the gain spectrum. The techniques developed to probe the carrier distributions in QDs have provided insight into the processes that induce random occupancy in QDs and so this understanding can be used to design QD materials where the QDs become decoupled from the wetting layer states at room temperature. The carrier temperature analysis could then be applied to these new QD materials to determine the nature of QD occupation. The development of these new QD materials could allow the full width of the available gain spectra to be exploited to create devices that can generate pulse lengths that approach those theoretically achievable.

References.

- S. Anders, C. S. Kim, B. Klein, M. W. Keller, and R. P. Mirin, "Bimodal size distribution of self-assembled In Ga As quantum dots", Physical Review B, **66**, 125309 (2002).

- Y. Arakawa and H. Sakaki, "Multidimensional quantum well laser and temperature dependence of its threshold current", Applied Physics Letters, **40**, 939-941 (1982)

- M. Asada, Y. Miyamoto and Suematsu, "Gain and the threshold of three-dimensional quantum-box lasers", IEEE Journal of Quantum Electronics, **22**, 1915-1922 (1986).

- L. V. Asryan and R. A. Suris, "Inhomogeneous line broadening and the threshold current density of a semiconductor quantum dot laser", Semiconductor Science and Technology, **11**, 554-567 (1996).

- D. Bimberg, M. Grundmann, and N. N. Ledentsov, "Quantum dot heterostructures", John Wiley, Chichester, 1999.

- D. Bimberg, N Kirstaedter, N. N. Ledentsov, Z. I. Alferov, P. S. Kopev, V. M. Ustinov, "InGaAs-GaAs Quantum-dot lasers" IEEE Journal of Selected Topics in Quantum Electronics, **3**, 196-205 (1997).

- P. Blood, "On the dimensionality of optical absorption, gain, and recombination in quantum-confined structures", IEEE Journal of Quantum Electronics **36**, 354-362 (2000).

- Blood. P, Lewis. G.M, Smowton. P.M, Summers. H, Thomson. J, Lutti. J, "Characterization of semiconductor laser gain media by the segmented contact method", IEEE Journal of Selected Topics in Quantum Electronics **9**, 5 (2003)

- P. Blood, "Gain and Recombination in Quantum Dot Lasers", IEEE Journal of Selected Topics in Quantum Electronics, **15**, 808-818 (2009)

- P. Borri, W. Langbein, S. Schneider, U. Woggon, R. L. Sellin, D. Ouyang and D. Bimberg, "Ultralong Dephasing Time in InGaAs Quantum Dots", Physical Review Letters, **87**, 157401 (2001).

- P. Borri, W. Langbein, S. Schneider, U. Woggon, R. L. Sellin, D. Ouyang and D. Bimberg, "Exciton relaxation and dephasing in quantum-dot amplifiers from room to cryogenic temperature", IEEE J. Selected Topics in Quantum Electronics, **8,** 984-991 (2002).

- L. A. Coldren and S. W. Corzine, "Diode lasers and photonic integrated circuits," Wiley Series in Microwave and Optical Engineering, 1995.

- N. Chand, E. E. Becker, J. P. Van der Ziel, S. N. G. Chu, and N. K. Dutta, "Excellent uniformity and very low (<50 A/cm^2) threshold current density strained InGaAs quantum well diode lasers on GaAs substrate", Applied Physics Letters, **58**, 1704-1706 (2000)

- D.G. Deppe, K. Shavritranuruk, G. Ozgur, H. Chen, S. Freisem, "Quantum dot laser diode with low threshold and low internal loss", Electronic letters, **45**, 54-56 (2009).

- D. G. Deppe, D. L. Huffaker, S. Csutak, Z. Zou, G. Park, and O. B. Shchekin, "Spontaneous emission and threshold characteristics of 1.3 μm InGaAs-GaAs quantum-dot GaAs-based lasers," IEEE J. Quantum Electronics, **35**, 1238–1246 (1999).

- D. G. Deppe, H. Huang, and O. B. Shchekin, "Modulation characteristics of quantum-dot lasers: the influence of p-type doping and the electronic density of states on obtaining high speed", IEEE J. Quantum Electronics, **38**, 1587-1593 (2002).

- H. Drexler, D. Leornard, W. Hanson and J. P. Kotthaus, "Spectroscopy of Quantum Levels in Charge-Tunable InGaAs Quantum Dots" Physical Review Letters, **73**, 2252-2255 (1994)

- A. Einstein, Phys Z, Translated in "The Old Quantum Theory" D. ter Harr, Oxford, 1967 **18**, 121 (1917).

- S. Fathpour, Z. Mi, P. Bhattacharya, A. R. Kovsh, S. S. Mikhrin, I. L. Krestnikov, A. V. Kozhukov, and N. N. Ledentsov, "The role of Auger recombination in the temperature-dependent output characteristics (T_0=∞) of p-doped 1.3 μm quantum dot lasers", Applied Physics Letters, **85**, 5164-5166 (2004).

- N. Galbiati, C. Gatti, E. Grilli, and M. Guzzi, "Photoluminescence of the Be binding energy in direct band-gap AlGaAs", Applied Physics Letters **71**, 3120-3122 (1997).

- R. N. Hall, "Electron-Hole Recombination in Germanium", Physical Review **87**, 387 (1952).

- H. Jiang and J. Singh, "Strain distribution and electronic spectra of InAs/GaAs self-assembled dots: An eight-band study", Physical Review B, **56**, 4696-4701 (1997)

- T. Kageyam, K. Takada, K. Nishi, M. Yamaguchi, R. Mochida, Y. Maeda; H. Kondo, K. Takemasa, Y. Tanaka; T. Yamamoto;M. Sugawara, Y. Arakawa, "Long-wavelength quantum dot FP and DFB lasers for high temperature applications", Novel in-plane semiconductor lasers XI, Proceedings of SPIE, **8277** (2012).

- K. Kim, T. B. Norris, S. Ghosh, J. Singh, and P. Bhattacharya, "Level degeneracy and temperature-dependent carrier distributions in self organized quantum dot", Applied Physics Letters, 82, 12 (2003).

- N. Kirstaerdter, O. G. Schmidt, N. N. Ledentsov, D. Bimberg, V. M. Ustinov, A. Y. Egorov, A. E. Zhukov, M. V. Maximov, P. S. Kopev, Z. I. Alferov, "Gain and differential gain of single layer InAs/GaAs quantum dot injection lasers", Applied Physics Letters, **69**, 1226-1228 (1996).

- M. Kuntz, G. Fiol, M. Laemmlin, C. Meuer, and D. Bimberg, "High-Speed Mode-Locked Quantum-Dot Lasers and Optical Amplifiers", Proceedings of the IEEE, **95**, 1767-1778 (2007).

- H. Y. Liu, I. R. Sellers, T. J. Badcock, D. J. Mowbray, M. S. Skolnick, K. M. Groom, M. Gutierrez, M. Hopkinson, J. S. Ng, J. P. R. David, and R. Beanland, "Improved performance of 1.3 mm multilayer InAs quantum-dot lasers using a high-growth-temperature GaAs spacer layer", Applied Physics Letters **85**, 704-706 (2004).

- H. Y. Liu, I. R. Sellers, M. Gutierrez, K. M. Groom, W. M. Soong, M. Hopkinson, J. P. R. David, R. Beanland, T. J. Badcock, D. J. Mowbray, "Influences of the spacer layer growth temperature on multilayer InAs/GaAs quantum dot structures", Journal of Applied Physics **96**, 1988 (2004).

- J. A. Lott, V. A. Shchukin, N. N. Ledentsov, A. M. Kasten, and K. D. Choquette, "Passive cavity surface emitting laser", Electronic Letters, **47**, 717-719 (2011).

- J. Lutti, "Optical properties of InP/AlGaInP quantum dot laser heterostructures" , PhD Thesis, Cardiff University (2005).

- D. R. Matthews, H. D. Summers, and P. M. Smowton, "Experimental investigation of the effect of wetting-layer states on the gain–current characteristic of quantum-dot lasers", Applied Physics Letters **81**, 4904-4906 (2002).

- S. S. Mikhrin, A. R. Kovsh, I. L. Krestnikov, A. V. Kozhukhov, D. A. Livshits, N. N. Ledentsov, Yu. M. Shernyakov, I. I. Novikov, M. V. Maximov, V. M. Ustinov and Zh. I. Alferov, "High power temperature-insensitive 1.3 μm InAs/InGaAs/GaAs quantum dot lasers", Semiconductor Science and Technology, **20**, 340 (2005).

- I. O'Driscoll, M. Hutchings, P. M. Smowton, and P. Blood, "Many-body effects in InAs-GaAs laser structures", Applied Physics Letters, 97, 141102 (2010).

- I. O'Driscoll, P. M. Smowton, and P. Blood, "Low temperature nonthermal population of InAs-GaAs quantum dots", IEEE J. Quantum Electronics, **45**, 380-387 (2009).

- I. O'Driscoll, P. M. Smowton, P. Blood, "Random Population of Quantum Dots in InAs–GaAs Laser Structures", J. Quantum Electronics, **46**, 525-532 (2010)

- S. W. Osborne, P. Blood, P. M. Smowton, Y. C. Xin, A. Stintz, D. Huffaker, and L. F. Lester, "Optical absorption cross section of quantum dots", J. Physics B, Condensed Matter, **16**, S3749–S3756 (2004).

- S. Osborne, P. Blood, P. M. Smowton, J. Lutti, Y. C. Xin, A. Stintz, D. Huffaker, L. F. Lester, "State filling in InAs quantum-dot laser structures", IEEE J. Quantum Electronics, **40**, 1639-1645 (2004).

- K. Otsubo, N. Hatori, M. Ishida, S. Okumura, T. Akiyama, Y. Nakata, H. Ebe, M. Sugawara and Y. Arakawa "Temperature-Insensitive Eye-Opening under 10-Gb/s Modulation of 1.3-μm P-Doped Quantum-Dot Lasers without Current Adjustments", Japanese J. of Applied Physics, Part 2, **43**, L1124-L1126 (2004).

- W. Ouerghui, A. Melliti, M. A. Maaref, and J. Bloch, "Dependence on temperature of homogeneous broadening of InGaAs/InAs/GaAs quantum dot fundamental transitions", Physica E, **28**, 519-524 (2005).

- G. Park, O. B. Shchekin, D. L. Huffaker, and D. G. Deppe, "Lasing from InGaAs/GaAs quantum dots with extended wavelength and well defined harmonic-oscillator energy levels", Applied Physics Letters, **73**, 3351–3353 (1998).

- H. Pask, "Model for localised recombination in Quantum dots", PhD Thesis, Cardiff University (2006).

- H. Pettersson, R. J. Warburton, J. P. Kotthaus, N. Carlsson, W. Siefert, M. E. Pistol and L. Samuelson, "Electronic structure of self-assembled InAs quantum dots in InP: An anisotropic quantum-dot system", Physical Review B, **60**, R11289-R11292 (1999).

- K. H. Schmidt, G. Medeiros-Ribeiro, U. Kunze, G. Abstreiter, M. Hagn, and P. M. Petroff, "Size distribution of coherently strained InAs quantum dots", J. Applied Physics, **84**, 4268 (1998).

- H. C. Schneider and W. W. Chow, "Many-body effects in the gain spectra of highly excited quantum-dot lasers", Physics Review B, 64, 115315 (2001).

- O. B. Shchekin and D. G. Deppe, "1.3 μm InAs quantum dot laser with T_o = 161 K from 0 to 80 °C", Applied Physics Letters **80**, 3277-3279 (2002).

- W. Shockley and W. T. J. Read, "Statistics of the Recombination of Holes and Electrons" Physical Review, 87, 835-841 (1952).

- P. M. Smowton, I. C. Sandall, D. J. Mowbray, Hui Yun Liu, and M. Hopkinson, "Temperature-Dependent Gain and Threshold in P-Doped Quantum Dot Lasers", IEEE J. Selected Topics in Quantum Electronics, **13,** 1261-1266 (2007).

- P. M. Smowton, I. C. Sandall, Journal of Applied Physics, 101, 013107 (2007).

- M. Sugawara, K. Makai, and H. Shoji, "Effect of phonon bottleneck on quantum-dot laser performance", Applied Physics Letters, **71,** 2791-2793 (1997).

- T. Takahashi and Y. Arakawa, "Theoretical analysis of gain and dynamic properties of quantum well box lasers", Optoelectronics, Devices and Technologies, **3**, 155-162 (1988).

- J. D. Thomson, H. D. Summers, P. J. Hulyer, P. M. Smowton, P. Blood, "Determination of single-pass optical gain and internal loss using a multisection device", Applied Physics Letters, **75**, 2527-2529, (1999).

- G. W. Turner, H. K. Cho, and M. J. Manfra, "Ultralow-threshold (50 A/cm^2) strained single-quantum-well GaInAsSb/AlGaAsSb lasers emitting at 2.05 μm", Applied Physics Letters, **72**, 876-878 (1998)

- V. M. Ustinov "Quantum dot lasers" (Oxford University Press, Oxford, 2003).

- K. J. Vahala, "Quantum box fabrication tolerance and size limits in semiconductors and their effect on optical gain", IEEE J. Quantum Electronics, **24**, 523-530 (1988).

- K. J. Vahala and C. E. Zah, "Effect of doping on the optical gain and the spontaneous noise enhancement factor in quantum well amplifiers and lasers studied by simple analytical expressions", Applied Physics Letters, **52**, 1945- (1988).

- C. L. Walker, I. C. Sandall, P. M. Smowton, I. R. Sellers, D. J. Mowbray, H. Y. Liu, and M. Hopkinson, "The role of high growth temperature GaAs spacer layers in 1.3 m In(Ga)As quantum-dot lasers", IEEE Photonics Technology Letters, **17**, 2011–2013, (2005).

- Y. C. Zhang, C. J. Huang, F. Q. Liu, B. Xu, J. Wu, Y. H. Chen, D. Ding, W. H. Jiang, X. L. Ye, and Z. G. Wang, "Thermal redistribution of photocarriers between bimodal quantum dots", J. Applied Physics, **90**, 1973 (2001).

- W. Zhou, O. Qasaimeh, J. Phyllips, S. Krishna and P. Bhattachorya, "Bias-controlled wavelength switching in coupled-cavity $In_{0.4}Ga_{0.6}As$/GaAs self-organized quantum dot lasers", Applied Physics Letters, **74**, 783-785 (1999).

- A. E. Zhukov, V. M. Ustinov, A. Y. Egorov, A. R. Kovsh, A. F. Tsatsul'nikov, N. N. Ledentsov, S. V. Zaitsev, N. Y. Gordeev, P. S. Kop'ev, and Z. I. Alferov, "Negative Characteristic Temperature of InGaAs Quantum Dot Injection Laser", Japanese J. of Applied Physics, **36**, 4216-4218 (1997).

Publications.

- <u>M. Hutchings</u>, I. O'Driscoll, P. M. Smowton and P. Blood, "Temperature dependence of the gain peak in p-doped InAs quantum dot lasers", Applied Physics letters, **99**, 151118 (2011).

- I. O'Driscoll, <u>M. Hutchings</u>, P. M. Smowton and P. Blood, "Many-body effects in InAs-GaAs laser structures", Applied Physics letters, **97**, 141102 (2010).

- I. O'Driscoll, <u>M. Hutchings</u>, P. M. Smowton and P. Blood, "Random population of InAs-GaAs quantum dots", Proceedings of SPIE, **7616**, 761605 (2010).

- P. M. Smowton, M. S. Al-Ghamdi, S. Shutts, G. Edwards, <u>M. Hutchings</u>, A. B. Krysa, "Effect of Growth Temperature on InP QD Lasers", IEEE Photonics Technology Letters, **22** (2), pp.88-90 (2010).

Conferences.

- M. Hutchings, I. O'Driscoll, P. M. Smowton, P. Blood, "Carrier Temperature and Threshold Current Density of Quantum Dot Lasers", International Semiconductor Laser Conference (ISLC) 2012 23rd IEEE international, San Diego, USA.

- M. Hutchings, I. O'Driscoll, P. M. Smowton, P. Blood, "Measuring the Carrier Temperature in a Quantum Dot Ensemble", UK semiconductor Conference (UKSC) 2012, Sheffield, UK.

- M. Hutchings, I. O'Driscoll, P. M. Smowton, P. Blood, "Measurement of carrier temperature in InAs Quantum Dots", Semiconductor and Integrated OptoElectronics (SIOE) Conference 2012, Cardiff, UK

- M. Hutchings, I. O'Driscoll, P. M. Smowton, P. Blood, "Band filling in p-doped InAs quantum dot lasers", CLEO 2011, Baltimore, USA.

- M. Hutchings, I. O'Driscoll, P. M. Smowton, P. Blood, "The effect of p-doping on band filling in InAs quantum dot laser structures", Semiconductor and Integrated OptoElectronics (SIOE) Conference 2011, Cardiff, UK

- M. Hutchings, I. O'Driscoll, P. Blood, P. M. Smowton, "Rate equation analysis of Quantum Dot population in InAs/GaAs laser structures", Quantum Dot (QD 2010, Nottingham, UK.